Data Management of Geostationary Communication Satellite Telemetry and Correlation to Space Weather Observations

by

Whitney Quinne Lohmeyer

B.S. Aerospace Engineering
North Carolina State University, 2011

Submitted to the Department of Aeronautics and Astronautics in partial fulfillment of the requirements for the degree

of

Master of Science in Aeronautics and Astronautics

at the

MASSACHUSETTS INSTITUTE OF TECHNOLOGY

February 2013

Signature of Author …………………………………………………………………………...
Department of Aeronautics and Astronautics
January 31, 2013

Certified by …………………………………………………………………………………...
Kerri Cahoy
Assistant Professor of Aeronautics and Astronautics
Thesis Supervisor

Accepted by …………………………………………………………………………………..
Eytan H. Modiano
Professor of Aeronautics and Astronautics
Chair, Graduate Program Committee

Data Management of Geostationary Communication Satellite Telemetry and Correlation to Space Weather Observations

by

Whitney Quinne Lohmeyer

Submitted to the Department of Aeronautics and Astronautics on January 31, 2013 in partial fulfillment of the requirements for the degree of Master of Science in Aeronautics and Astronautics

ABSTRACT

To understand and mitigate the effects of space weather on the performance of geostationary communications satellites, we analyze sixteen years of archived telemetry data from Inmarsat, the UK-based telecommunications company, and compare on-orbit anomalies with space weather observations. Data from multiple space weather sources, such as the Geostationary Operational Environmental Satellites (GOES), are compared with Inmarsat anomalies from 1996 to 2012. The Inmarsat anomalies include 26 solid-state power amplifier (SSPA) anomalies and 226 single event upsets (SEUs). We first compare SSPA anomalies to the solar and geomagnetic cycle. We find most SSPA anomalies occur as solar activity declines, and when geomagnetic activity is low. We compare GOES 2 MeV electron flux and SSPA current for two weeks surrounding each anomaly. Seventeen of the 26 SSPA anomalies occur within two weeks after a severe space weather event. Fifteen of these 17 occur after relativistic electron events. For these fifteen, peak electron flux occurs a mean of 8 days and standard deviation of 4.7 days before the anomaly. Next, we examine SEUs, which are unexpected changes in a satellite's electronics, such as memory changes or trips in power supplies. Previous research has suggested that solar energetic protons (SEPs) cause SEUs. However, we find that SEUs for one generation of satellites are uniformly distributed across the solar cycle. SEUs for a second generation of satellites, for which we currently have only half a solar cycle of data, occur over an order of magnitude more often than the first, even during solar minimum. This suggests that SEPs are not the primary cause of SEUs, and that occurrence rates differ substantially for different satellite hardware platforms with similar functionality in the same environment. These results will guide design improvements and provide insight on operation of geostationary communications satellites during space weather events.

Thesis Supervisor: Kerri Cahoy

Title: Boeing Assistant Professor of Aeronautics and Astronautics

ACKNOWLEDGEMENTS

I would like to acknowledge my parents, Melody and Bill Lohmeyer, for always supporting me and playing a critical role in my success. Dr. Fred DeJarnette, my undergraduate advisor, who's mentoring made long-term goals become reality, and to whom I dedicate this thesis. I would also like to thank my advisor, Kerri Cahoy, for her continuous mentoring throughout my time at MIT, and during the summer before my first semester. Additionally, I would like to thank Leonard Bouygues, Carolann Belk, Gina Annab, Natalya Brikner, Ingrid Beerer, and Qiaoyin Yang for their love and friendship, which I will indefinitely cherish.

Furthermore, I would like to acknowledge Dan Baker, Yuri Shprits, Mark Dickinson, Marcus Vilaca, Janet Greene, Cathryn Mitchell, Joe Kinrade, the Invert Centre for Imaging Science at the University of Bath, Greg Ginet, Anthea Coster, Trey Cade, the Inmarsat Spacecraft Analysts, and Joseph Ditommaso for their support. I would also like to thank NOAA, LANL, ACE, SIDC and the World Data Center for Geomagnetism for access to their space environment databases. Lastly, I would like to thank NSF, MIT, and Inmarsat for funding this work.

TABLE OF CONTENTS

LIST OF ACRONYMS

ACE – Advanced Composition Explorer
ACS – Attitude Control System
AMER – Americas Region
AOR – Atlantic Ocean Region
APAC – Asian Pacific Region
CME – Coronal Mass Ejection
DST – Disturbance Storm Time Index
EMEA – Europe Middle East Africa Region
EPAM – Energetic Ion and Electron Instrument
EPEAD – Energetic Proton, Electron and Alpha Detector
EPS – Energetic Particle Sensor
ESA – European Space Agency
ESD – Electrostatic Discharge
ESP – Energy Spectrometer for Particles
EUV – Extreme Ultraviolet Sensor
GCR – Galactic Cosmic Rays
GEO – Geostationary
GOES – Geostationary Operational Environmental Satellites
HEPAD – High Energy Proton and Alpha Particle Detector
IMF – Interplanetary Magnetic Field
IOR – Indian Ocean Region
LANL – Los Alamos National Labs
MAG – Magnetic Field Vectors Instrument and Data
MAGED – Magnetospheric Electron Detector
MAGPD – Magnetospheric Proton Detector
PAC – Pacific Region
POR – Pacific Ocean Region
RTSW – Real Time Solar Wind System
SEM – Space Environment Monitor
SEP – Solar Energetic Protons
SEU – Single Event Upsets
SIDC – Solar Influences Data Center
SIR – Stream Interaction Regions
SIS – High Energy Particle Fluxes Instrument
SPE – Solar Proton Events
SPENVIS – Space Environment Information System
SSB – Space Studies Board
SSPA – Solid State Power Amplifier
STK – Satellite Tool Kit
SWEPAM – Solar Wind Electron, Proton, and Alpha Monitor
SWPC – Space Weather Prediction Center
TDRS – Tracking Relay Satellite System
XRS – X-Ray Sensor

LIST OF FIGURES

LIST OF TABLES

CHAPTER 1: INTRODUCTION AND MOTIVATION

In 2008, the National Research Council published the "Severe Space Weather Events – Understanding Societal and Economic Impacts Workshop Report". This report documents the findings from the 2007 public workshop that the Space Studies Board (SSB) of the National Academies was charged to convene to assess the nation's ability to manage the effect of space weather and their societal and economic impacts [NRC, 2008].

One of the primary technologies of focus was the telecommunications industry. At the time of the workshop more than 250 geostationary communications satellites were in orbit, which amounted to more than a $75 billion dollar investment that delivers an annual revenue of $25 billion. Yet economics aside, this critical infrastructure is important because of the services it provides. To name a few, these satellites provide backup communication in the event of a disaster that damages ground based communications systems, they provide news, education, and entertainment to remote areas, and connect end users including military, maritime officials, or civilian subscribers.

However, the telecommunications industry is being challenged by space weather, which is not only affecting the satellites, but the satellite engineers, satellite operators and the satellite customers. For example, in 1994 Canadian Telesat experienced a space weather induced satellite anomaly when their Anik E2 satellite went off air due to an energetic electron induced discharge to the control unit. As a result, more than 100,000 dish owners and 1,600 remote communities were affected. Fortunately, the 290 million dollar satellite was restored after an intensive six month, $70 million recovery effort. Numerous other examples of space weather induced anomalies exist, yet the primary challenge lies in understanding how to quantify the effects of space weather on satellite components.

In fact, one of the workshop conclusions was that access to space weather data and as well as satellite telemetry, is the first step in better understanding the cause of satellite anomalies as they pertain to space weather. It is widely known that space weather impacts the performance of satellite systems. The ability to quantify these effects requires the analysis of both space weather and satellite anomaly data; *however, the main challenge is not access to space weather data, but rather satellite anomaly data*

Decades of spacecraft anomaly data sit unused in the electronic telemetry archives of major geostationary communications satellite manufacturers and operators. Telemetry comes from the Greek words tele (remote) and metron (measure), meaning to measure from a distance. These telemetry data are faithfully acquired and monitored by ground operators, and anomaly alarms are sounded should the component health data stray outside of pre-defined nominal or safe operational thresholds. The spacecraft health data are largely used in real time to help mitigate the effect of anomalies on the overall system performance and minimize impact to customers. Once the "fire" has been put out, the telemetry data are used for fault investigations, ground-based anomaly re-creation and modeling, and summaries of lessons learned.

The extensive databases of on-orbit anomalies from commercial spacecraft operators have not yet been released for scientific investigations. This is partly because scientific analyses of these anomaly data, beyond the engineering analyses for prompt detection and mitigation strategies, are not in the immediate interest of these businesses. However, these companies are interested in using accurate real-time space weather predictions and observations for fleet operations, and thus have some motivation to contribute via research collaborations to the space weather community.

Recently, *Choi et al.* (2012) analyzed the effects of space weather on ninety-five satellite anomalies from seventy-nine unique satellites. The study incorporated publicly available geostationary satellite anomaly data with the causes ranging from electrostatic discharge, to loss of amplifiers, complete power system failure, etc. Yet, several of these anomalies, such as those caused from failure to deploy a solar array or a safe-hold triggered by faulty ground-control software, were not likely due to space weather and should have been filtered from the analysis [Mazur, 2012]. Furthermore, although their correlation between space weather and these anomalies noted relationships between anomalies and local time, seasonal dependencies, and geomagnetic index Kp, did not normalize for the different conditions that exist between different satellite buses. Our research methodology stresses the need for normalization in the analysis of different satellite manufacturers and hardware components to assure an accurate correlation study.

For this research, we partner with Inmarsat, a telecommunications company based in the UK, to analyze satellite component anomaly data from eight satellites on two of Inmarsat's satellite fleets. Inmarsat has been operating its fleet of geostationary (GEO) satellites for more than twenty years, and has maintained a complete archive of component telemetry and housekeeping data for more than twenty years with the primary purpose of monitoring spacecraft health and performance. Since 1996, the satellites have experienced twenty-six solid-state power amplifier (SSPA) anomalies. SSPAs are a key component in satellite communication systems, as they are used to amplify the uplink signals received by the satellite from the ground before re-transmitting the downlink signals to the users on the ground.

SSPAs have advantages in reliability, ruggedness, size and cost, compared to alternatives such as traveling wave tube amplifiers [Sechi, 2009]. There are generally two types of SSPA anomalies, "hard" failures and "soft" failures. Soft failures are generally recoverable (e.g. from power cycling) and hard failures are not. Both failures are identified when health measurements, such as SSPA current in this work, fall below a pre-defined threshold. The threshold setting is specific to particular hardware, for example, the thresholds for Fleet A SSPAs and Fleet B SSPAs are different as the satellites had different manufacturers. These health measurements are continuously recorded (e.g., hourly) and saved and then downlinked to the ground where they are monitored and archived.

It should be noted that anomalies with on-board components, such as SSPAs, are expected and are managed by all satellite operators. Anomaly rates are factored into the design of geostationary satellites and are typically mitigated through the use of on-board unit redundancy and configuration options. The current SSPA anomaly rate presented is significantly lower than that modeled as part of the design reliability analysis; hence both satellite performance and lifetime have not been impacted adversely.

In order to more accurately quantify the effect of space weather on geostationary communications satellites we focus on one type of component anomaly, solid-state power amplifiers, as well as single event upsets (SEU). Analyzing data from 5 satellites of the same fleet, and then comparing the results with a second 3-satellite fleet allows high level insight into the effect of satellite hardware differences that are not possible in a larger, more general study. What causes these anomalies and failures? Alone, the data contain valuable information about how space weather impacts flight electronics and materials as a function of age, time, and location. The data are even more valuable when combined with space weather observations from spacecraft and from the ground. We compare the satellite anomalies with observations of the space weather environment using space weather databases from: the Geostationary Operational Environmental Satellite (GOES) database, the Advanced Composition Explorer (ACE) database, the World Data Center for Geomagnetism in Kyoto, Japan, the Solar Influence Data Center (SIDC) in Brussels, Belgium, and severe space weather events from the NOAA Space Weather Prediction Center (SWPC).

One open question is whether there are periods during the lifetime of a satellite when they may be more susceptible to anomalies, separate from the influence of space weather. For example, seven of the twenty-six SSPA anomalies occurred within the first two years of the satellites' lifetime. Did these seven anomalies result from the taxing launch environment and orbital repositioning maneuvers that a satellite experiences within the first two years of operation, or from space weather? As we discuss in more detail in this work, anomalies that occur within the first two years of operation should first be investigated for correlation to space weather events before being categorized as "burn-in" or launch environment-related anomalies.

Inmarsat Satellite Fleet

Table 1 summarizes the three primary Inmarsat fleets, their launch date, coverage area, and longitudinal location. The fleet number I2, I3, or I4, designates Inmarsat Fleet 2, 3 and 4, along with the flight number F1, F2, F3, etc. I2 originally consisted of four satellites, however two have been decommissioned, which are the only Inmarsat satellites to have been decommissioned thus far. I3 consists of five satellites, and I4 consists of three satellites.

Both of the I2 satellites are currently positioned over the Pacific region (PAC). For the I3 satellite fleet, the coverage areas are divided into ocean regions: Atlantic Ocean Region (AOR), Indian Ocean Region (IOR), and the Pacific Ocean Region (POR). Lastly, the I4 coverage areas are divided into three regions: Asia-Pacific (APAC), Europe-Middle East-Africa (EMEA), and the Americas (AMER).

Table 1: Inmarsat Fleet

Satellite	Launch Date	Coverage	Longitude
I2F1	30 October 1990	PAC	109 E
I2F2	05 March 1991	PAC	142 W
I2F3	16 December 1991	Decommissioned 2006	
I2F4	15 April 1992	Decommissioned 2012	
I3F1	03 April 1996	IOR	64 E
I3F2	06 September 1996	AOR	15.5 W
I3F3	18 December 1996	POR	178 E
I3F4	03 June 1997	AOR	54 W
I3F5	04 February 1998	IOR	25 E

I4F1	12 March 2005	APAC	143.5 E
I4F2	08 November 2005	EMEA	25 E
I4F3	18 August 2008	AMER	98 W

Figure 1 provides an outline of the global satellite fleet configurations and coverage areas as of June 2012, and described in Table 1. These satellites are located in a geostationary orbit about the equator, and maintain an altitude of 6.6 earth radii (R_E), or approximately 36,000 km [Vampola et al., 1985]. Geostationary orbit has an eccentricity of zero, and is thus considered to be a circular orbit.

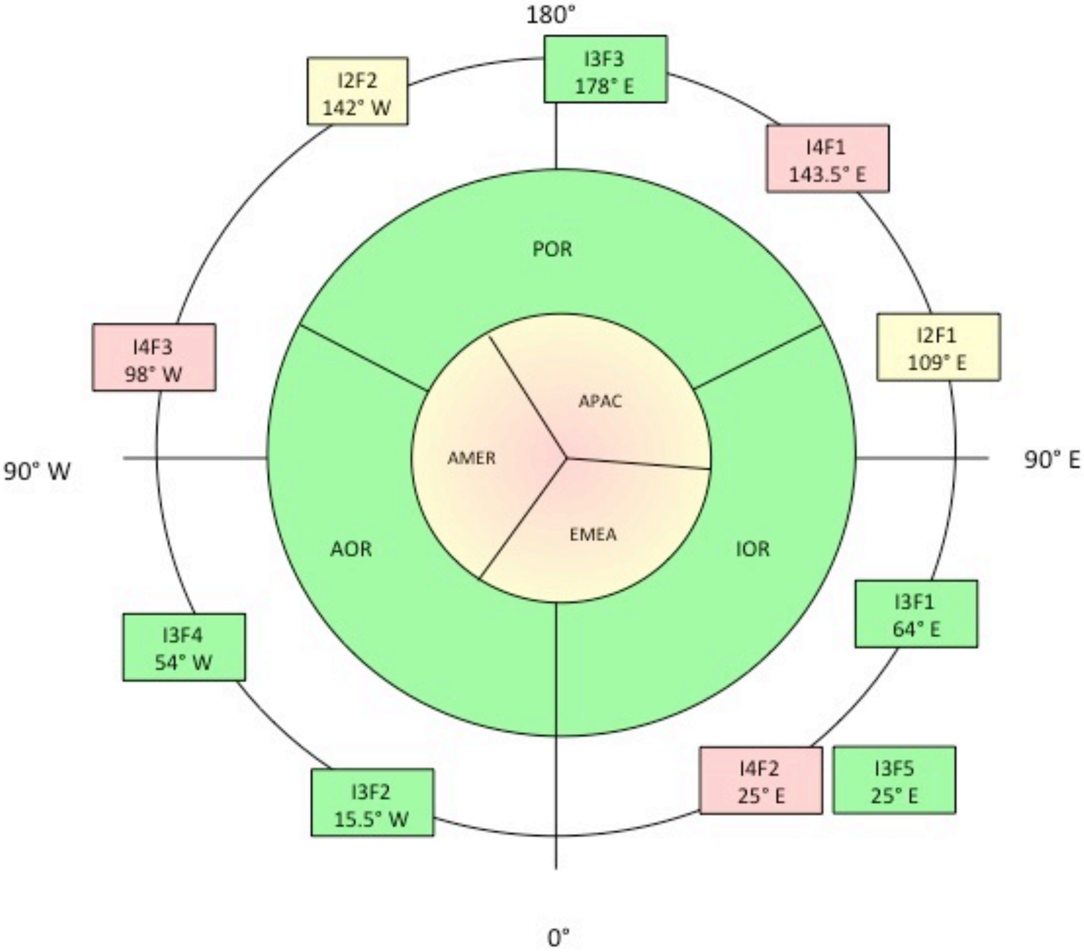

Figure 1: Inmarsat Satellite Locations and Coverage

Figure 2(a,b) shows the orbit for two of Inmarsat's satellites generated in Satellite Tool Kit (STK), one satellite is designated in yellow and the other satellite is shown in pink.

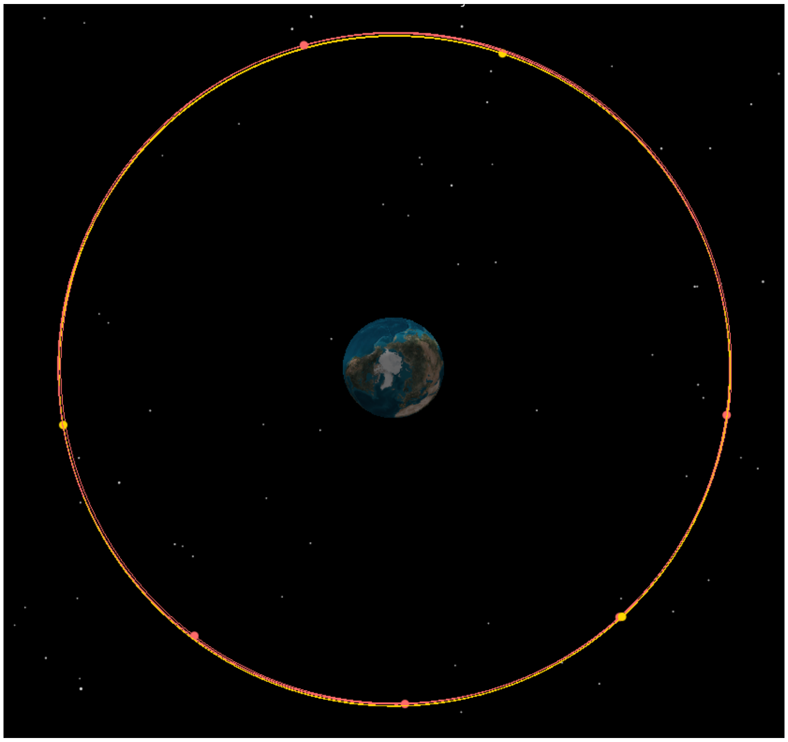

(a)

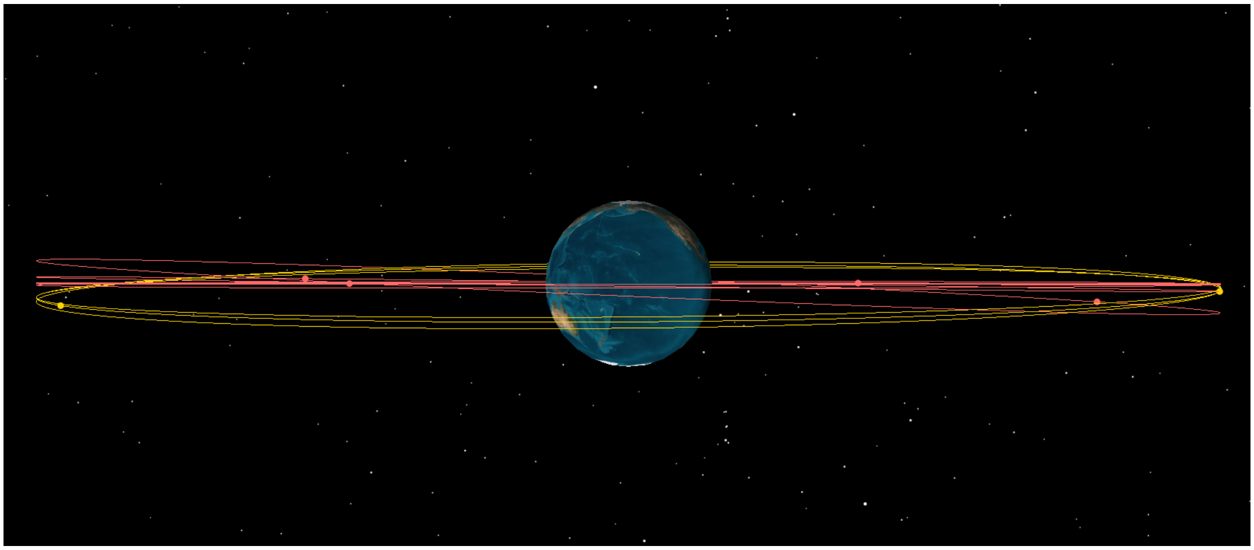

(b)

Figure 2(a,b): The GEO orbit of two of Inmarsat's satellites, one satellite is designated in pink and the other satellite in yellow

The satellites have an altitude of approximately 35,795 km, an inclination of 2.56 degrees, an eccentricity of 0.0003, and a semi-major axis of 42,166 km. Satellites in GEO pass through the Earth's shadow once a day. Depending on the time of year, the length of time the satellite spends in the shadow of the Earth, or in an eclipsed state, changes. When the Earth blocks the sunlight from reaching the satellite, and in turn keeps the satellite from gaining maximum power via its solar panels, the spacecraft is forced to switch to batteries or shut down [Intelsat, 2012]. Using models for the Inmarsat solar panels incorporated in the STK 10 database, it was determined that the satellites have a maximum power generation of approximately 18,000 W. However, as previously stated, in the event of an eclipse the maximum power generation is drastically reduced.

Ultimately, whether for maintaining GPS links for national security or maintaining communication for disaster monitoring, there are benefits to better understanding the effects of space weather on satellites, as well as benefits to improving hardware designs, operational approaches, and observations for space weather forecasting. This research provides insight into all of these areas and serves as a starting point for bringing together the commercial satellite communications industry and space weather science communities to understand the sensitivity of key components to the changes of the space environment. The goal is to improve both component robustness as well as system performance using design redundancy, operational, and predictive monitoring approaches.

Chapter 2 provides a background on space weather, and specifically on energetic electrons, protons, galactic cosmic rays, and the geomagnetic space environment with associated metrics for measuring the severity of geomagnetic activity. Chapter 3 explains the historical Inmarsat telemetry archives, explains the traffic analysis of the SSPA currents and the correlation of the SSPA anomalies and SEUs occurrence with the eclipse seasons. Furthermore, Chapter 3 also contains SSPA and satellite local time assessment to determine if surface charging served as the source of these anomalies. Chapter 4 describes three data sources: the Geostationary Operational Environment Satellites, the Advanced Composition Explorer, and the World Data Center for Geomagnetism in Kyoto. Chapter 4 also contains a predicted AE-8 Radiation model for the geostationary communication satellites using ESA's SPENVIS tool, and a definition of severe space weather event. Next, Chapter 5: Space Weather Correlation, contains the bulk of the analysis for this research. It begins with an investigation of the SSPA anomalies and the geomagnetic space weather environment, followed with the SSPA anomalies and charged particles analysis. Then it transitions into the single event upset portion of the study, and investigates the solar energetic proton environment, and investigates the relationship between SEPs and SEUs. Lastly, in Chapter 6 we discuss our finding and develop plans for future work.

CHAPTER 2: SPACE WEATHER BACKGROUND

Space weather consists of diverse phenomena that originate from disturbances on the sun and lead to deviations in the space environment. The sunspot number is a metric used to assess the overall strength and fluctuation of solar activity, such as solar flares and coronal mass ejections (CMEs). The increase and decrease in sunspot number defines the solar maximum and solar minimum. At solar maximum there is an increased chance of solar flares, CMEs and other solar phenomena. However, even at solar minimum the Sun can produce damaging storms [Cole, 2003]. When the solar activity fluctuates between a high and low sunspot number it defines the solar magnetic activity cycle, a period of approximately eleven years.

Figure 3 depicts the solar cycle between 1995 and 2012. This period encompasses Solar Cycle 23 (May 1996 – Dec. 2008) and Solar Cycle 24 (Jan. 2009 – present). The solar maximum for Cycle 23 occurred approximately between 1998-2002, and the solar minimum occurred approximately between 2006 and 2009. The solar maximum has yet to occur for Cycle 24. The data for this plot are from the Royal Observatory of Belgium's Solar Influences Data Analysis Center [SIDC, 2003].

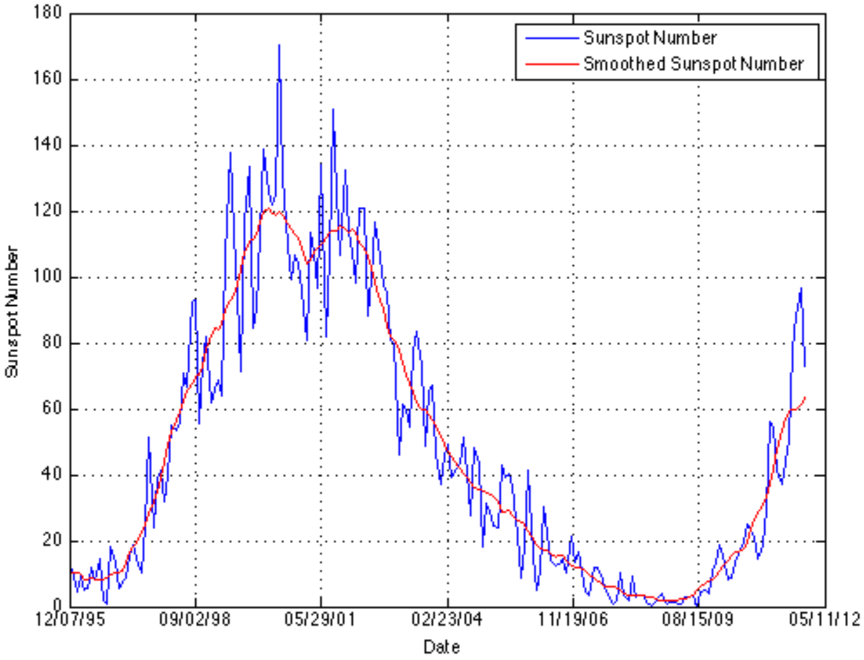

Figure 3: The Solar Cycle

A constant flow of radiation, plasma, and energetic particles originates from the Sun in the form of solar flares and CMEs, and are carried through the solar system via solar wind. The violent solar eruptions of CMEs release plasma with up to one hundred billion kilograms of electrons, protons, and heavy nuclei that travel near the speed of light with the capability of producing major geomagnetic storms. These charged particles, super-heated to tens of millions of degrees make CMEs one of the worst types of space weather phenomena to encounter satellite hardware [Gopalswamy, 2006]. If the interplanetary magnetic field (IMF) is oriented such that the Bz component is southward the particles from the CME can enter the earth's magnetosphere and cause magnetic storms [Fennel et al., 2001].

These bursts of energy and mass leave footprints on the surface of the sun known as sunspots, well-defined areas of cooler temperatures on the Sun's surface that appear as regions of dark spots. At these surface locations, strong magnetic field fluctuations can cause the energy and matter to become unstable and launch into space. CMEs and solar flares send charged particles and intense magnetic fields into the Earth's magnetosphere, ionosphere, and thermosphere. Solar flare X-rays can reach Earth's surface in eight minutes (i.e., at the speed of light), whereas solar energetic particles take closer to an hour. The highly energetic particles, ranging from ten to hundreds of MeV, deposit themselves into the surface and electronics of spacecraft, and are one of the most common causes of satellite anomalies [Baker, 2002].

During geomagnetic storms, and particularly solar proton events, charged particles are capable of penetrating the surface of satellites and bombarding the spacecraft's electrical components, which can ultimately lead to an electrical breakdown.

Energetic Charged Particles

Radiation, or traveling energetic particles, is one of the most common causes of satellite anomalies. During geomagnetic substorms and proton events, charged particles are capable of penetrating the surface of a satellite and bombarding the spacecraft's electrical components, which can ultimately lead to an electrical breakdown. When considering geostationary satellite systems, the primary particles of interest are low-energy electrons, high-energy electrons and high-energy protons. These three types of particles are notoriously considered the sources of surface charging, bulk dielectric charging, and single event upsets, respectively, and are described in the following three sections.

Geostationary satellites are located in the outer radiation belt, an area where energetic electrons, not protons are trapped. When a spacecraft is in contact with the hot solar plasma it becomes surrounded in traveling electrons, and ultimately becomes negatively charged [Vampola et al., 1985]. If the electric field generated from the hot plasma exceeds the breakdown field on the surface of the spacecraft the electromagnetic interference or arcing can occur [Fennel et al., 2001]. Thus, stressing the importance for spacecraft designs capable of tolerating electrostatic discharge, or keeping the differential charge surrounding the spacecraft below the breakdown potential at which arching occurs [SMAD III, 1999].

Low Energy Electrons

The expulsion of low-energy electrons, ranging in energy between approximately 10-100 keV, is a hazardous result of magnetospheric substorms. When these low-energy electrons interact with GEO satellites, they deposit their charge onto the surface of the satellite, but they are typically too low in energy to penetrate the structure's surface [Baker, 2000]. However there have been rare instances where electrons above 25-30 keV have penetrated the surface [Fennel et al., 2001].

The accumulation of charged particles on insulating surfaces can lead to a buildup of charge, and ultimately cause arcing or electrostatic discharge (ESD). However, instead of developing in the dielectric materials of the spacecraft, the charge buildup occurs on its surface. If inadequate electrical connections exist between the solar arrays and surface materials, then differential charging on the surface can cause lightning-like breakdown discharges between the materials [Vampola et al., 1985].

Surface charging at GEO is directly related to local time and the geomagnetic environment. It became clear in the 1970's that anomalies on geostationary satellites occurred in the near midnight to dawn region of the magnetosphere. During the initial phase of a geomagnetic substorm electrons are injected from the magnetotail into the night side of the magnetosphere, and tend to cause a surface charging on the night side of the earth, between midnight and dawn. The sunlit areas of the satellite are generally positive in charge whereas the shadowed areas are negatively charged, with respect to the surrounding plasma, which is the primary source of current that causes charging [Fennel et al., 2001].

High-Energy Electrons

Relativistic electrons (with energies greater than ~300 keV), are commonly referred to as high-energy electrons and cause deep dielectric or bulk charging. Bulk charging generally occurs hours to days after large magnetic storms and results from high-energy electrons that penetrate the surface-shielding material of a satellite. Once the electrons penetrate the surface, they can deposit into the spacecraft's thick dielectrics, including cables, conductors and circuit boards. Interaction with high-energy electrons can significantly change the electrical properties of dielectric materials. If bulk charging occurs at a rate greater than the existing charge can escape from the dielectric, then a breakdown can possibly occur [Fennel et al., 2001]. A breakdown generates a fast pulse, 100 nanoseconds or less, on connected devices and discharges energy into sensitive electronic circuits.

An electrical discharge occurs when the field between two materials accumulates and exceeds a critical threshold. Often, discharge stems from sharp flux changes, or when surfaces have different conductivities [Gubby, 2002]. Discharges can introduce noise into the system, cause interference, cause serious component damage, cause a bit flip, or completely interrupt spacecraft operation [Lanzerotti, 2001]. Thus space weather variations can significantly change the electrical properties of dielectric materials.

At GEO, the intensity of high-energy electrons can penetrate spacecraft shielding, cause differential charging, and ultimately cause electronic circuitry short, burn out, or malfunction, leading to wider satellite failures. These high-energy electrons are at a maximum during the declining phase of the solar cycle, when high-speed solar wind streams occur [Shea, 1998; Miyoshi, 2008]. Furthermore, it was found that internal discharging peaks near local noon rather than between midnight and dawn, as with surface charging [Fennel et al., 2001]. Fennel also highlights that internal charging is largely a function of spacecraft shielding and orbit, as satellites that spend long periods of time in high flux regions require thick shielding.

High-Energy Protons

High-energy protons, or solar energetic protons (SEPs) of greater than 10 MeV, and originate from CMEs. In less than two days after the CME, these particles penetrate the Earth's magnetic field at the poles, crash into atmospheric particles, and produce ion and electron pairs that temporarily increase the plasma density in the lowest regions of the ionosphere [Baker, 2000; Baker, 2002]. This causes absorption of short wave radio signals and widespread blackout of communications, sometimes called a polar cap absorption event. Dangerous levels of high-energy particle radiation build up in the magnetosphere; this radiation can damage spacecraft microelectronics and pose a serious threat to the safety of astronauts. Energetic proton events can cause increased noise in photonics, total dose problems, power panel damage, and single event upsets.

The term SEU is commonly used within the satellite industry to indicate when high energy-particles cause electrical interference such as a ‘bit flip’, physical damage, and even component failure [Baker, 2011]. In severe cases, SEUs can cause satellites to lose control and tumble, potentially leading to satellite failure. SEUs can occur at any point throughout the eleven-year solar cycle, but are found to mostly occur near solar minimum, between the second and ninth year of the typical 11-year solar cycle[2]. The causal relationship between high-energy protons, SEUs and solar array degradation is of particular interest to the communications satellite industry as these interactions are not well understood.

Galactic Cosmic Rays

The second source of particles that cause SEUs are galactic cosmic rays (GCR). GCRs consist mostly of protons (84% hydrogen) along with alpha particles (15% Helium) and less than 1% of heavier nuclei, and result from supernova explosions that spread cosmic rays [Baker, 2000; Wilkinson, 1991]. These rays have energies up to 10^{14} MeV and occur out of phase with the eleven year solar cycle; the radiation from GCRs peaks at solar minimum and reaches a minimum at solar maximum [Riley, 2012; Wilkinson, 1991]. At solar minimum, the solar winds are low and allow GCRs to reach the magnetosphere. This does not usually occur at solar maximum because the solar winds inhibit the GCRs from entering a trajectory towards the magnetosphere and the geostationary satellites. GCR data is not analyzed in this study, but will be included in future work, as strong GCRs can also cause significant SEUs [Baker, 1998].

The Geomagnetic Space Environment

The Earth’s magnetic field consists of an inner and an outer radiation belt, which are more formally referred to as the Van Allen radiation belts. The inner belt lies between 1.2 and 1.8 Earth radii, or 4000 km from the Earth’s surface, and traps energetic protons greater than 10 MeV in flux. On the other hand, the outer radiation belt is at 2.5-6.6 Earth radii and contains energetic electrons greater than 2 MeV in flux [Cole, 2003]. Inmarsat’s communication satellites are situated at geostationary orbit, and thus are located in outer radiation belt where energetic electrons are trapped.

The radiation belts and traveling solar wind define the shape of the magnetosphere, whereas the boundary of the magnetosphere is known as the magnetopause. The primary purpose of the magnetosphere is to shield the Earth and its surrounding magnetic field from harsh solar winds. However, due to the variability in the magnetic field and solar wind, COMSATs are occasionally situated outside of the magnetosphere where they are immersed in hot solar plasma originating from solar winds and GCRs.

Geomagnetic Indices

The strength of the Earth's magnetic field can be measured using a number of different indices. Two of the most commonly used indices used for describing geomagnetic storms are Kp and Disturbance Storm Time Index (Dst).

Kp is the general planetary index used for qualitatively characterizing the high latitude geomagnetic environment. This parameter is determined from a network of ground-based magnetometer measurements, and is the weighted average of the maximum value of the horizontal component of the magnetic field during a three-hour period [Thomsen, 2007; Balch, 2011]. The Kp scale spans from zero to nine, where nine describes the highest level of severity for geomagnetic storms.

The second metric for geomagnetic activity is Dst. Dst is inferred from the ground measurements of the fluctuations of magnetic field in the equatorial plane and indicating the strength of the ring current. Dst is the mean of the horizontal component of the Earth's magnetic field measured at four ground-based observatories located in Hawaii, Puerto Rico, South Africa and Japan. For "typical" magnetic storms Dst undergoes the following phases [Mursula, 2005]:

1. Nominal Phase: Before a magnetic storm, Dst measures approximately zero; this is the condition for a quiet day, or a period of low geomagnetic activity.
2. Main Phase Stage 1: As the magnetic storm begins, the Dst will initially increase due to the compression of the magnetosphere that occurs from interplanetary shocks in the initial phase of the storm.
3. Main Phase Stage 2: Dst drastically decreases as the intensity of trapped particles heightens.
4. Recovery Phase: After the strength of the magnetic storm peaks (occasionally on the order of -400 nT), Dst will begin to increase back toward its baseline value.

Figure 4 shows the four phases of a magnetic storm, and provides an example of the Dst during a severe geomagnetic storm.

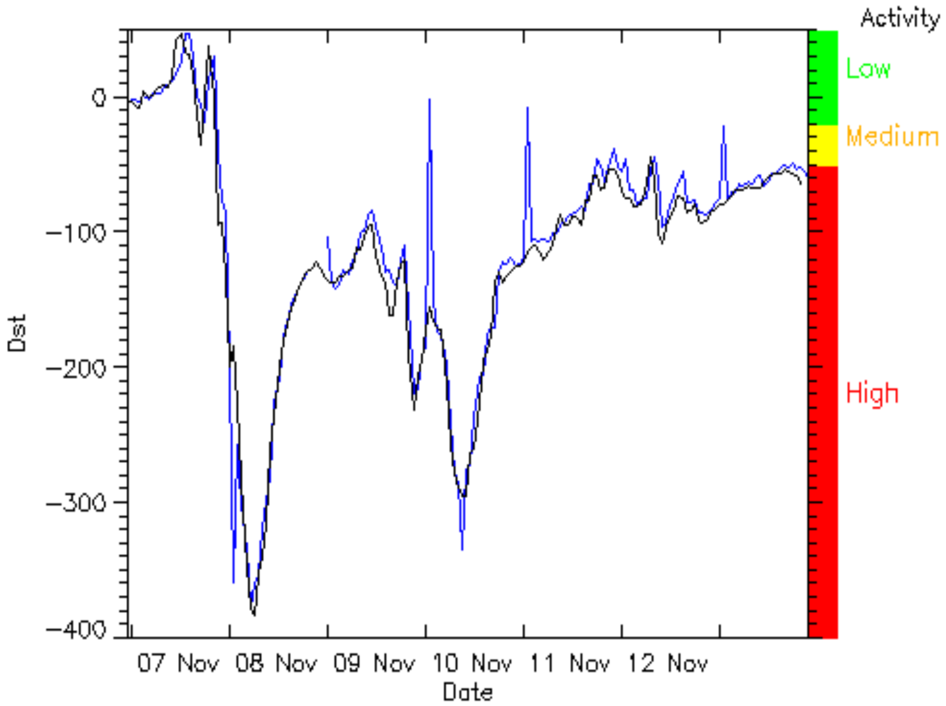

Figure 4: Example of Dst phases of activity in early November 2004 [NASA SPOF, 2006]

During a magnetic storm Dst becomes negative, because as the intensity of the storm increases as the number of electrons and low-energy ions located in the magnetosphere increases [Fennel et al., 2001]. These energetic particles comprise the “ring current.” As ring current increases during magnetic storms, Dst decreases because it is inversely proportional to the energy of the ring current [Cole, 2003]. However, once the interplanetary magnetic field returns toward more nominal values, the ring current returns to a quiet level and Dst increases. At lower latitudes, the magnetic strength on the surface of the Earth is proportional to the energy of the ring current [Mursula, 2005]. This relation is the Dessler-Parker-Sckopke relation [Bono, 2005]. The Geomagnetic Equatorial Dst Data Service is hosted by the World Data Center for Geomagnetism in Kyoto, Japan. This database was used for acquiring values of Dst at times of anomalous satellite component behavior and was also used to determine dates for severe geomagnetic space weather events between 1996 and 2012.

Like the solar activity, geomagnetic space weather activity is also cyclical. However, unlike the solar cycle, the geomagnetic cycle does not have a clear solar minimum and solar maximum. The geomagnetic cycle generally consists of two peaks that occur within a year before and after solar maximum. Furthermore, a given metric, such as the sunspot number, does not exist. This can make plotting the geomagnetic cycle relatively difficult, and explains why there have been multiple approaches to plotting this cycle.

Allen notes the differences between the solar cycle, shown in yellow, and geomagnetic cycle, shown in red of Figure 5. Their method for depicting the geomagnetic cycle is to plot the number of days the value of Ap was greater than or equal to 40. Ap is the 8-value average of the 3-hourly ap values for each UT-day [Allen, 2004]; ap is the three-hour equivalent range derived the Kp metric [Balch, 2012].

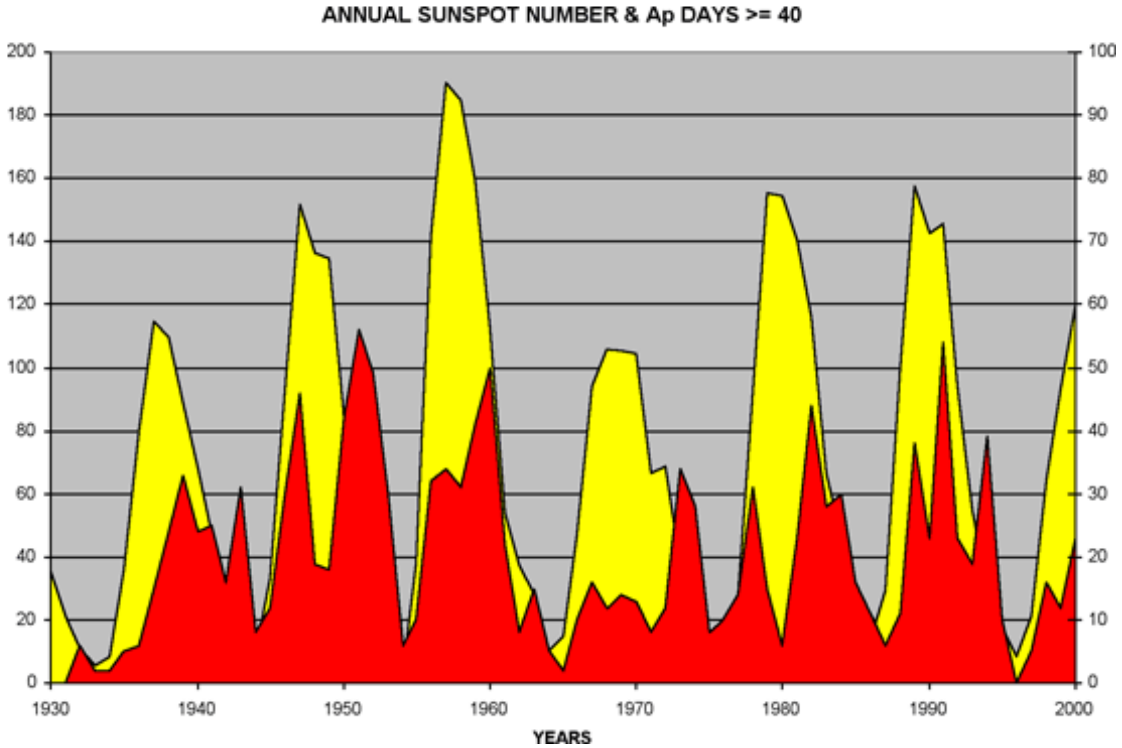

Figure 5: Annual sunspot number and Ap days >=40 [Allen, 2004]. Sunspot number is shown on the left vertical axis, and Ap is shown on the right vertical axis.

Figure 5 shows that the geomagnetic cycle has the same 11-year period as the solar cycle, and that there is always one peak in the geomagnetic cycle during the declining portion of solar cycle. However, it is clear that the geomagnetic cycle is not as definitive as the solar cycle in terms of maximum and minimums. For this reason, the geomagnetic cycle is less frequently used in analysis.

An alternative approach to show the geomagnetic cycle is to plot the annual number of times Dst reaches a specified value. Different values of Dst have been suggested, we chose to specify a value of -150 nT and -200 nT, because generally these values are considered extreme for severe geomagnetic events. Figure 6 shows the number of instances the Dst was less than -200 nT, and less than -150 nT, from 1957 to 2012. The year 1957 is the earliest verified Dst data from World Data Center for Geomagnetism in Kyoto, Japan.

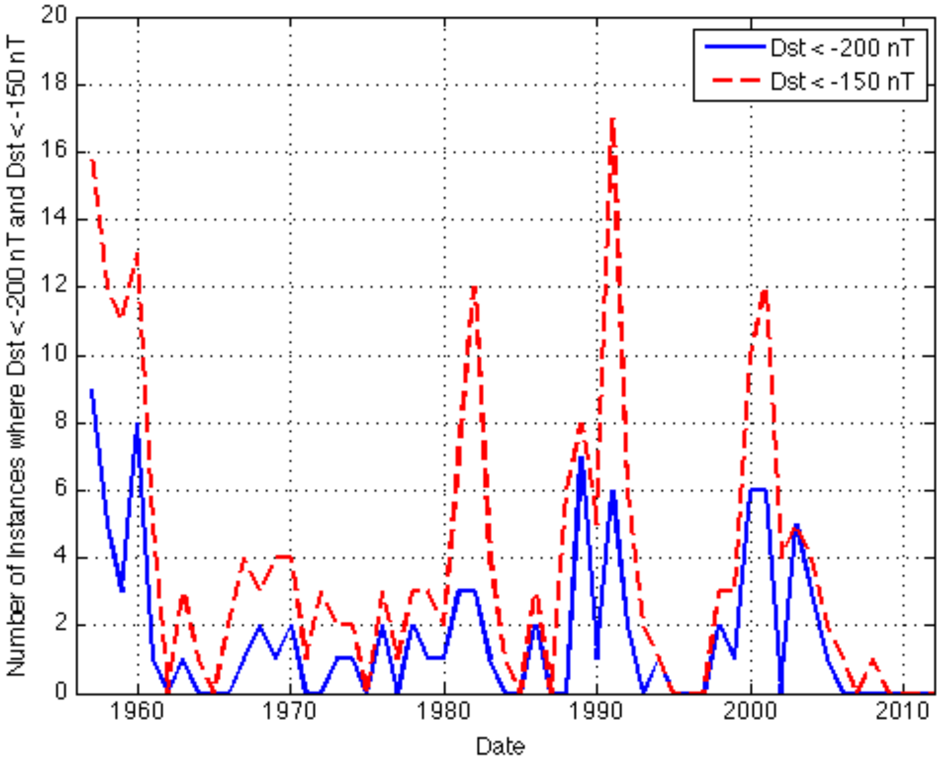

Figure 6: The Geomagnetic Cycle

The purpose of this plot is to clarify the geomagnetic cycle. As expected, the two scenarios, Dst less than -200 nT and Dst less than -150 nT, follow the same general trends, but with different amplitudes. Interestingly, since 2006 it is the first time zero instances of severe geomagnetic storms have occurred for more than three years. The three-year periods of zero severe geomagnetic storms began in 1964 and 1995. It has currently been six years since the last severe geomagnetic storm of a Dst less than -200 nT.

CHAPTER 3: DATA FROM INMARSAT

To better understand and mitigate the effects of space weather on the performance of its satellite fleet, Inmarsat, one of the world's leading providers of global mobile satellite communications services, has partnered with MIT and researchers in the space weather community. This partnership focuses on correlations of space weather with satellite component and system performance, and methods for mitigating potential degradation.

The effects of space weather can greatly inhibit the performance of geostationary communication satellites and their ground stations. However, much work remains to be completed in order to achieve an in-depth understanding of the specific types of space weather events that significantly impact component health, and the necessary methods for mitigating component failures. Understanding the causal relationship between space weather and component health is important because this knowledge will help improve the robustness of satellite hardware and thus improve the services that satellite operators provide to their customers.

Furthermore, the space radiation environment is an important aspect of satellite design that should be accounted for to meet the satellite's performance and lifetime requirements. Advances in technology have led to a reduction in the size of satellite components – on the micro and nano scales –, which inadvertently has increased their susceptibility to the effects of space weather [Baker, 2000; Wilkinson, 1991; Gubby, 2002]. Electrical upsets, interference, and solar array degradation are just a few of the known effects of the space environment. In fact, as a result of space weather, satellite operators are occasionally forced to manage reduced performance or fully decommission satellites, amounting to social and economic losses of several tens of millions of dollars per year [Baker, 1998]. Therefore, we have conducted a correlation analysis to better understand space weather's affect on spacecraft that should improve satellite design and reduce the maintenance cost for satellite operators.

In this analysis, more than 500 MB of on-orbit component telemetry and component anomaly data for Inmarsat's satellite fleet are analyzed. Inmarsat's telemetry database is used to identify and investigate both nominal and anomalous component performance from 1990 to 2012. Data on solid-state power amplifiers and eclipse durations were analyzed, along with anomaly and SEU information for each satellite. Table 2 describes the collected Inmarsat satellite telemetry.

Table 2: Telemetry Descriptions

Telemetry Parameter	**Description**
SSPA Current	Solid-state power amplifier current
SSPA Temperature	Solid-state power amplifier temperature
Total Bus Power	Instantaneous power of the main power bus, power values are calculated from prime and redundant voltage and current sensors on the main bus
Solar Panel North/South Short Circuit Current	Output of the short-circuit cell current sensor located on the outboard panel of the north and south wing, used to determine when satellites are in eclipse
Solar Panel North/South Open Circuit Voltage	Output of the open-circuit cell voltage sensor located on the mid-board panel of the north and south wing

SSPAs are key components for accurately transmitting signals in communication systems, and provide advantageous reliability, ruggedness, size and cost compared to alternatives such as traveling wave tube amplifiers [Sechi, 2009].

The Solid State Power Amplifier (SSPA)

The primary task of solid-state power amplifiers is to increase the power of an input signal to a predefined level. For spacecraft applications, amplifiers are needed because the input communications signal is often degraded due to the atmosphere, through which it must emit to reach the satellite. Therefore, the signal must be amplified, or the power of the signal must increase, to restore the original signal and accurately transmit the signal to the end user. The two most important performance parameters of SSPAs are output power level and power gain The gain of an SSPA, G, is the ratio of the output to input power and is generally measured in decibels, dB [Colantonio, 2009].

SSPAs are non-linear components, yet the device can operate linearly when the amplitude of the input signal is low. As the input signal increases it reaches a level where the output power of the signal saturates [Sechi, 2009]. Amplifiers on communication satellites are generally operated slightly below saturation. The maximum power output with the highest efficiency occurs at the saturation point, however the risk of signal distortion occurs when the input power is beyond the "operating point". The specific operating point should be optimized for the individual satellite [Elbert, 2002].

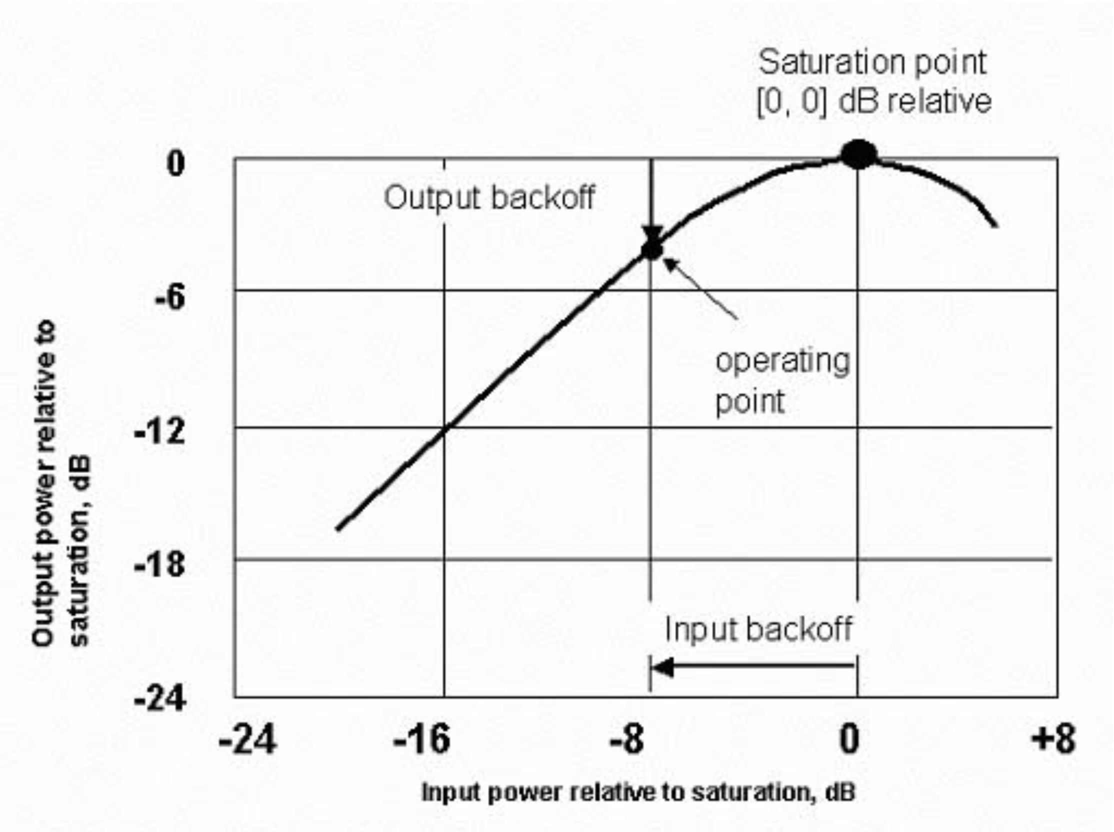

Figure 7: Saturation curve of an amplifier [Elbert, 2002]

In terns of energy, SSPAs convert DC power into microwave energy power. Efficiency, expressed as a percentage, is the amplifiers ability to convert the DC power into microwave power, and is also referred to as drain efficiency. Ultimately, efficiency determines the power supply of the amplifier. A high efficiency amplifier provides high-transmitted power and increases the overall system performance [Colantonio, 2009].

The European satellite bus manufacturer, EADS Astrium, equips several of their designs with a L-Band SSPA. This 0.75 kg amplifier, shown in Figure 8, is specifically used for mobile communication phased array antennas, which require tight gain and tracking performance with superb Dc/RF conversion efficiency. The SSPAs provide 15 W output power capability. Additional features of this amplifier include 5 degree phase tracking, 0.5 dB gain tracking, peak efficiency of 32%, production rate of 15/week, and spin off products in S and navigation bands. In the past, these amplifiers have flown on several ESA and Inmarsat satellites [Astrium]. Figure 8 shows the EADS Astrium L-Band SSPAs.

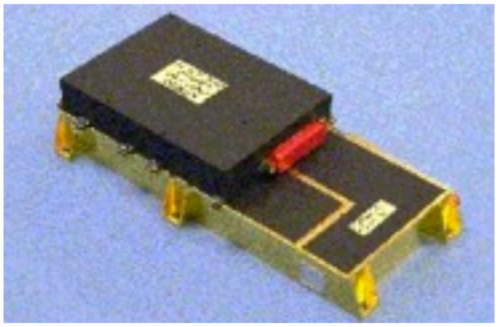

Figure 8: EADS Astrium L-Band SSPA with dimensions of 217 mm x 107 mm x 47 mm

A satellite anomaly occurs when a component operates outside of its defined threshold for nominal performance. Thresholds are established to monitor the health of components, and notify operators when the component experiences anomalous performance, which limit the operational lifetime of the satellite. For SSPAs, the main threshold of concern is the amplifier current. The SSPA current determines the amplification capability of the device. When the amplifier is irradiated the semiconductor material (such as silicon or Gallium Arsenide) is affected by surface charging, deep dielectric charging from relativistic electrons, or impact from high energy more massive particles such as protons. Over an undetermined period of time, this results in a change in conductivity of the material and thus leads to a change in current, which is a parameter monitored and tracked in housekeeping telemetry. If the current exceeds the upper threshold the SSPA will saturate, and if the current exceeds the lower threshold the SSPA will not provide enough current to adequately amplify the signal. Therefore the effects of space weather can cause the amplifiers to operate insufficiently and even cause amplifier anomalies.

Traffic Analysis of SSPA Currents

Over the course of a spacecraft's lifetime, component health and performance degrades as a result of exposure to space weather [Baker, 2000]. These anomalies are often assumed to result from the taxing launch environment and maneuvers that a satellite experiences within the first two years of operation. Anomalies that occur within the first two years of operation can pose challenges when analyzing the source of anomaly, as correlations between anomalies and space weather events may be confused with anomalies from the launch environment. Thus, it suggests that space weather should be monitored as a cause of anomaly at all stages or the spacecraft's life.

Figure 9 shows the age, or number of years after launch, of the satellites when an SSPA anomaly occurred. The age has been approximated to the closest whole year, so 4.6 years is recorded as 5 years. For the second satellite fleet, most anomalies are shown to occur in the first two years of operation. Anomalies that occur during the first two years of a satellite's life are sometimes due to the extreme conditions that the sensors experience during launch and during the maneuvers to reach the allocated orbital slot. However, it is possible that these anomalies are not "burn-in" or transition effects but could be due to harsh space weather events. Seven of the twenty-six anomalies occurred in the first two years of the satellites lifetime, and 6/7 anomalies occurred within two weeks of a severe radiation space weather event caused from relativistic electrons.

Inmarsat satellites have an expected lifetime of fifteen years. One can expect that as the satellite increases in age the likelihood of anomalies should also increase. Nonetheless, there is not an obvious increase in Figure 9 because the two co-plotted fleets consist of satellites at different points in their expected lifetime. While the satellites in the first fleet are up to fifteen years old, the satellites in the second fleet are at most six years old.

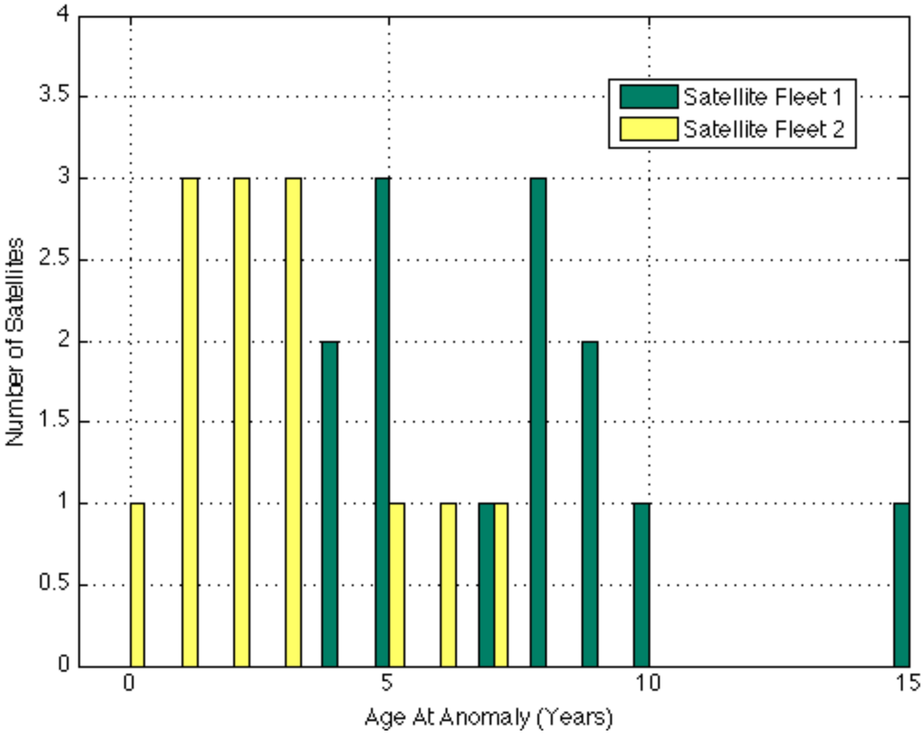

Figure 9: Satellite Age at time of SSPA Anomaly including anomalies that occur within two years of launch [Lohmeyer, 2012]. The two different color bars, yellow and green, designate two different satellite fleets.

The eight Inmarsat satellites considered in this analysis have each experienced between zero and eight SSPA anomalies. These anomalies have occurred as early as in first three months of operation and as late as at nearly fifteen years of operation. Figure 9 shows that at age 1, 2, 3, 5, and 8 years after launch the same number of anomalies occur (3 each). We again note that the satellite fleets have different designs and SSPA configurations.

Nominal SSPA currents over the lifetime of each satellite have inherent periodicities as a result of traffic, or customers using Inmarsat's communication services. Figure 10 is the single amplitude spectrum for a nominal SSPA. As depicted, the most prevalent periodicities are one week, one day, a half of a day, a third of a day and a quarter of a day.

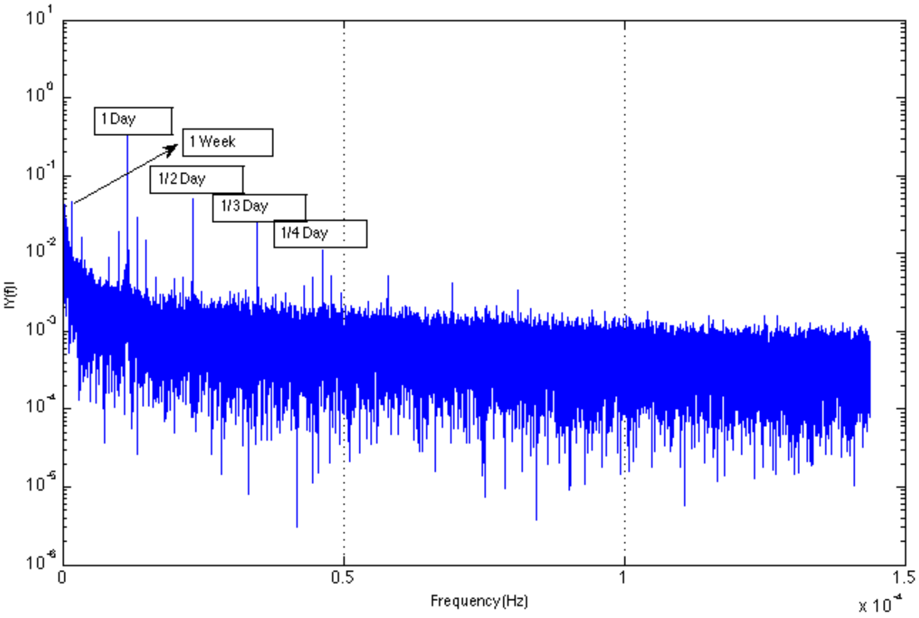

Figure 10: Single Amplitude Spectrum of Nominal SSPA

We observed some cases where the frequency spectrum of an anomalous SSPA showed periodicities in addition to those shown for a nominal SSPA in Figure 10. In the nominal case, we expect periodicities to be related to traffic and the diurnal cycle. Figure 11 shows an example of the single amplitude spectrum of an anomalous SSPA, where periodicities of 1 day, 1 week, half of a day, one third of a day and a fourth of a day are clearly present, in addition to higher power clusters of harmonics.

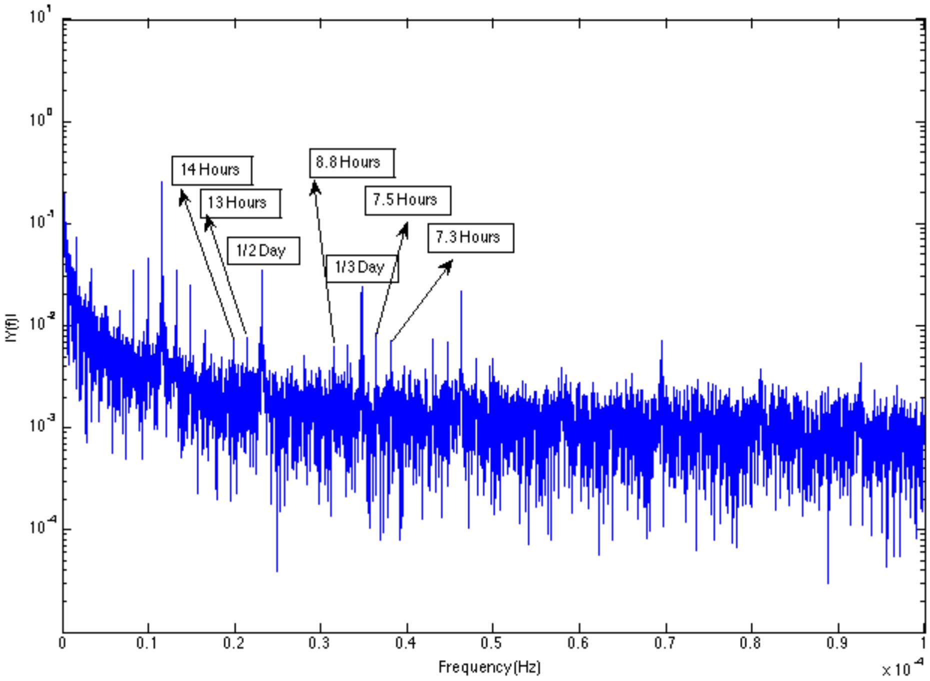

Figure 11: Single Amplitude Spectrum of Anomalous SSPA

The periodicities on a larger scale, such as months, imply that seasonal trends exist. Seasonal trends suggest that that the SSPA data is dependent on solar activity, and motivates the investigation of relationships between anomalies and eclipse seasons, as well as anomalies and space weather in a more general sense.

Correlation of Anomalies and SEUs with the Eclipse Seasons

The Earth's orbit, while not truly circular, revolves around the Sun along the ecliptic plane, which is 23.5 degrees from the Earth's rotational axis. Regardless of the year, the Earth's rotational axis maintains this orientation and pointing direction. As a result of the rotational tilt angle and the Earth's rotation about the Sun, seasons occur, making longer periods of daylight in the summer and shorter periods of daylight in the winter. As the satellites approach autumn and spring, they enter equinox, which is approximately 21 days long. In the initial days of equinox the eclipse duration, or amount of time the sunlight is blocked, last for ~ 1-2 minutes, yet when the Sun reaches equinox the duration of eclipse can increase up to 72 minutes [Intelsat, 2012].

Generally, geostationary satellites have a direct view of the sun and are able to utilize energy from the solar panels as a power source. However, during an eclipse the Earth blocks sunlight from reaching the solar arrays and forces the satellite operators to monitor and control power management during the known eclipse seasons.

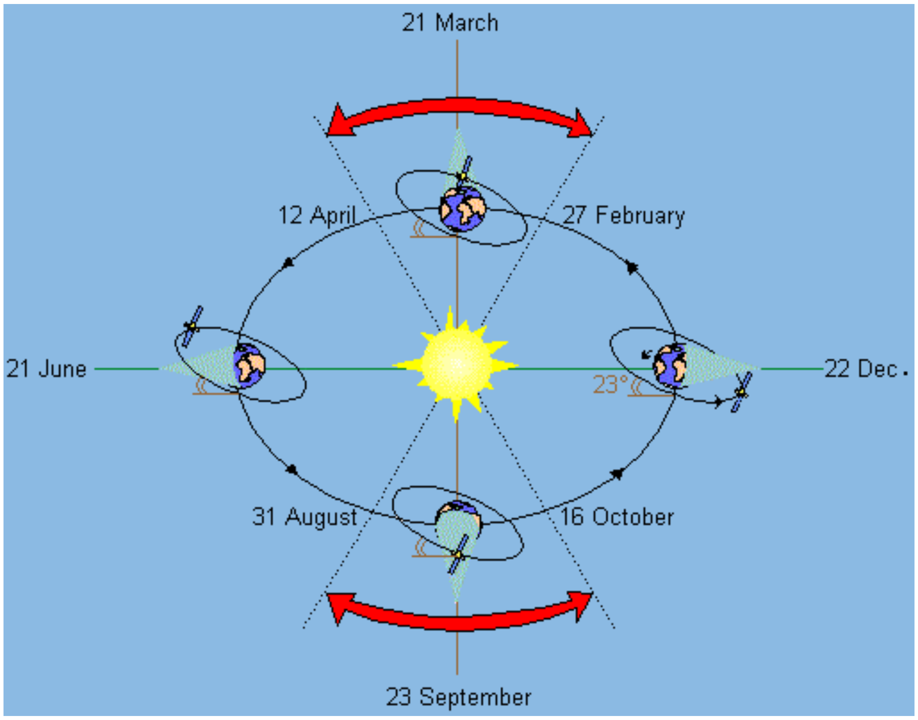

Figure 12: Eclipse Seasons [CNES, 1979]

In this work, the start and end dates of eclipse season as well as the longest eclipse duration times for the four satellites with the highest traffic levels were tracked. The Inmarsat recorded eclipse dates are displayed in Table 3, and are slightly longer than the eclipse periods denoted by the red arrow in Figure 12. To simplify the table, instead of listing the annual range, the earliest eclipse start date since 1996, and the latest eclipse end date are listed. The period in the center of the eclipse season where the longest eclipse durations occur does not exceed ten days. For example the longest eclipse start and longest eclipse end for Satellite W occur from March 16-24, a period of nine days.

Table 3: Summary of Eclipse Durations

Satellite	Spring Season Start	Spring Season End	Longest Eclipse Start	Longest Eclipse End	Fall Season Start	Fall Season End	Longest Eclipse Start	Longest Eclipse End
W	Feb. 25	April 15	March 16	March 24	Aug. 30	Oct. 19	Sept. 21	Sept. 26
X	Feb. 26	April 19	March 16	March 24	Aug. 30	Oct. 20	Sept. 21	Sept. 26
Y	Feb. 26	April 18	March 22	March 26	Aug. 30	Oct. 22	Sept. 25	Sept. 29
Z	Feb. 26	April 20	March 21	March 27	Aug. 30	Oct. 23	Sept. 21	Sept. 29

Lunar eclipses require a less intensive procedure because they only occur once or twice a year, and do not produce significant discharges. Regardless, in the event of a lunar eclipse operators instruct the satellites to enter eclipse mode because the onboard propagators do not track the moon's location.

The two eclipse seasons are from late February to mid-April and late August to late October; the longest eclipses generally last between 68 to 73 minutes [Lohmeyer, 2012]. The eclipse seasons coincide with the vernal and autumnal equinox, because during equinox the Earth blocks the Sun's light from reaching the satellites. Interestingly, the SSPAs are not primarily found to occur during equinox, but occur more so in the two solstice periods.

Table 4 shows the season in which each of the twenty-six SSPA anomalies occur. The specific satellite longitudes are kept anonymous to protect competitive advantage. Interestingly, the majority of the SSPA anomalies does not occur during the eclipse seasons, but instead occur between November and January, during the northern winter solstice. The northern equinoxes coincide with the fewest number of SSPA anomalies. Based on these data, it appears that the geometry of the Earth eclipsing the sun in addition to the measures taken by the operators during eclipse seasons for power management seem to reduce the number of SSPA anomalies. As shown in Table 4, ten and seven anomalies occur over solstice periods, compared with three and six anomalies in periods of eclipse.

Table 4: The number of SSPA anomalies that occur during different seasons

Satellite	Nov. – Jan. Solstice	Feb. – April Equinox	May – July Solstice	Aug. – Oct. Equinox
A	1	0	0	1
B	3	0	3	0
C	2	1	1	1
D	2	0	0	0
E	0	0	1	0
F	1	2	1	4
G	1	0	1	0
Total	10	3	7	6

During these two eclipse seasons, satellite operators pay particular attention to monitor and control power management of the satellites as the Earth blocks the sunlight from reaching the solar panels [Lohmeyer, 2012]. ESD is found to occur during rapid changes in potential associated with the beginning and end of the eclipse seasons [Fennel, 2001]. Based on this data, it appears that the additional measures taken during eclipse seasons to protect the satellite components also reduce the number of SSPA anomalies, as ten and seven anomalies occur in periods of solstice, and three and six anomalies occur in periods of eclipse. It should also be noted that solstice periods, which coincide with spring and fall, are also when geomagnetic activity is most active [Rangarajan and Lyemori, 1997].

For the SEU and eclipse analysis, the four satellites with the highest traffic were considered. Of these four satellites, two have advanced computing systems that consist of primary and secondary computers that are each susceptible to SEUs. Table 5 shows the distribution of SEUs over separate quarters of the year. However, when comparing the occurrence of SEUs with the different of eclipse seasons, no obvious correlation exists.

Table 5: Eclipse and SEU

Satellite	**Nov. – Jan. Solstice**	**Feb. – April Equinox**	**May – July Solstice**	**Aug. – Oct. Equinox**
W	2	0	2	3
X	2	4	1	2
Y primary	2	3	3	8
Y secondary	7	11	14	13
Z primary	11	12	10	8
Z secondary	12	12	7	5
TOTAL	36	42	37	39

SSPA Anomalies and Satellite Local Time

Choi *et al.* [2012] found that for 95 publicly available GEO anomalies the majority of the anomalies occur mainly between midnight to and dawn in local time. However, the anomalies were not specific to only SSPAs but also include a variety of failures including electrostatic discharge and power outage. In Figure 13, we plot the local time of each of the 26 SSPA anomalies on the eight Inmarsat satellites. In future work, we will consider the temporal distribution of anomalies and their relationship to different types of charging. For example, anomalies associated with internal charging should be equally distributed in MLT, whereas surface charging should preferentially occur in the midnight to dawn sector.

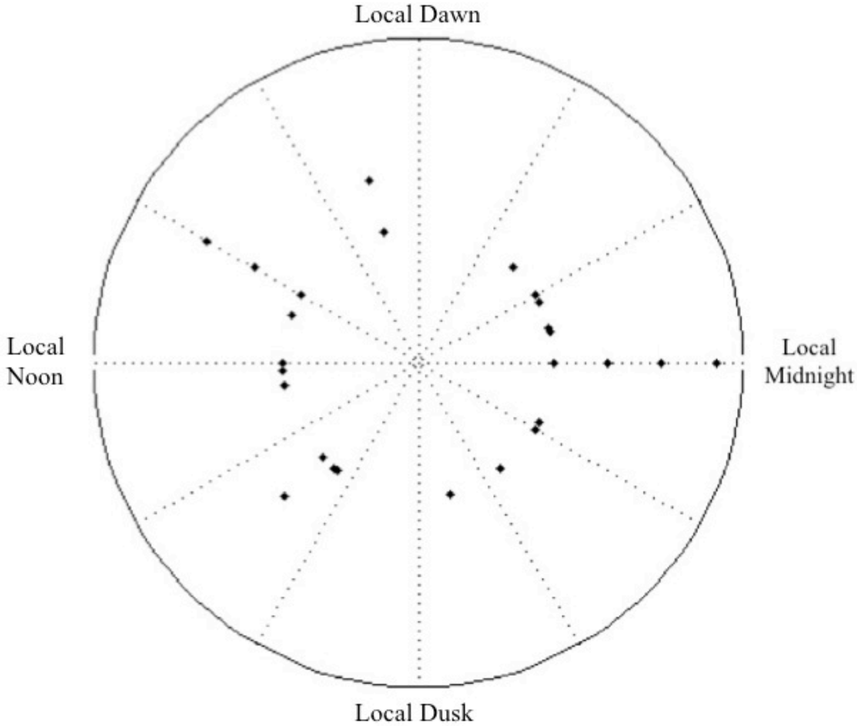

Figure 13: Satellite Local Time[1] for the twenty-six SSPA anomalies. The radial distance from the center of the plot shows the number of anomalies that occurred, as at local midnight, when four (15%) SSPA anomalies occurred.

The 26 SSPA anomalies we have, from two different fleets, may not be sufficient to draw clear conclusions on time dependence, although they are all from the same type of component failure. However, we will summarize their current distribution. Nine (35%) occur between midnight and 06:00 local time. This is the largest distribution of anomalies compared to three other six-hour periods (midnight – 06:00, 06:00 – noon, noon – 18:00, 18:00 – midnight). Seven of 26, or 27%, occur between 06:00 and local noon, as well as seven between local noon and 18:00. Lastly, four of the 26 SSPA anomalies occur between 18:00 and local midnight (not including midnight). It is interesting that numerous studies, e.g. *Choi et al.* [2012], *Wilkinson* [1994], and *Fennel et al.* [2001], suggest that satellite anomalies depend on satellite local time. However, a majority of

---

[1] This is LT and not MLT, which we will also investigate in future work.

[2] Galactic cosmic rays are the exception; these high-energy particles do not originate from the sun.

these anomalies may be associated with surface charging, and further investigation into the SSPA anomaly mechanism is needed to provide context.

CHAPTER 4: SPACE WEATHER DATA

For historical space weather information, the primary databases included in this study are: NOAA Geostationary Operational Environmental Satellites, the Geomagnetic Equatorial Dst Data Service in Kyoto, Japan, the Royal Observatory of Belgium's Solar Influences Data Analysis Center and the Advanced Composition Explorer Satellite.

Geostationary Operational Environment Satellites (GOES) Data

To obtain dates for severe solar storm events (X-rays), radiation storm events (SEPs and relativistic electrons), and additional data on the space environment during times of anomalous satellite component activity, the authors used the NOAA National Geophysical Data Center to obtain GOES Space Environment Monitor (SEM) data. This sensor suite has provided continuous magnetometer, particle and X-ray data since the mid-1970s, and is a primary source for public, military and commercial space weather warnings [GOES, 1996].

Table 6 shows the GOES satellites that have been active from 1996 – present. GOES 11 was not included due to technical difficulties and GOES 9 and GOES 15 were not used because of their short coverage time span.

Table 6: GOES Satellite Initial and Final Coverage Times

GOES Satellite	Initial Coverage Time	Final Coverage Time
GOES 8	Jan. 1995	June 2003
GOES 9	April 1996	July 1998
GOES 10	July 1998	Dec. 2009
GOES 11	July 2000	Feb. 2011
GOES 12	Jan. 2003	Aug. 2010
GOES 13	April 2010	Sept. 2012
GOES 14	Dec. 2009	Present (comes and goes)
GOES 15	Sept. 2010	Present

At any point between 1996 and 2012 at least two of the GOES 8 – GOES 15 satellites were collecting data. During this time, several of the GOES satellites were either decommissioned into a parking orbit or experienced technological difficulties and are thus not included in this study. Nonetheless, of the remaining GOES satellites, GOES 12 is the primary satellite used for gathering SEM data, GOES 8, 10, 13 and GOES 14 were also used when one of these satellites was located closer to the anomalous satellite and for dates outside of the and GOES 12 coverage time span.

The SEM consists of three magnetometers, an X-ray/extreme ultraviolet sensor (XRS/EUV), and an energetic particle sensor/high-energy proton and alpha detector (EPS/HEPAD). This study focuses on telemetry from the EPS/HEPAD, which measures the aforementioned particle flux throughout the magnetosphere. Specifically, the instrument consists of two energetic proton, electron and alpha detectors (EPEADs), a magnetospheric proton detector (MAGPD), a magnetospheric electron detector (MAGED), and a HEPAD [NSWPC, 2007].

For this research, the GOES EPS 2 MeV electron flux channel in five-second intervals data is used to assess relativistic electrons at the time of SSPA anomalies. Additionally, the GOES EPS

P4 proton flux channel, which measures protons between 15-40 MeV, is used to quantify the high-energy proton flux during the time of each anomaly [GOES, 1996]. GOES experts suggest that examining data up to five days prior to a satellite anomaly event is sufficient for understanding the space environment leading up to the event. Therefore for each anomaly, we have collected GOES data five days leading up to the failure, the day of the failure, and one day after.

Advanced Composition Explorer (ACE) Data

The ACE satellite has provided operational data since January 1998, and has served as a dominant source for geomagnetic storm warnings. ACE is stationed at the first Lagrangian point (L1), approximately 1.5 million km from the Earth, and is always observing local dayside. Another beneficial aspect of the ACE satellite's stationary location is that in combination with the solar wind speeds, one can calculate the time at which the solar wind carrying energetic particles should contact Earth [NSWPC, 2007]. The ACE Real-Time Solar Wind System (RTSW) consists of four instruments: Energetic Ion and Electrons (EPAM), Magnetic Field Vectors (MAG), High Energy Particle Fluxes (SIS), and Solar Wind Ions.

The ACE Satellite's Solar Wind Electron, Proton, and Alpha Monitor (SWEPAM) sensor was used to quantify Level 2, or verified, solar wind speeds at the time of each SSPA anomaly. This parameter not only characterizes the solar activity during the time of the anomaly, but also provides insight into the respective magnetopause compression. If the solar wind speeds and pressure are high (600-800 km/s) then the magnetopause is likely to compress, placing Inmarsat's geostationary communication satellites outside of the magnetosphere where they are unshielded from the harsh space weather environment [ACE, 2008].

World Data Center for Geomagnetism in Kyoto

The Geomagnetic Equatorial Dst Data Service is hosted by the World Data Center for Geomagnetism in Kyoto, Japan. The Data Analysis Center for Geomagnetism and Space Magnetism is a part of the World Data Center for Geomagnetism and consists of the Data Center and the University of Kyoto's Graduate School of Science. Several types of geomagnetic indices are calculated at the center that are then verified and archived for public access (e.g. Dst). Additional parameters, such as Kp and Ap, are derived and also accessible from Kyoto [World Geomagnetic Center, 2012].

This database was used for acquiring values of Level 2 Dst and Kp at times of anomalous satellite component behavior and also to determine dates for severe geomagnetic space weather events between 1996 and 2012.

SPENVIS

The Space Environment Information System (SPENVIS), is the European Space Agency's (ESA) primary tool for modeling the effect of the space environment. The figure below was produced using SPENVIS and the NASA's AE-8 Radiation Model embedded in the tool's radiation sources and effects package. AE-8 models the trapped electron flux for a given orbit or location; for this study geosynchronous orbit was selected. This model is the most commonly used radiation model and for high-energy particles, which cause deep dielectric charging, but is not used for fluxes in the few keV range that are responsible for surface charging[8]. The locations of Inmarsat's satellites are also shown in Figure 14. It is clear that all geosynchronous satellites, not just those in Inmarsat's fleet, are subject to high electron radiation [ESA, 1997].

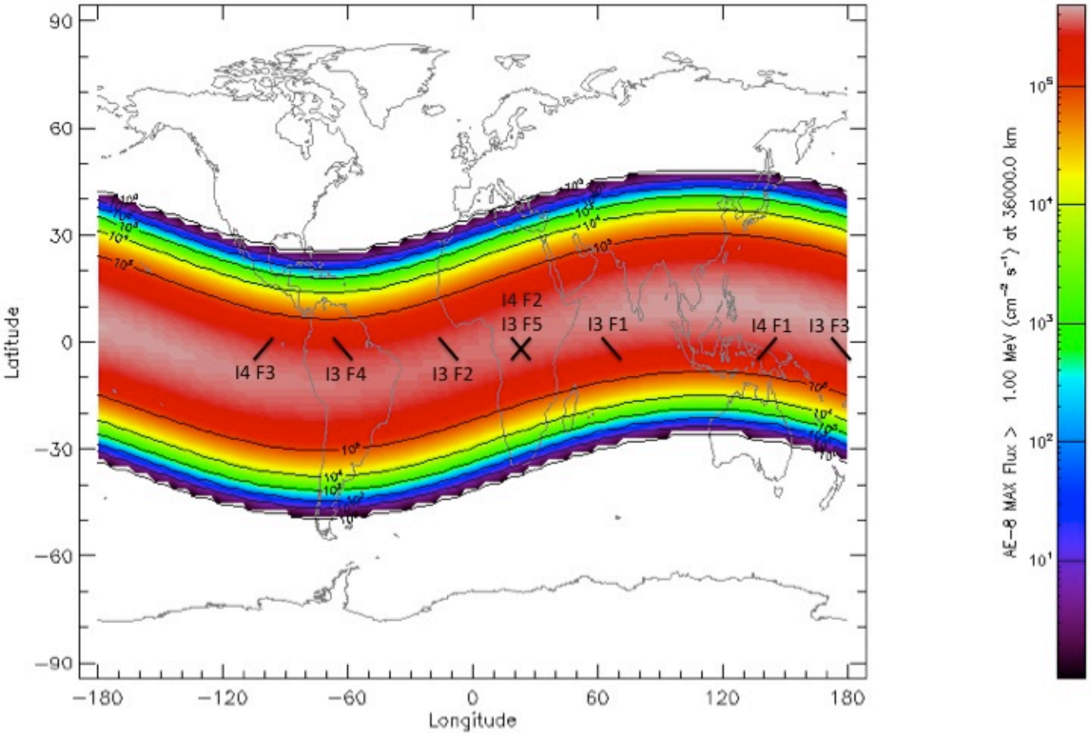

Figure 34: SPENVIS AE-8 Radiation Model with several Inmarsat locations noted.

Definition of Severe Space Weather Events

Despite a large number of available space weather observations and affiliated metrics, one challenge encountered during this analysis is that concise database of historical severe space weather events does not exist. The absence of such a resource is partly due to many different variations in the definition of "severe space weather event." Out of necessity, in this section we present the definition for a "severe space weather event" based on energetic protons and electrons, solar flares, and geomagnetic activity levels that we have employed in this work, which is summarized in Table 7.

While there are numerous databases of recorded space weather metrics (GOES, Kyoto, and ACE) a common list of historical severe space weather events does not exist. This is partly due to the multitude of variations one discovers when attempting to define the term "severe space weather event." For this work, we have developed a definition for "severe space weather event" based on four categories: (i) geomagnetic storms, (ii) energetic protons radiation storm, (iii) relativistic electrons radiation storm, and (iv) solar flare X-rays. These metrics are based on NOAA SWPC Space Weather Alerts and criteria used in recent studies throughout the space weather community [National Weather Service, 2007].

A severe (i) geomagnetic storm occurs when Dst is less than -200 nT. We tabulated when Dst was less than -200 nT using the Kyoto Dst database, which can be found in Appendix A. A severe radiation storm occurs when the 10 MeV proton flux exceeds 10,000 proton flux units (pfu, particles/sr·cm^2·s), which is S4 on the NOAA Severe Weather Scale, as well as when the 2 MeV electron flux is greater than 10,000 pfu. The radiation event dates and levels for severe radiation events from energetic protons as well as electrons can be found in Appendix B and C, respectively. NOAA sends space weather alerts when the 2 MeV electron flux is greater than 1,000 pfu, however in this work, we have defined a severe relativistic electron radiation event as that in which the 2 MeV electron flux exceeds 10,000 pfu to more clearly distinguish between the higher flux events.

Severe radiation storms were broken into two categories: (ii) solar energetic particles, and (iii) relativistic electrons, because solar energetic particles vary independently of relativistic electrons. Both types of severe radiation storms were determined from GOES data. SEPs arise due to strong flares, CMEs, and interplanetary shock waves, which can be immediate effects of solar storms. Relativistic electrons tend to occur in response to high solar wind speeds once the CMEs reach Earth or from other high-speed solar wind streams, which are essentially independent of CMEs and interplanetary shockwaves.

Lastly, a (iv) severe solar storm event occurs when solar flares exceed the X10 classification. Event date and level for solar flares greater than X10 are listed in Appendix D Flares are classified according to their maximum flux as A, B, C, M or X class flares; this is ascending order of intensity. Each class has a maximum, or peak, flux of 10 times greater than the class below, and the highest class, X flares, have a peak flux of approximately 10^{-4} W/m^2. This is known as an R4 severe storm on the NOAA Severe Weather Scale [NOAA NWS, 2007].

Table 7 summarizes definition and displays which space weather database was used to obtain the dates of severe storms. The two databases used were from the Geomagnetic Data Center in Kyoto (http://wdc.kugi.kyoto-u.ac.jp/dstdir/index.htm) and from the GOES satellites (http://www.ngdc.noaa.gov/goes/sem/getData). This definition of a severe space weather event was based on metrics from the NOAA Space Weather Prediction Center's Space Weather Alerts as well as criteria commonly used by the space weather community.

Table 7: Definition of Severe Space Weather Events used in this work.

Storm Type	**Condition**	**Data Source**
Geomagnetic Storm	Dst < -200 nT	Kyoto
Radiation Storm – SEP	10 MeV Proton Flux > 10,000 pfu	GOES
Radiation Storm – Relativistic Electrons	2 MeV Electron Flux > 10,000 pfu	GOES
Solar Storm	Solar Flares > X10	GOES

Using the definition of severe space weather event summarized in Table 1, there were twenty-four instances of severe geomagnetic storms, six instances of radiation storms from solar energetic protons, 347 instances of radiation storms from relativistic electrons, and six instances of solar storms between 1996 and 2012. The dates and associated measurements for these severe space weather events are found in Appendices A-D.

Figure 15 shows the four types of severe space weather events, defined in Table 7 between the years 1996 and 2012, Severe radiation events caused from relativistic electrons before 2003 and after 2008 are included in the plot below, but these values are not explicitly verified in the NOAA Space Weather Prediction Center. The electron data before 2003 and after 2008 for these values were gathered from GOES.

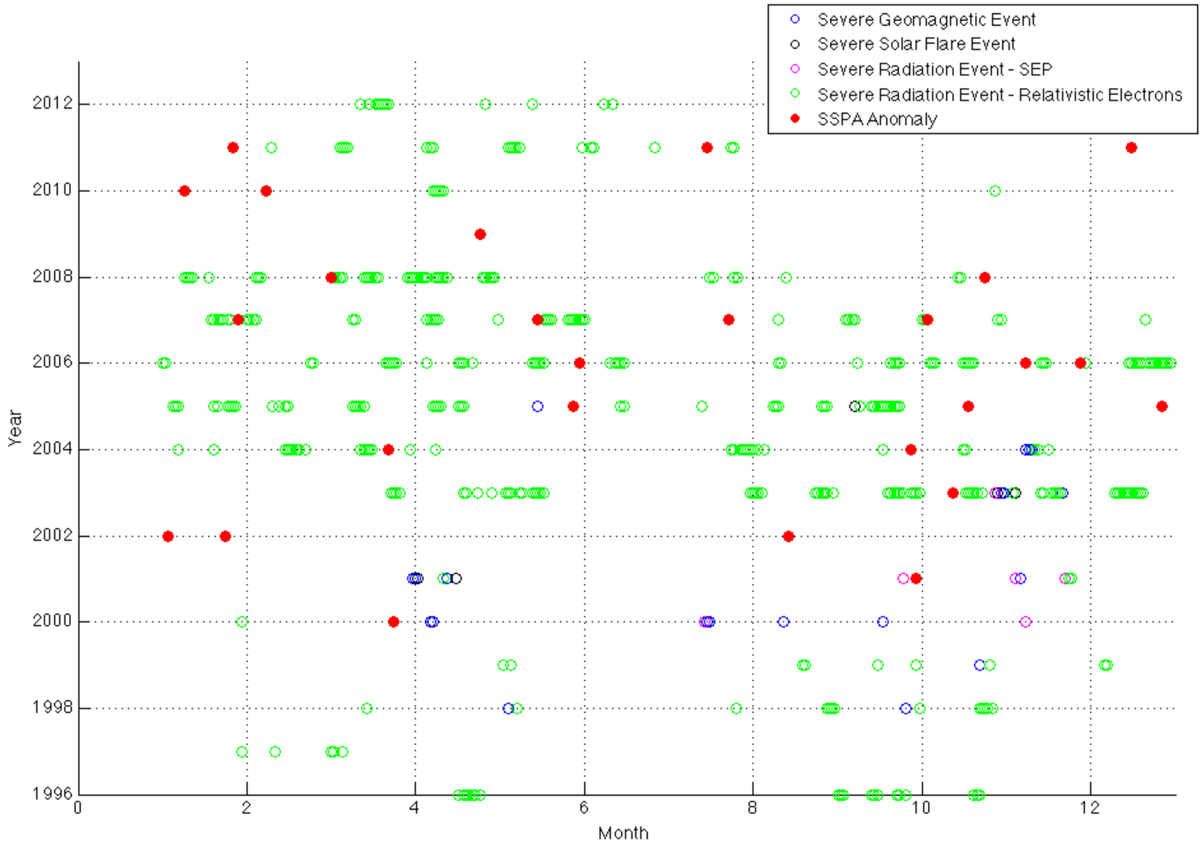

Figure 15: SSPA Anomalies and Severe Space Weather Events. Severe Space Weather events are defined in Table 7 and listed in Appendix A-D.

Table 8 displays the number of anomalies that occur before a period of two weeks, one week, three days, and one day of a severe space weather event. For both types of severe radiation events, the end of the event is recorded as the last instance the flux exceeds 10,000 pfu, to consider multiple protons flares within a single event. As expected, the number of events that occur within a given period of a severe space weather event and a particular anomaly decreases as the specified period of time decreases. This is evident for all four types of severe space weather events, but is most clear with the relativistic electron radiation events.

Table 8: Number of SSPA Anomalies that occur before the given period of time between the four types of severe space weather events

	Number of anomalies before the following periods of space weather event			
Type of Severe Space Weather Event	Two weeks before severe event	One week before severe event	Three days before severe event	One day before severe event
Radiation -	15	12	7	4

Relativistic Electron				
Radiation - Proton	0	0	0	0
Solar	0	0	0	0
Geomagnetic	0	0	0	0

Fifteen SSPA anomalies occurred two weeks before a severe radiation event. When the period of time was reduced from two weeks to one week, the number of anomalies that occurred one week before a severe radiation event reduced to twelve anomalies. Seven anomalies occurred within a period of three days before a severe radiation event, and four anomalies occurred one day before the severe space weather event. In addition, Table 9 shows the number of anomalies that occur after a period of two weeks, one week, three days, and 1 day of each space weather event.

Table 9: Number of SSPA Anomalies that occur after the given period of time between the four types of severe space weather events

	Number of anomalies after the following periods of space weather event			
Type of Severe Space Weather Event	Two weeks after severe event	One week after severe event	Three days after severe event	One day after severe event
Radiation - Relativistic Electron	15	10	7	5
Radiation - Proton	1	1	0	0
Solar	0	0	0	0
Geomagnetic	1	0	0	0

Seventeen of the twenty-six SSPA anomalies occurred two weeks after a severe space weather event. One of the seventeen occurred two weeks before a severe geomagnetic space weather event, one occurred during a severe radiation space weather event caused from SEPs, and fifteen of twenty-six SSPA anomalies occurred two weeks before a severe radiation space weather event related to relativistic electrons. Ten anomalies occurred after severe space weather events; Seven anomalies occurred three days after a space weather event, and five SSPA anomalies occurred one day after a severe space weather event.

Only one SSPA anomaly occurred within a specified period of a proton radiation event; this anomaly took place one week after a severe proton event. No anomalies occurred within any of the specified periods of a severe solar storm, and one anomaly occurred two weeks after a severe geomagnetic storm.

CHAPTER 5: SPACE WEATHER CORRELATION

The purpose of this chapter is to investigate which space weather effects are associated with SSPA anomalies. We intend for our analysis, observations, and conclusions to serve as a starting point for future interactions between the commercial satellite communications industry and space weather science communities on understanding the sensitivity of key components to the space environment. The goal is to improve both component robustness as well as improving system performance using design redundancy, operational, and predictive monitoring approaches.

Data Analysis Approach

The approach for correlating the Inmarsat telemetry and space weather data primarily focused on methods for managing numerous databases of unique time periods and increments. Once all of the data was gathered, we began removing space weather data that was at the time considered irrelevant to this particular study. For reliability measures, the original files containing the irrelevant space weather data were kept separate from the files used for the analysis.

Numerical techniques were implemented to extract elements from the space weather data that matched the time stamps of the Inmarsat telemetry, and an original period of five days before and one day after each of the SSPA anomalies was investigated. While this period of time provided interesting insight into the space weather environment at each anomaly, a series of severe space weather events at the boarder of the period suggested that expanding the period was necessary. Therefore the period of analysis broadened from five days before and one day after each anomaly to two weeks before and after the anomalies.

SSPA Anomalies and Space Weather Environment

Space weather originates from the sun[2], which emits solar flares, high-speed solar winds, and coronal mass ejections (CMEs). CMEs, or giant gas clouds, are emitted from the sun at speeds of about 1000 km/s and carry energetic particles that contribute to the formation of geomagnetic storms. Relativistic electrons can penetrate surfaces within the geostationary satellites and deposit charge into spacecraft electronics and other components. If the charge accumulates, it can discharge and cause satellite anomalies [Baker, 2002]. Due to the challenge in predicting the effect of space weather events on communications satellites, many commercial operators simply continue nominal operation during periods of increased solar activity.

One metric used to assess the overall strength and variability of solar activity, including phenomena such as solar flares and coronal mass ejections, is the sunspot number. The increase and decrease in the sunspot number defines the maximum and minimum of the solar magnetic activity cycle, a period of approximately eleven years. At solar maximum there is an increased chance of solar flares, and CMEs However, even at solar minimum, the Sun can produce damaging storms [Cole, 2003].

Figure 16 displays the raw sunspot number in blue, the smoothed sunspot number in red, and the Inmarsat SSPA anomalies from between 1996 and 2012. This period encompasses Solar Cycle 23 (May 1996 – Dec. 2008) and Solar Cycle 24 (Jan. 2009 – present). Solar minimum for Cycle 23 occurred in 1996, the maximum for Cycle 23 occurred between 1998 and 2002. The solar

---

[2] Galactic cosmic rays are the exception; these high-energy particles do not originate from the sun.

minimum for Cycle 24 occurred between 2008 and 2009, however, the solar maximum has yet to occur for Cycle 24 [Riley, 2012]. The solar cycle data for this plot are from SIDC.

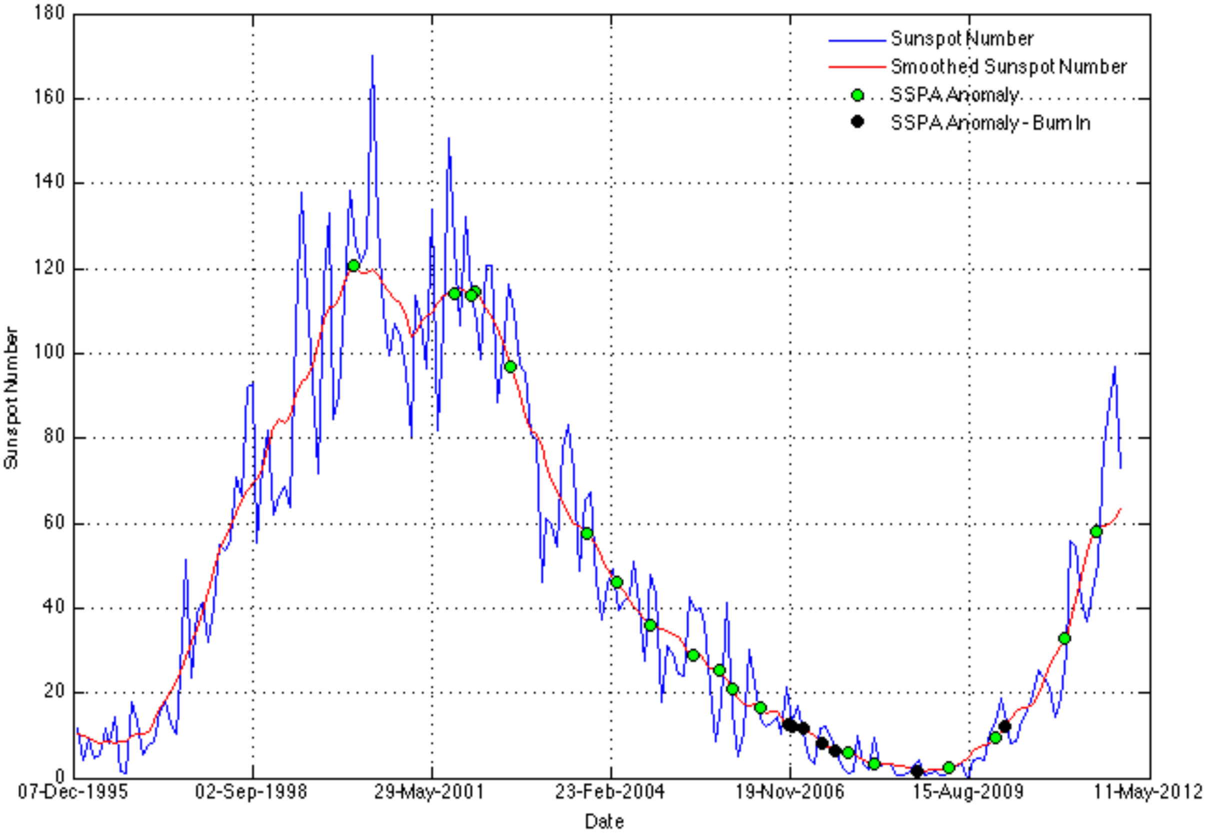

Figure 16: Sunspot number for Solar Cycle 23 and Solar Cycle 24. Raw Sunspot Number (blue), Smoothed Sunspot Number (red), Inmarsat SSPA Anomalies (green points), and the Inmarsat SSPA Anomalies that occur within the first two years after launch (black points).

At solar maximum, between 1998 and 2002, five anomalies occurred, and at solar minimum, between 2006 and 2009, ten anomalies occurred. When considering all twenty-six anomalies, it is clear that more anomalies occur during solar minimum than solar maximum. However, the twenty-six SSPA anomalies are from two separate satellite fleets with different designs and SSPA configurations. Furthermore, from 1996 to 2012, the total number of satellites overall increased from zero to eight.

In Figure 17(a,b), we depict the number of SSPA anomalies that occur annually between 1996 and 2012 (vertical bars), as well as the smoothed sunspot number (blue line), which represents the solar cycle. Figure 17(a) includes all twenty-six SSPA anomalies, and Figure 17(b) excludes the seven “early” anomalies that occur within two years of the launch date of the satellite. To help understand the role of space weather during these “early” anomalies, we examine each of these seven anomalies in more detail. There were no anomalies prior to 2000, even though this time includes launch and the intial years of operation that are commonly associated with satellite anomalies due the hazards of the launch environment and orbital repositioning.

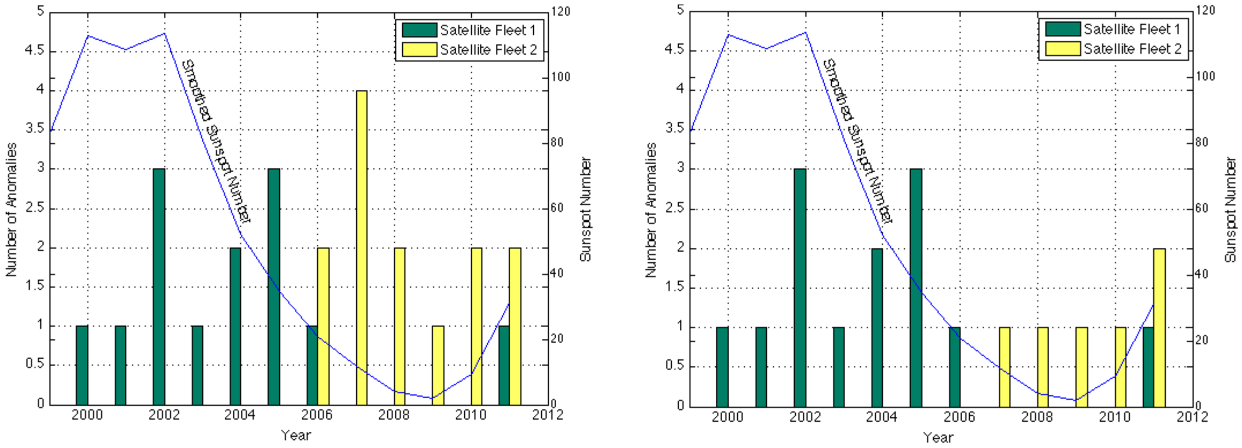

(a) (b)

Figure 17 (a,b): Yearly SSPA anomaly totals per satellite fleet (yellow and green bars), plotted with smoothed sunspot number (blue line). Figure 17(a) includes anomalies that occur within two years of launch and Figure 17(b) excludes anomalies that occur within two years of launch.

The different color bars in Figure 17 (green and yellow), represent the two separate satellite fleets. Comparing Figure 17(a) with Figure 17(b) where we have omitted the seven SSPA anomalies that occurred within two years of launch (also designated with black points in Figure 16), then the yearly rate of SSPA anomalies appears to decrease during solar minimum. At solar maximum there are still five anomalies, and at solar minimum there are four anomalies in Figure 17(b) instead of ten in Figure 17(a). In Figure 17(a), the year with the highest number of SSPA anomalies (four anomalies in 2007) coincided with solar minimum. However the next highest years (three anomalies) occurred at both solar maximum (2002) and during transition between solar maximum and solar minimum (2005).

Figure 18 displays the number of SSPA anomalies per year per satellite in Fleet A along with the solar cycle. A similar graph for Fleet B is not shown, because it has yet to experience a full solar cycle. The number of SSPA anomalies per year are divided by the number of satellites in operation per year. The purpose of this figure is to show a normalized version of Figure 16 that more clearly portrays the satellite population and corresponding anomalies on a yearly basis.

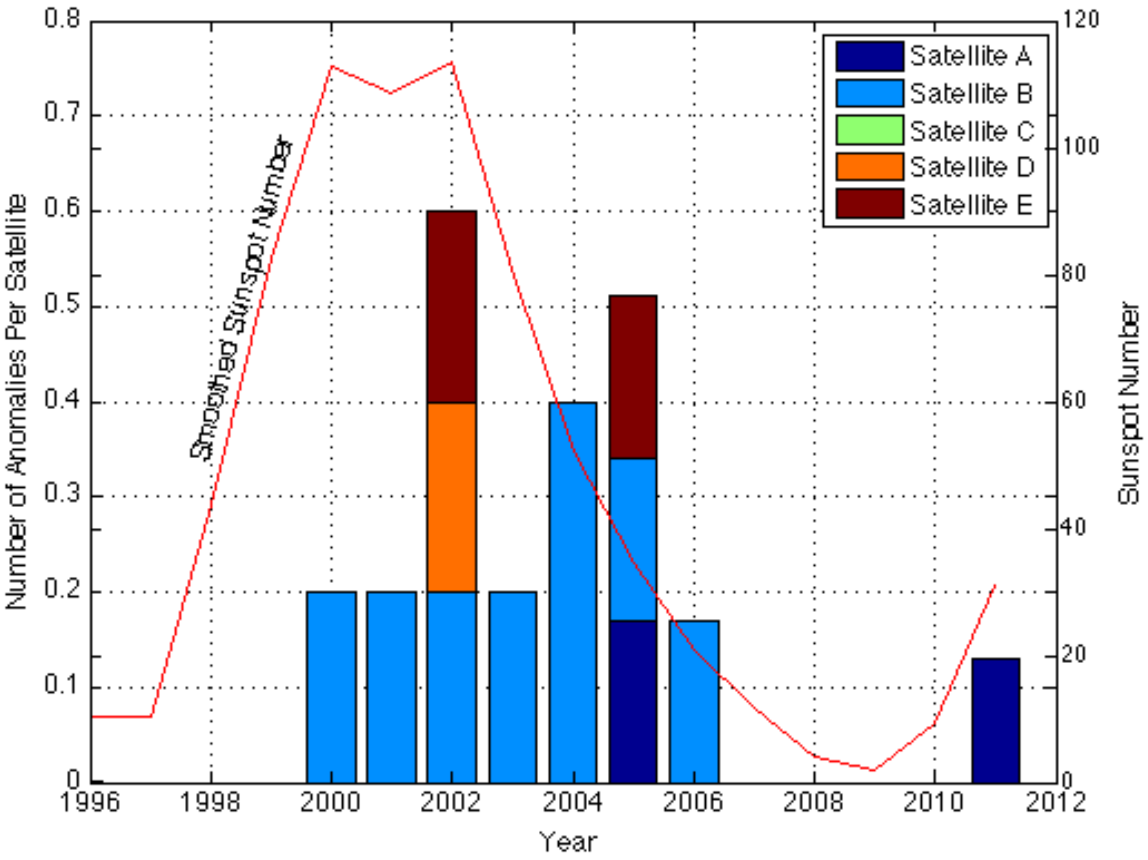

Figure 18: SSPA anomalies per year per satellite in Fleet A, from 1996 to 2012. Each letter in the legend corresponds to a different satellite in each fleet. The number of anomalies per year are divided by the number of satellites in operation, respectively. The satellite fleet has experienced an entire solar cycle, whereas the fleet B has not.

In Figure 18, the SSPA anomalies on Fleet A do not primarily occur at solar maximum, but occur during the declining phase of the solar cycle. The declining phase of the solar cycle is also when stream interaction regions (SIRs) originating from coronal holes, or high-speed solar wind streams occur. This is also when high-energy electron fluxes at GEO are at a maximum [Shea, 1998; Miyoshi, 2008]. However, additional SSPA data from geostationary communications satellites during the late 1990s would improve our understanding of the effect of space weather during this period.

Figure 19 shows the SSPA anomalies on Fleet A and the log10 of 2 MeV electron flux from the Los Alamos National Labs (LANL) Energy Spectrometer for Particles (ESP) [Reeves, 2011]. The 2 MeV differential electron flux was smoothed over a period of 62 days (about two months).

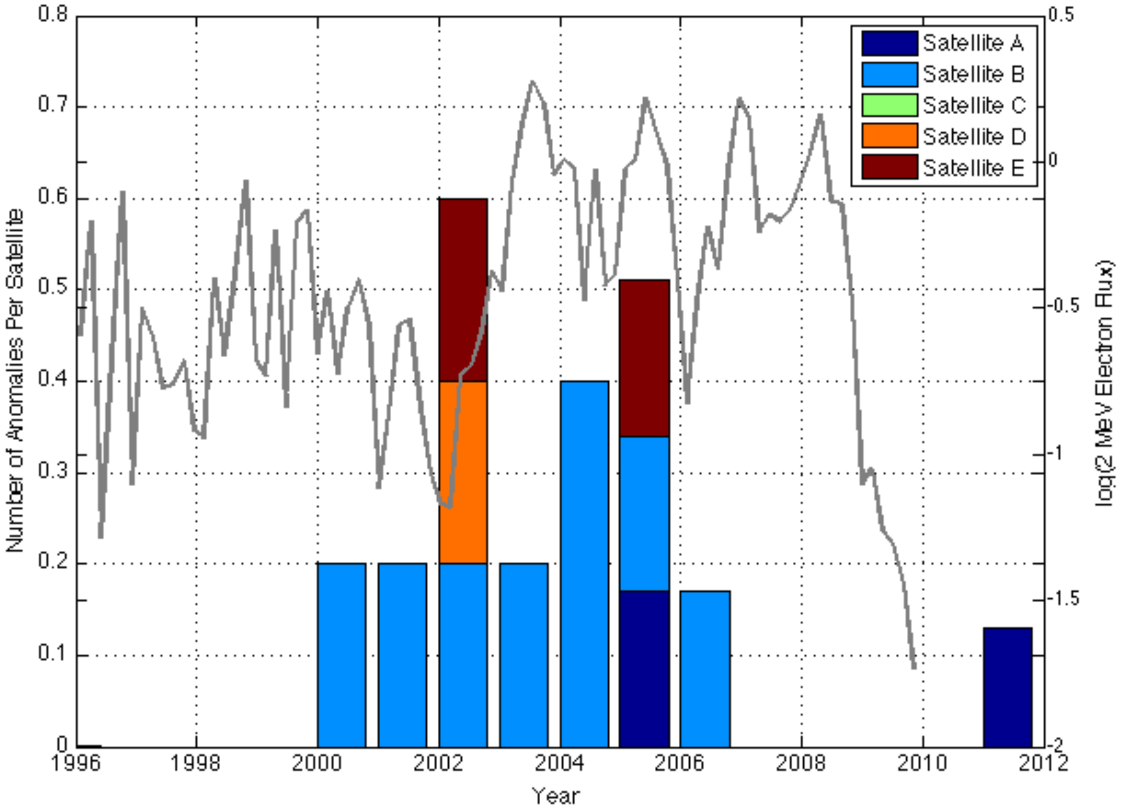

Figure 19: SSPA Anomalies per year per satellite and the LANL ESP log of 2 MeV Electron Flux. The LANL ESP measurements are from 1996-2009.

There is an increase in the 2 MeV electron flux that begins in 2002, and peaks from 2003 until 2005, which is approximately the time of the decline of the solar cycle after solar maximum. However, additional satellite telemetry data is required to further investigate this relationship.

SSPA Anomalies and Geomagnetic Environment

Similar to solar activity, geomagnetic space weather activity is also cyclical. However, unlike the solar cycle, the geomagnetic cycle does not have a clear minimum and maximum. The geomagnetic cycle generally consists of two peaks that occur about a year before and after solar maximum. Furthermore, a characterization metric, such as the sunspot number, does not exist for the geomagnetic cycle. This can make representation of the geomagnetic cycle difficult, and there are multiple approaches to plotting this cycle.

The geomagnetic cycle has the same 11-year period as the solar cycle, and there is always at least one peak in the geomagnetic cycle during the declining portion of the solar cycle. However, the geomagnetic cycle is not as easily defined as the solar cycle in terms of maximum and minimums [Allen, 2004]. For this reason, the geomagnetic cycle is less frequently used in analysis.

An alternative approach to show the geomagnetic cycle is to plot the annual number of times Dst reaches a certain value. While different values of Dst have been previously used, in this work we look at the values of and -200 nT, consistent with our definition of severe geomagnetic events (-

200 nT in Table 1). The year 1957 is the earliest verified Dst data from the World Data Center for Geomagnetism in Kyoto, Japan. This data is available from http://wdc.kugi.kyoto-u.ac.jp/dstdir/index.html.

Interestingly, the years since 2006 are the first time in recent history that there have been zero instances of severe geomagnetic storms for a period of *more* than three years. The previous three-year periods of zero severe geomagnetic storms were in 1964 and 1995. As of 2012, it has currently been six years since the last severe geomagnetic storm of Dst less than -200 nT.

Figure 20 shows the yearly number of SSPA anomalies per satellite and the geomagnetic cycle between 1996 and 2012. Similar to Figure 18, Figure 20 shows the number of anomalies per satellite per year in order to take into account the changing number of satellites with time. The number of anomalies per year are divided by the respective number of satellites in operation.

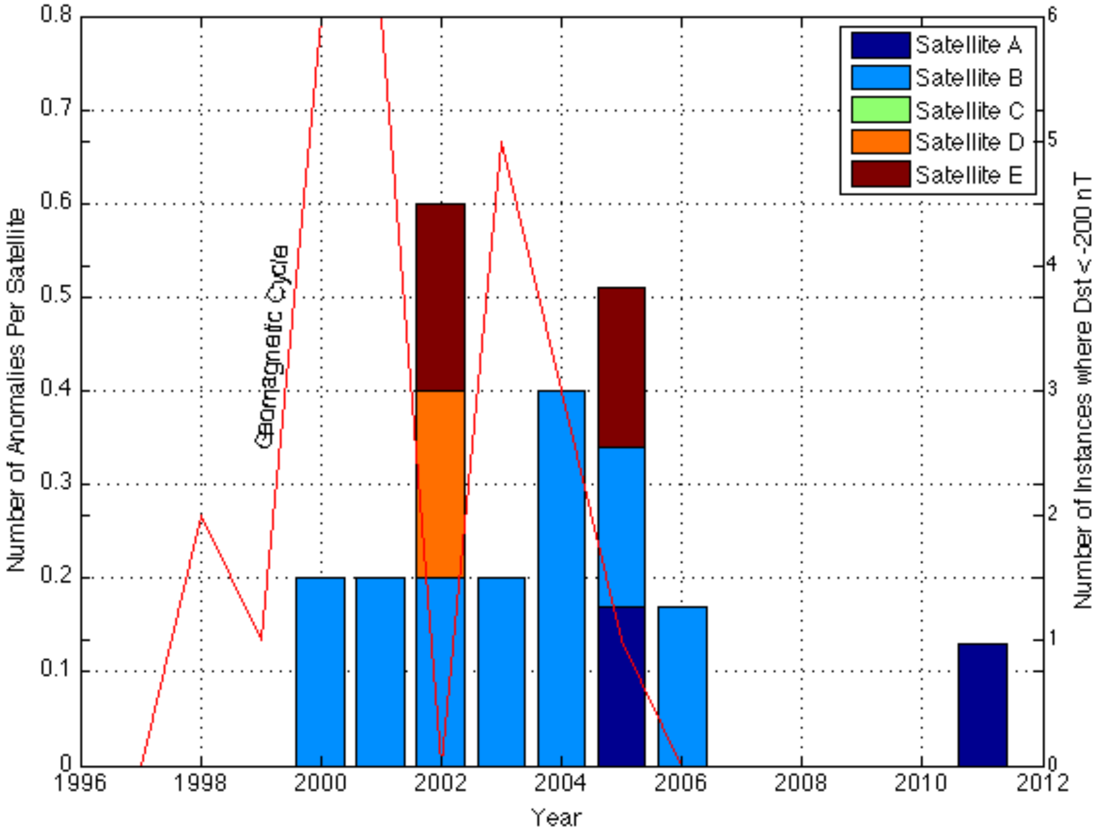

Figure 20: Fleet A SSPA anomalies per year per satellite and the geomagnetic cycle. Fleet B SSPA anomalies are not shown, as they first occurred in 2006, after which the geomagnetic cycle has remained quiet. The number of anomalies per year are divided by the number of satellites in operation, respectively. This normalization explains why the range of the ordinate is 0 to 0.8.

While there has been no severe geomagnetic activity since 2006, between 2000 and 2006 the number of SSPA anomalies appear to occur at low periods of geomagnetic activity. There appears to be a clearer relationship between geomagnetic activity and SSPA anomalies, even based only on data from 1996—2006, than a connection between yearly SSPA anomalies and the solar cycle.

Figure 21 consists of three subplots that characterize the geomagnetic space weather environment during the time of SSPA anomaly. Figure 21(a) is Kp, the general qualitative metric for the geomagnetic field, recorded from Kyoto. Figure 21(a) shows that the highest Kp value experienced at the time of the 26 SSPA anomalies is Kp = 4. With the Kp scale from 0-9, a level of Kp = 4 is not considered severe geomagnetic space weather conditions. Figure 21(b) shows the values of Dst, also gathered from Kyoto, at the time of the anomaly, and indicates that at the time of these 26 SSPA anomalies, the geomagnetic field is in a quiet condition. Dst is often referenced as the best estimate for predicting the likelihood of extreme space weather events [Riley, 2012]. The seven blue dots denote the SSPA anomalies that occurred within two years of launch, and the remaining nineteen anomalies are shown in red crosses.

Lastly, Figure 21(c) shows the ACE solar wind speed (Vx) measured in kilometers per second. When the solar wind speed is between 600—800 km/s (as shown in the upper shaded area of the plot), the magnetopause may experience compression, but this is also dependent on solar wind pressure and density. When the magnetopause is compressed, satellites located at geostationary orbit are often located outside the protection of the magnetic field and are susceptible to the harmful space weather environment.

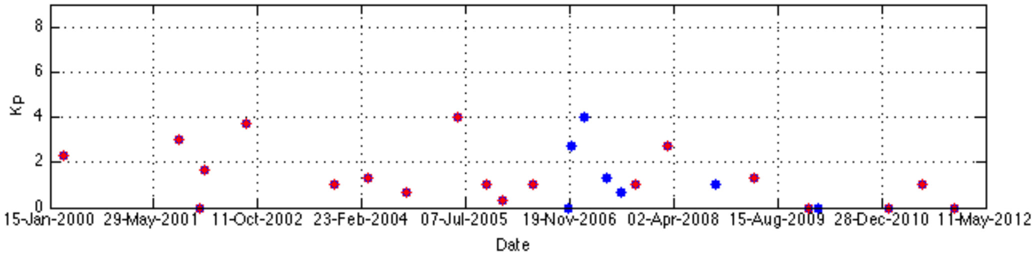

(a)

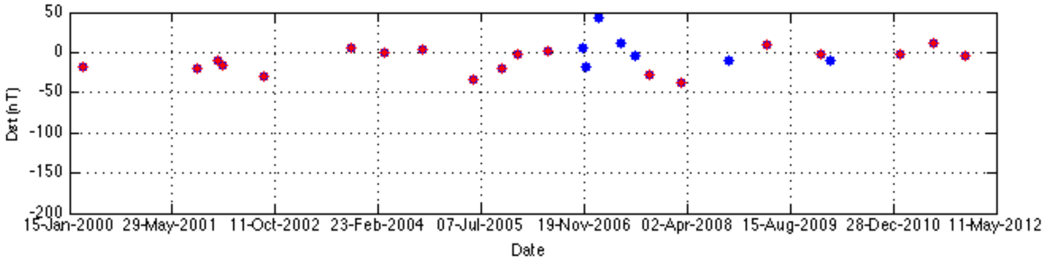

(b)

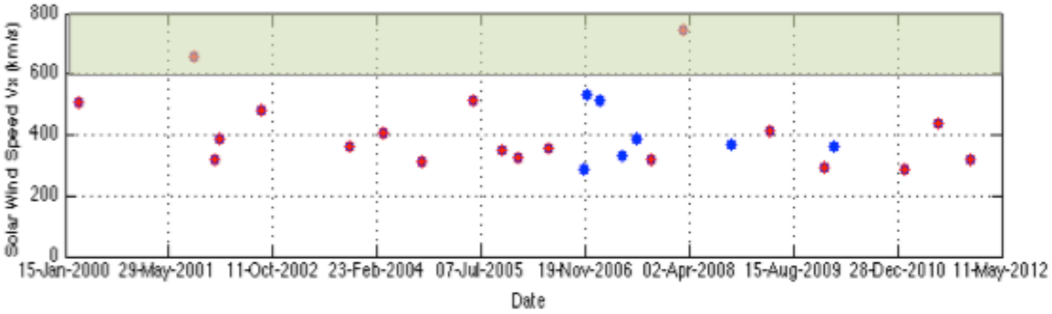

(c)

Figure 21(a-c): The Kp, Dst, and solar wind speed at the time of all 26 SSPA anomalies. Blue anomalies occurred during first two years of satellite operation and are considered to be due to the launch environment.

Of the two instances where the solar wind speed exceeded 600 km/s, one of the two SSPA anomalies occurred during one of the six most severe space radiation events caused from SEPs, and the other SSPA anomaly occurred during a severe relativistic electron radiation event. At the time of the anomaly, this SSPA experienced three times the 2 MeV electron flux (14400 pfu) compared to the anomaly with the second highest 2 MeV electron flux (4900 pfu), and experienced more than eight times higher than the SSPA anomaly with the third highest 2 MeV electron flux. Furthermore, the second highest 2 MeV electron flux (4900 pfu) occurred when the solar wind speed was 533.99 km/s, which was highest value apart from the two instances where the solar wind speed was between 600-800 km/s.

In summary, statistics of the solar wind and geomagnetic indices at the time of the twenty-six anomalies are shown in Table 10. While the maximum solar wind speed and pressure were 779.9 km/s and 3.3 nPa, respectively, the MP standoff distance, measured in earth radius (R_E) was at a minimum compressed to 11.6 R_E. As the satellites are located at geostationary orbit, or 6.6 R_E, the worst case anomaly (in terms of solar wind) was within the magnetopause by 5 R_E, and was significantly shielded from the magnetosphere.

Table 10: Geomagnetic and Solar Wind Parameters at the time of the SSPA Anomalies

	Solar Wind Speed (km/s)	**Solar Wind Pressure (nPa)**	**MP standoff (R_E)**	**Dst (nT)**	**Kp**
Mean	425.5	1.75	12.93	-10.46	1.373
Minimum	292	0.9	11.6	-43	0
Maximum	779.9	3.3	14.1	12	4
Range	487.9	2.4	2.5	55	4
Std. Dev	126.95	0.76	0.79	16.37	1.274

It is possible that more significant conditions, and specifically magnetopause compression, occurred prior to the anomalies, and thus in the future it is important to investigate the condition of these parameters up to two weeks before the SSPA anomalies.

SSPA Anomalies and Charged Particles

Relativistic electrons cause bulk charging, and can ultimately lead to circuitry burn out or major satellite anomalies. Bulk charging, or deep-dielectric charging, typically occurs hours to days after large geomagnetic storms, and are the result of high-energy electrons in Earth's Van Allen radiation belts. To quantify the high-energy electrons during the time of each SSPA anomaly, the authors obtained GOES 2 MeV electron flux data for a period of five days prior to each anomaly and one day after.

The electron flux data is taken from the GOES satellite that is longitudinally closest to the respective Inmarsat satellite. There are situations when the GOES satellite is located more than fifty degrees away from the Inmarsat satellite. Given the low time resolution of the current study, that should not be a factor in correlation of events with SSPA anomalies.

Using the 2 MeV electron flux data from the GOES SEM, we have mapped the range of electron flux rates two weeks before and after each of the twenty-six SSPA anomalies [NSWPC, 2000]. Prior to analyzing the data for a period of two weeks surrounding the anomaly we selected a period of five days prior and one day after each of the SSPA anomalies. In this analysis we found that the majority of the anomalies experience substantial, but non-severe levels of relativistic electron radiation, which suggested that the space weather phenomena at periods of up to weeks or months contribute to the satellite anomalies. Figure 22 shows the range of 2 MeV electron flux rates that each satellite experiences two-weeks before and after each anomaly.

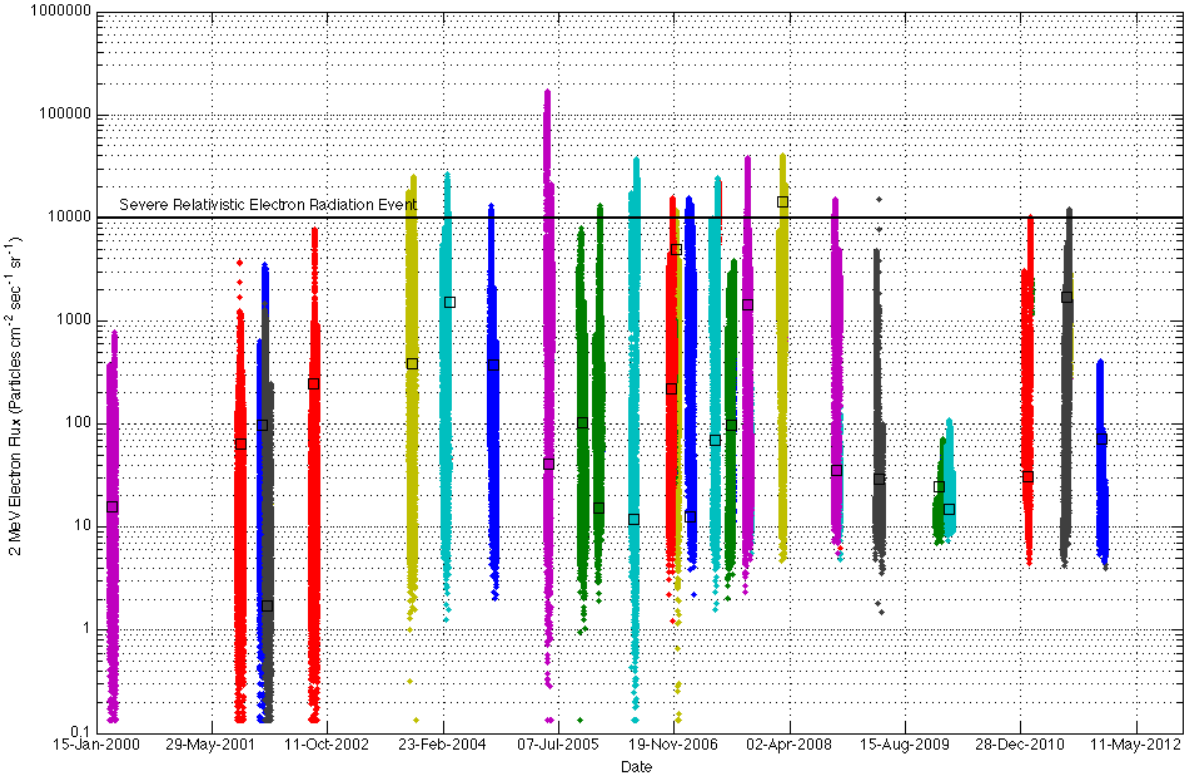

Figure 22: The 2 MeV electron flux rates two weeks before and after each of the SSPA anomalies. The 2 MeV electron flux rate at the time of each SSPA anomaly is shown by the black squares.

Sixteen of the twenty-six SSPA anomalies experienced electron flux rates consistent with severe relativistic electron radiation events. The remaining ten anomalies experienced maximum flux rates ranging between 71.3 pfu and 7940 pfu throughout the two-week period surrounding the anomaly. Of the seven "early" anomalies within two years of launch, five anomalies experience levels of severe relativistic electron radiation during two weeks before the anomaly, but at the time of the anomaly, the electron flux is relatively low.

After analyzing the 2 MeV electron flux two weeks before and after the anomaly, we compared the 2 MeV electron flux with the SSPA current. Initially we chose to investigate a period of five days before and one day after each anomaly. Figure 23 shows one example of this comparison. The 2 MeV electron flux (solid blue line) and the SSPA current (dotted green line) five days prior and one day after an SSPA anomaly; the anomaly is designated with a red line.

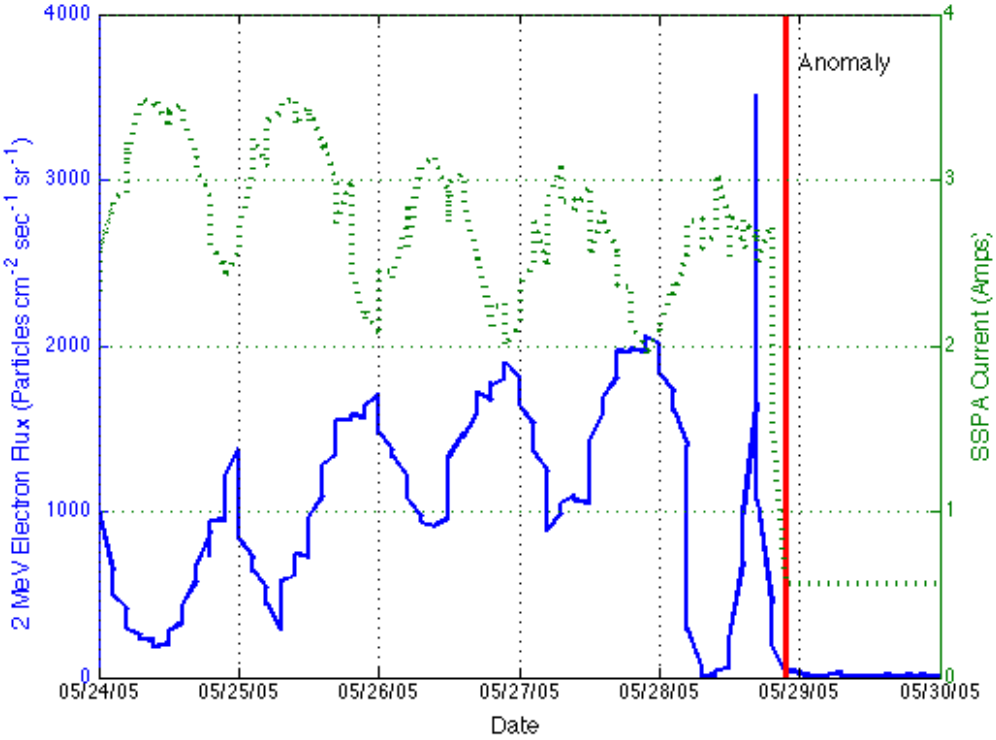

Figure 23: 2 MeV Electron Flux during SSPA Anomaly for five days prior to and one day after an anomaly plotted on the left vertical axis, and SSPA current plotted on the right axis. The GOES 2 MeV electron flux is the blue line, the SSPA current is the dotted green line, and the anomaly is marked with a red line.

The 2 MeV electron flux, shown in the blue solid line, experiences cycles of elevated electron flux until less than 12 hours prior to the anomaly, when the electron flux peaks to approximately 3500 pfu. Immediately following this peak, the SSPA experiences an anomaly. This anomaly is also observed in the SSPA current, plotted in a green dashed line. Interestingly, the SSPA current appears to mirror the trend of the 2 MeV electron flux.

While these results show a relationship between the 2 MeV electron flux and the SSPA current, we decided to expand our analysis to two weeks before and after the anomaly. In doing so found that this seemingly causal spike in 2 MeV electron flux less than 12 hours prior to the event was actually small compared to the severe spike in electrons that appears in Figure 24(a,b). Figure 24(a,b) shows the 2 MeV electron flux rate (solid blue line) and the SSPA current (dotted green line) two weeks before and after an SSPA anomaly. The anomaly is designated with a red line, and two different examples are shown in Figure 24(a) and Figure 24(b).

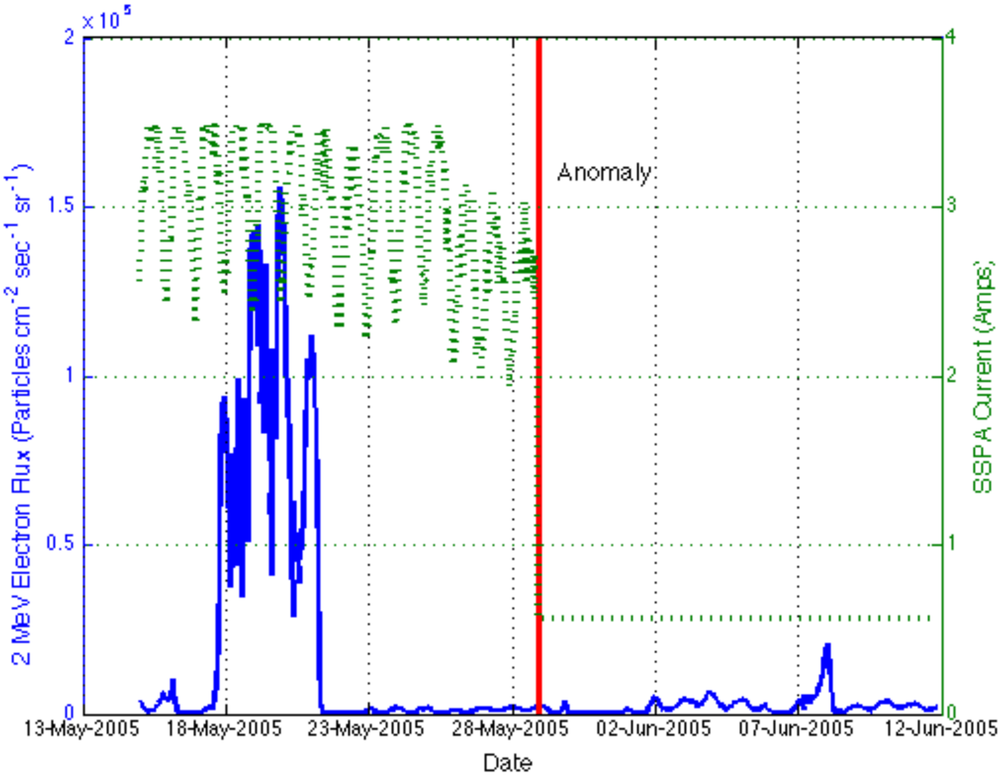

(a)

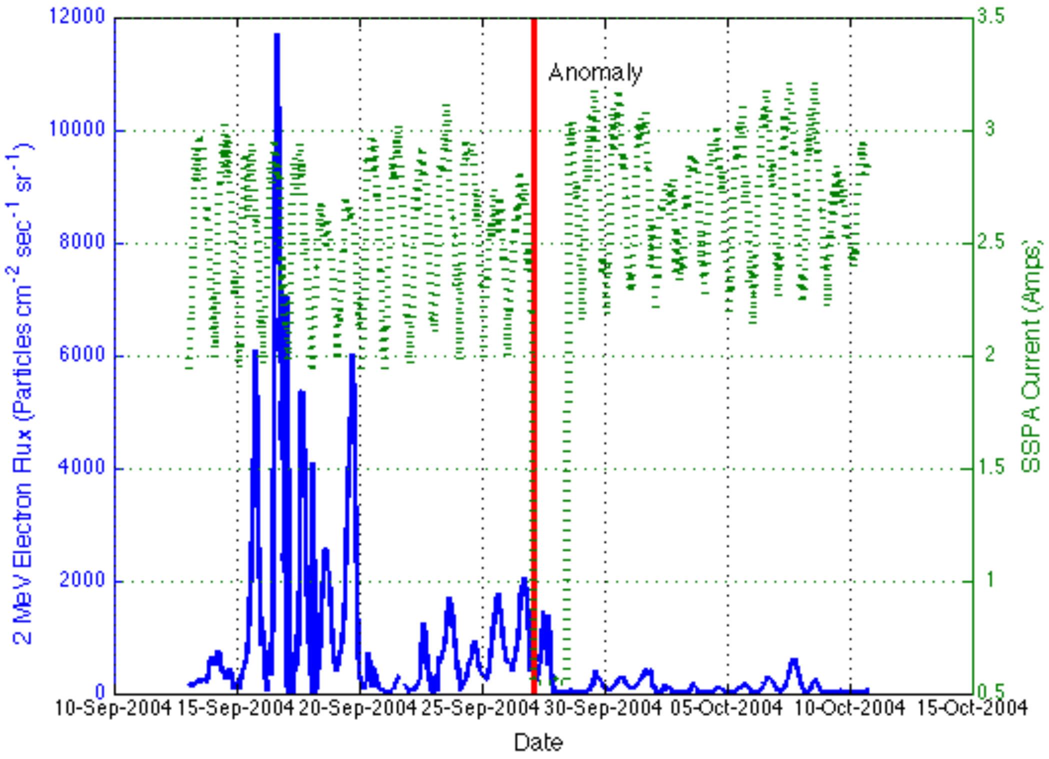

(b)

Figure 24(a,b): 2 MeV Electron Flux during SSPA Anomaly for two weeks before and after an anomaly plotted on the left vertical axis, and SSPA current plotted on the right axis. Figure 24(a) and 24(b) represent two different anomalies on two distinct satellites. The GOES 2 MeV electron flux is the blue line, the SSPA current is the dotted green line, and the anomaly is marked with a red line.

In Figure 24(a), the peak 2 MeV electron flux occurred 10.6 days before the SSPA anomaly occurred. Figure 24(b) shows another example of an SSPA anomaly. The peak 2 MeV electron flux in Figure 24(b) occurred 10.4 days before the SSPA anomaly. Of the 15 anomalies that occurred two weeks after a severe electron event, a total of six anomalies occurred 10 +/- 1.5 days after a peak of severe electron flux. This could be due to deep dielectric charging inducing surface dielectric charge buildup and discharge.

For the fifteen out of 17 relativistic electron scenarios, the peak 2 MeV electron flux occurred from 0.2 to 14 days before the SSPA anomaly, with a peak flux between 2,870 pfu and 167,000 pfu. On average, these anomalies occurred 8 days (1 sigma of 4.7 days) after severe relativistic electron fluxes. As shown in Figure 15, the time distribution of these events tends to be clustered. For the remaining eleven out of 26 anomalies, while an event was not identified in the two weeks immediately before the anomaly occurred, they did also occur during a period of turbulent space weather; therefore, it may be necessary to extend the two-week analysis period, and investigate a larger period before and after the anomaly, such as a month. Appendix H contains plots of the 2 MeV electron flux and SSPA current for all SSPA anomalies.

In addition to relativistic electrons, high-energy protons can also cause satellite anomalies. While high-energy protons are not well understood, it is believed that these particles are the main cause of hardware anomalies, SEUs and solar array degradation. However, we decided to analyze the high-energy proton flux in a similar manner as the relativistic electrons, the high-energy proton flux during each SSPA anomaly was examined using the GOES 30 MeV proton flux data five days prior and one day after each anomaly. Figure 25 shows the high-energy proton environment during one of the twenty-six SSPA anomalies. The 30 MeV proton flux is shown with a solid blue line, the SSPA current appears as dotted green, and the anomaly is marked with a vertical red line.

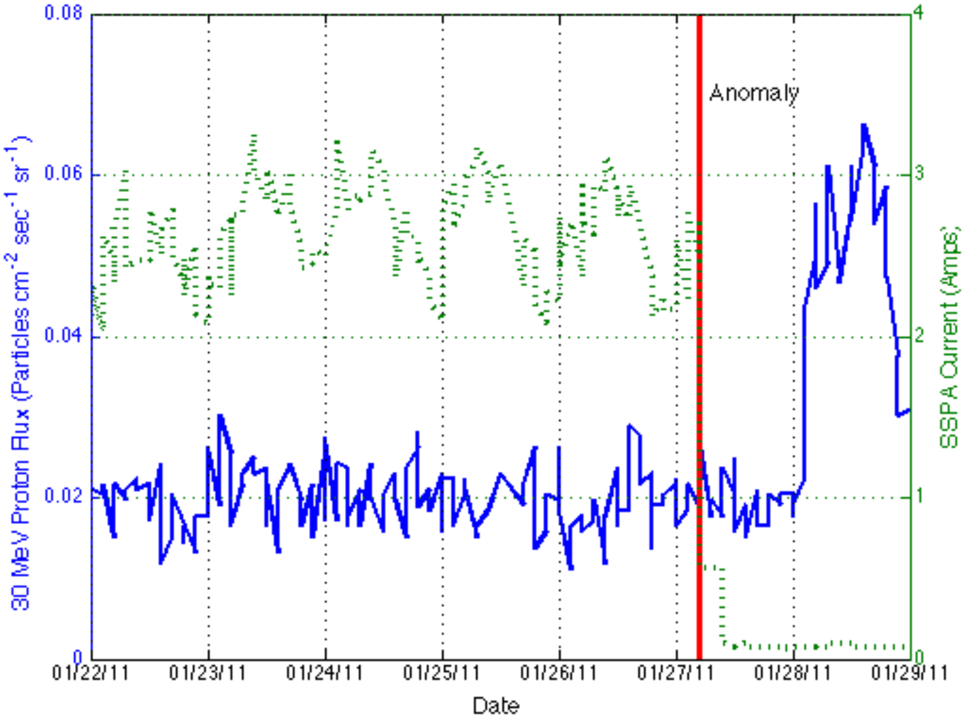

Figure 45: 30 MeV Proton Flux during SSPA Anomaly

The 30 MeV proton flux undergoes slight fluctuations before, during and shortly after the SSPA anomaly, until it experiences a significant increase one day after the anomaly occurs. Unlike the 2 MeV electron flux, the SSPA current does not mirror the proton flux. Therefore, the authors did not choose to expand the analysis for a period of two weeks before and after each anomaly.

Single Event Upsets and the Space Weather Environment

SEUs are categorized as seemingly random anomalies that occur in a satellite's electronics; for example: bit-flips, trips in power supplies, and memory changes in attitude control systems (ACS). For the two generations spanning from 1996 to 2012, there were 226 SEUs combined. Of these, fleet A experienced 28 SEUs, an average of 5.6 SEUs per satellite, and fleet B experienced 198, an average of 66 SEUs per satellite. SEUs are particularly interesting types of anomalies because they are hard to predict and, as our results show, dependent on hardware. As hardware technological capabilities grow and component form factors shrink, satellites are becoming increasingly more susceptible to radiation effects such as charging, radiation damage, and SEUs [Baker, 2000].

SEUs occur when highly energetic particles penetrate the surface and deposit charge into the electronics of a satellite [Peterson, 1996]. Protons with energies greater than 10 MeV are capable of penetrating the surface of a satellite, and can produce damage equivalent to years of normal on-orbit operation [Baker, 2000]. In severe cases, SEUs can cause satellites to lose control and tumble, potentially leading to satellite failure.

High-energy solar protons originate from coronal mass ejections. The sun emits CMEs at speeds of 1,000 km/s. These particles take only 1.5 to 2 days to reach Earth [Baker, 2000; Baker, 2002], and when the particles reach satellites at geostationary orbit they can cause SEUs and significantly contribute to solar array degradation [Lohmeyer, 2012]. The two main sources of particles that cause SEUs are solar energetic protons (SEP) and GCRs; the particles trapped within the magnetosphere do not possess sufficient energy to cause SEUs for GEO communication satellites [Wilkinson, 1991]. While it is clear that both high-energy solar protons and GCRs are capable of causing SEUs, our analysis of Inmarsat's SEU data shows that sensitivity to SEUs is also a function of different types of hardware. Although the satellite fleets under consideration here have consistent designs within a fleet, it is important to also recognize that multiple copies of a single hardware device produced from a single manufacturer have been found to vary by as much as 15% [Tylka, 1996].

Solar Proton Events

Large solar proton events (SPEs), while fairly uncommon, can cause severe radiation damage to spacecraft, because they excite protons and heavy ions to high energy levels capable of penetrating surrounding structures and shielding of satellite electronics. The energy levels required for this form of penetration are approximately 50–100 MeV/nucleon [Tylka, 1996], however particles at 10 MeV can also contribute to surface charging and SEUs [Baker, 2000].

To date, Inmarsat has not had any extended service interruptions, permanent equipment failures or suffered any reduction in satellite lifetime directly attributable to SEUs. While SEUs are challenging to predict, the Inmarsat satellites make use of automatic on-board error detection and correction functions, coupled with the use of automated ground system monitoring.

For this study, the solar proton event data comes from the NOAA Space Weather Prediction Center (http://www.swpc.noaa.gov/ftpdir/indices/SPE.txt). For each event, the proton fluxes are integrated five-minute averages recorded from GOES, which have monitored and reliably collected space environment data since 1976. The start of a proton event is defined when three consecutive proton fluxes are recorded at a rate greater than or equal to ten particle flux units (pfu), where one pfu is a rate of one particle per square centimeter of detector area per steradian of solid angle scanned per second of time. The end of a proton event is the last instance the rate is above ten pfu. This definition accounts for multiple proton flares or interplanetary shock increases within one proton event.

We compare the occurrence of solar proton events to the solar cycle. Figure 26 shows the smoothed sunspot number and the 10 MeV–10,000 MeV solar proton events between 1996 and 2012. The sunspot number is a metric used to assess the overall strength and fluctuation of solar activity, such as solar flares and CMEs. The increase and decrease in sunspot number defines the solar maximum and solar minimum. At solar maximum there is an increased chance of solar flares, coronal mass ejections and other solar phenomena. However, even at solar minimum the Sun can produce damaging storms [Cole, 2003]. The solar magnetic activity cycle has a period of approximately eleven years.

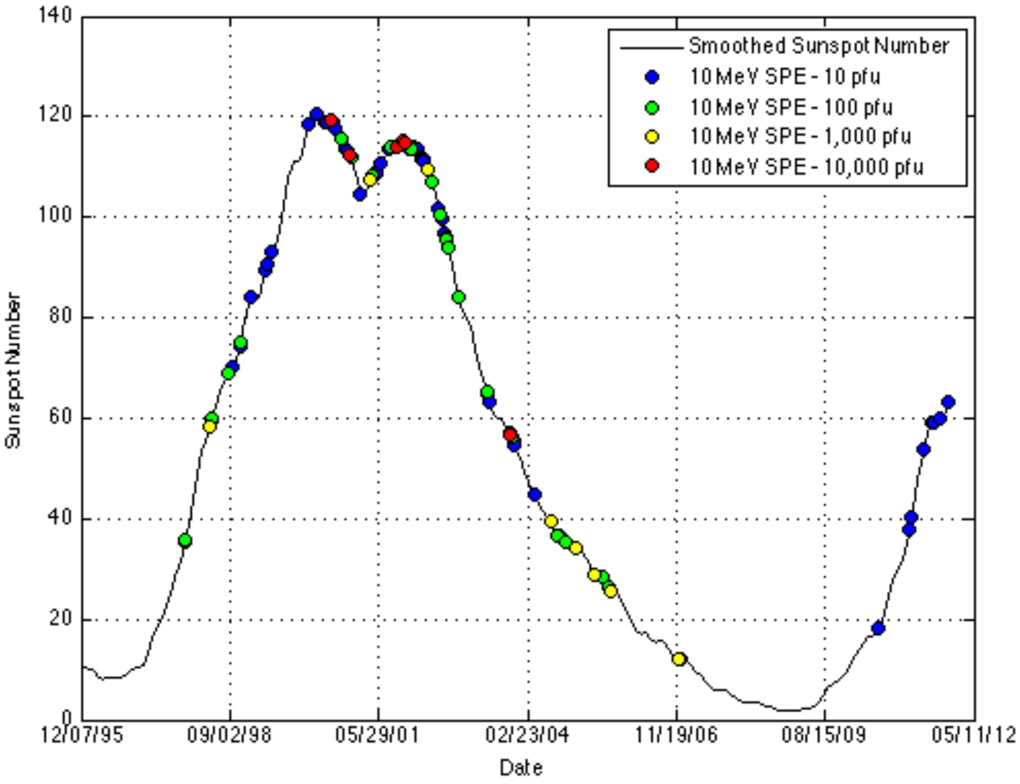

Figure 26: The distribution of 10 MeV SPEs from 10 – 10,000 pfu throughout the solar cycle and can be found in Appendix B and Appendix E-G

Solar proton events that involve 10 MeV particles with arrival rates greater than 10 pfu are considered significant events [Gopalswamy, 2006]. A list of solar proton events for particles between 10 MeV and 10,000 MeV and with rates greater than 10 pfu were recorded and can be found in Appendix B and Appendix E-G. The strongest and most frequent SPEs occur when the sunspot number is at a maximum; this is known as solar maximum, and occurs between 1998 and 2002.

In 2001 there were 22 SPEs and in 2002 there were 19 SPEs; these two years had the highest number of SPEs between 1996 and 2012. In 2001 and 2002, five of the six most severe SPEs, measuring 12,900 to 31,700 pfu occurred during solar maximum. Significantly fewer SPEs occurred at solar minimum: from 2007 to 2009 there were zero SPEs.

For a seasonal perspective, the distribution of SPEs per month is shown in Figure 27. The highest number of SPEs occurred in November with sixteen SPEs. Interestingly for SEUs instead of SPEs, the season around northern hemisphere winter solstice is the period of time with the fewest SEUs [Lohmeyer, 2012]. The months with the second highest number of SPEs were April and July, which both had twelve SPEs. For the northern hemisphere, April is just after vernal equinox, and July is just after summer solstice.

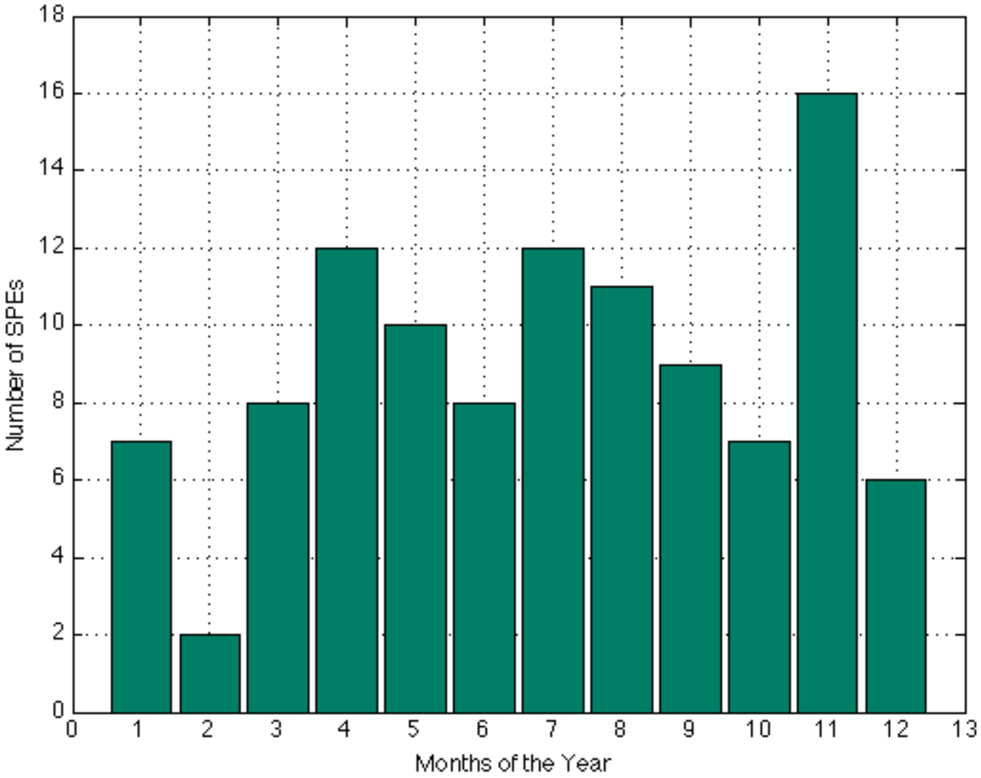

Figure 27: The number of SPEs per month measured from GOES, between 1996 and 2012. Dates of SPE events are in Appendix B and Appendix E-G

Figure 28 shows the distribution of SPEs during the Bartels cycle. The Bartels cycle, similar to the Carrington cycle, is the 27-day cycle of the Sun's rotation [Bartel, 1934]. There is no obvious trend for this distribution. The day with the highest number of SPEs occurred on the third and 26th day of the Bartels cycle, and the day with the fewest number of SPEs occurs on the 22nd day of the cycle.

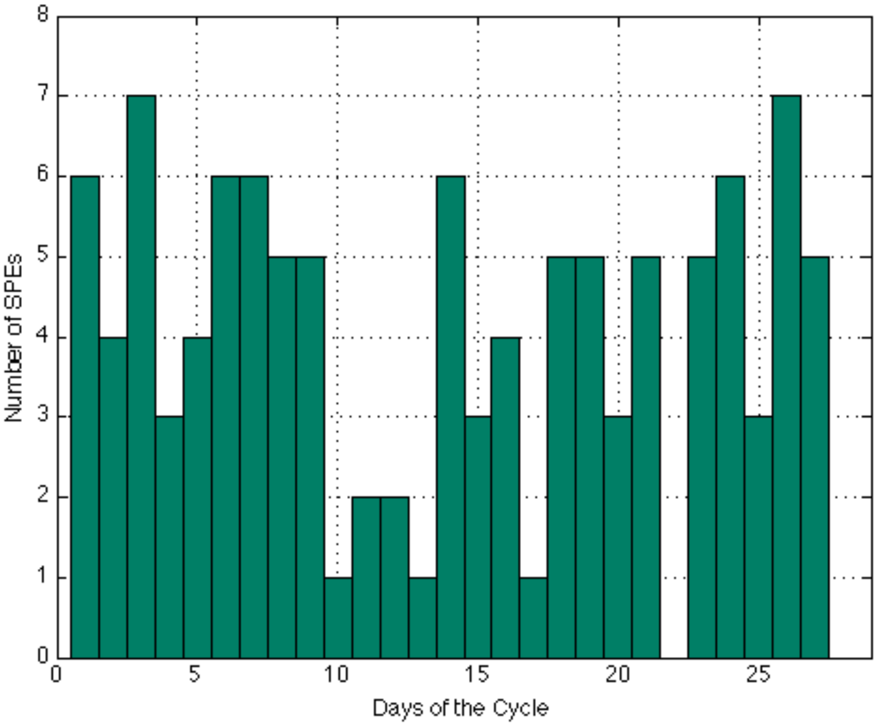

Figure 28: The number of SPEs per day of Bartels cycle measured from GOES, dates attached in Appendix B and Appendix E-G

Single Event Upsets

The causal relationship between high-energy protons and single event upsets has been studied since 1979, when two separate papers, Guenzer et al. and McNulty et al., presented evidence that high-energy protons were capable of causing SEUs [Peterson, 1996]. A follow-up study analyzed the correlation between SEUs and the space environment that occurred on the NASA's Tracking and Data Relay Satellite System (TDRS-1) from 1984 to 1990 [Wilkinson, 1991]. Similar to Inmarsat, TDRS-1 was designed to provide communications and high-data rate transmission services. Wilkinson finds that protons with energies greater than 10 MeV—40 MeV tend to induce SEUs, and that SEUs are most likely to occur when protons with energies >50 MeV exceed a rate of 10 pfu [Wilkinson, 2000]. However, Tylka et al. states that in order to do a thorough correlation analysis of SEUs, both solar protons and heavy ions must be investigated.

The composition of the solar wind is a mixture of materials found in the solar plasma, composed of ionized hydrogen (electrons and protons) with an 8% component of helium (alpha particles) and trace amounts of heavy ions and atomic nuclei: C, N, O, Ne, Mg, Si, S, and Fe that were ripped apart by heating of the Sun's outer atmosphere, the corona [Feldman, 1998]. This study only attempts to correlate solar protons to SEUs; analysis of alpha particles and heavy ions are planned in future work.

Figure 29 shows the distribution of SEUs per month. The highest number of SEUs occurs in April, followed by May.

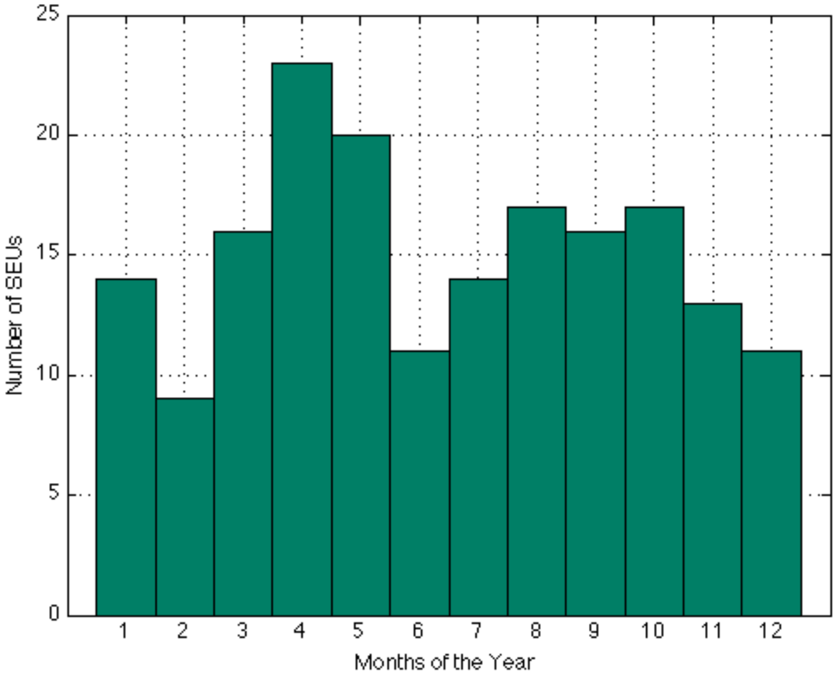

Figure 29: The number of SEUs per month measured from GOES

As shown in Figure 27, April was the month with the second highest number of SPEs, after November, which had the highest number of SPEs. For SEUs, November had the fourth lowest number of SEUs, followed by December, June, and February, which had the fewest number of SEUs. This further validates that SEUs are not likely caused from SPEs.

Figure 30 shows the distribution of SEUs during the Bartels 27-day solar cycle. Similar to Figure 28, there does not seem to be any clear and consistent trends for SEUs during the Bartels solar cycle. The day with the highest number of SEUs occurs on the 21st day of the cycle, and the day with the fewest number of SEUs occurs on the 20th day of the cycle.

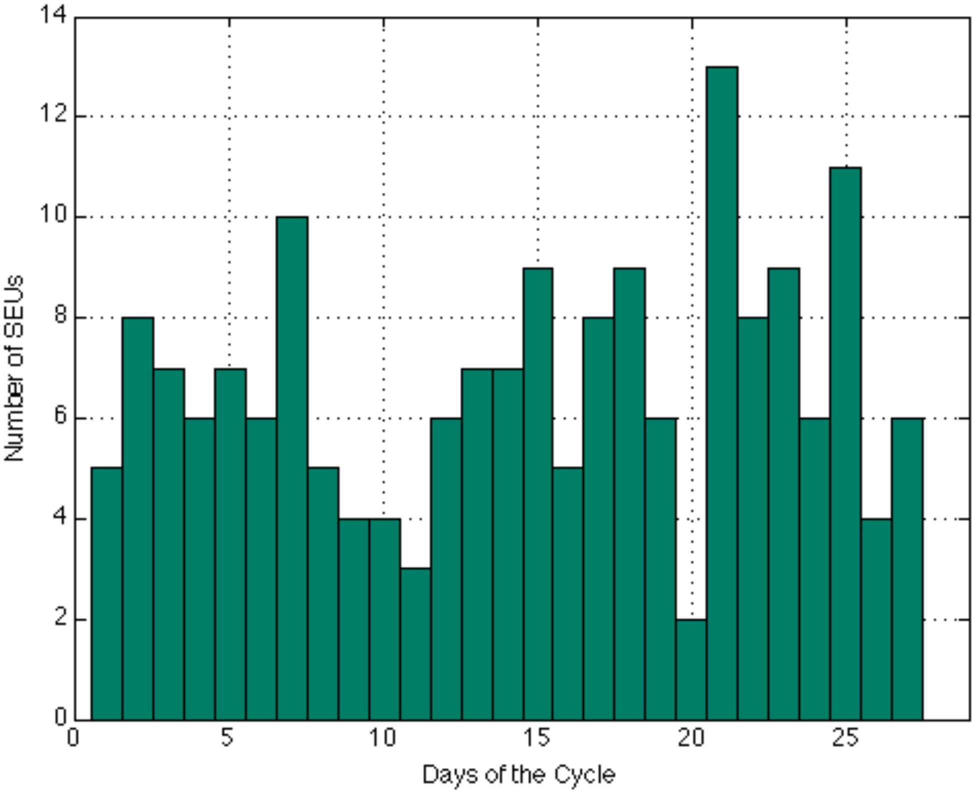

Figure 30: The number of SEUs per day of Bartels cycle measured from GOES

SEUs can occur at any time during the solar cycle, but tend to occur nearer to solar minimum, which is consistent with previous investigations [Wilkinson, 2000; Baker, 2011].

As previously discussed, Figure 26 shows that more solar proton events occur at solar maximum than at solar minimum. Figure 31 shows the SEUs that occurred on Fleet A between 1996 and 2012; the different colors represent the five different satellites in fleet A. The SEUs tend to occur most often at solar minimum. Specifically, the largest number of SEUs per year occurred in 1997, 2005 and 2009. However, between 1998 and 2000, the years leading up to solar maximum, there were also high levels of SEUs, and there were no SEUs in both 2001 near solar maximum as well as in 2008, near solar minimum.

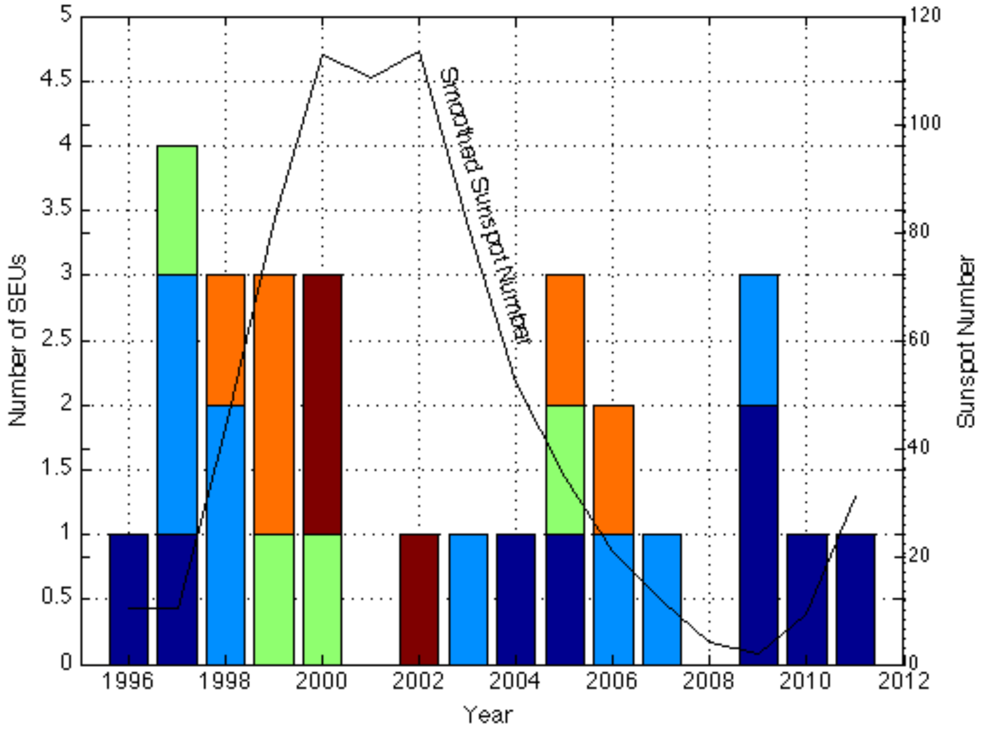

Figure 31: The solar cycle and the annual number of SEUs per satellite for satellite fleet A. The different colors represent the five different satellites in fleet A.

One possible explanation why there are zero SEUs at the 2008 solar minimum is the fact that there are only a few SEU events for satellite fleet A. Satellite fleet A only experienced 28 total SEUs, in comparison with fleet B, which experienced 198 SEUs. Figure 32 is a scatter plot of the twenty-eight SEUs that occurred on fleet A. The SEUs are shown as a black asterisk for 10 MeV solar proton events ranging from 10–10,000 pfu. There were zero SPEs between 2006 and 2010, which is approximately solar minimum.

As shown in Figure 26, a high concentration of SPEs occurs during solar maximum, or between 1998 and 2002. During this time, ten of the twenty-eight SEUs on fleet A occur. The other eighteen SEUs occur during the solar minimum of Cycle 23 and Cycle 24.

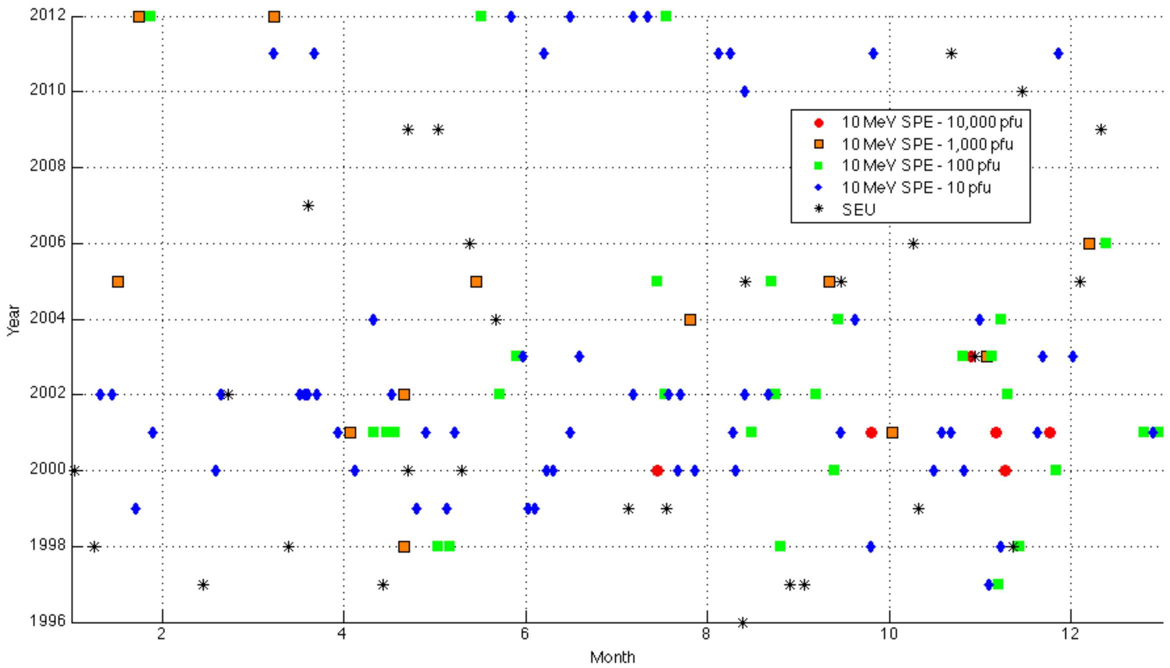

Figure 32: Fleet A SEUs plotted with 10 MeV SPEs ranging between 10 – 10,000 pfu from 1996—2012. The red circles are 10,000 pfu SPEs, the orange squares are 1,000 pfu SPES, the green squares are 100 pfu SPEs, the blue diamonds are 10 pfu SPEs and the black asterisks are SEUs. Eighteen of the twenty-eight SEUs occur at period of solar minimum, ten SEUs occur at solar maximum.

For each SEU, we analyzed the number of SPEs that occur a given period of time before and after the SEU. It is expected that the SEU would occur after the solar proton event, however we also investigate whether any severe solar proton events occur after the SEU to better understand the overall environment at the time of the SEU. Table 11 shows the SEUs on Satellite fleet A that occur one day, one week, two weeks, and one month before 10 MeV solar proton events with rates between 10-10,000 pfu.

Table 11: Fleet A SEUs that occur 1 day, 1 week, 2 weeks, and 1 month before solar proton events of 10 MeV ranging between 10 – 10,000 pfu

Solar Proton Events	**The number of SEUs that occur before an SPE on fleet A**			
	< 1 day before	**< 1 week before**	**< 2 weeks before**	**< 1 month before**
10 pfu	0	0	0	6
100 pfu	0	2	3	3
1,000 pfu	0	1	1	2
10,000 pfu	0	0	0	0

Fleet A encountered 28 SEUs, and eleven of these occurred up to one month before an SPE. Of these eleven, four SEUs occurred two weeks before an SPE and three occurred one week before an SPE. No events occurred one day before an SPE. Should a single SEU occur within one month of both a 10 MeV SPE and within one month of a later 100 MeV SPE it is counted twice, once for each of the different energy levels.

Table 12 shows the number of SEUs on fleet A that occur *after* an SPE for the same periods of time in Table 11.

Table 12: Fleet A SEUs that occur 1 day, 1 week, 2 weeks, and 1 month after solar proton events of 10 MeV protons ranging between 10 – 10,000 pfu

Solar Proton Events	**SEU occurs after the following periods of SPE on fleet A**			
	< 1 day after	**< 1 week after**	**< 2 weeks after**	**< 1 month after**
10 pfu	0	2	2	5
100 pfu	0	1	1	2
1,000 pfu	0	1	1	1
10,000 pfu	1	1	1	1

Of the 28 SEUs encountered by fleet A, nine SEUs occurred one month after a solar proton event. Out of these nine SEUs, five occurred two weeks and five occurred one week after an SPE, and one SEU occurred one day after an SPE.

The number of SEUs that occurred within the specified periods of an SPE does not necessarily suggest that a significant relationship exists between the occurrence of an SEU and SPEs. While coronal mass ejections take approximately 1.5—2 days to reach Earth, the amount of time between interactions of energetic particles with components that may eventually lead to a SEU is not well understood. The data shown here look at these statistics to get a sense for the general occurrence rates.

Figure 33 shows the smoothed sunspot number and the annual number of SEUs for satellite fleet B. Fleet B experienced 198 SEUs between 1996 and 2012. The first SEU occurred in 2005, at a period near solar maximum.

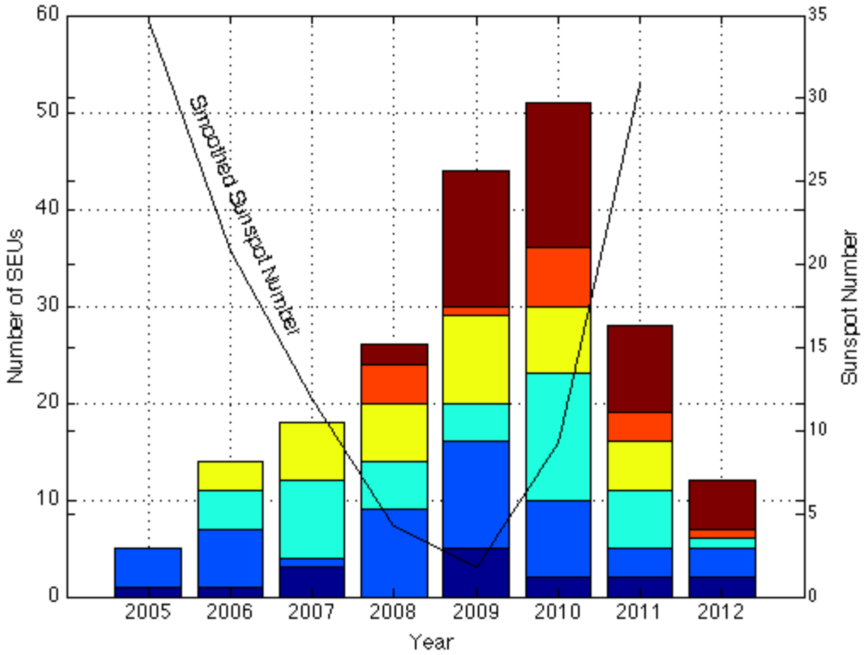

Figure 33: The solar cycle and the annual number of SEUs per satellite for satellite fleet B. The six different colors represent the local and remote computers on each of the three satellites in fleet B. An inverse correlation exists between the solar cycle and SEUs.

For fleet B, it is clear that more SEUs occur during solar minimum, compared with solar maximum. This inverse relationship strongly suggests that the single event upsets were not primarily caused by solar energetic protons, as we have shown in Figure 26 that more solar proton events occur at solar maximum. Thus, a more likely source of these SEUs could be GCRs, which primarily occur at solar minimum [Baker, 2000].

Figure 34 is a scatter plot of the SEUs, shown with a black asterisk, and the 10 MeV SPE between 10 – 10,000 pfu for fleet B.

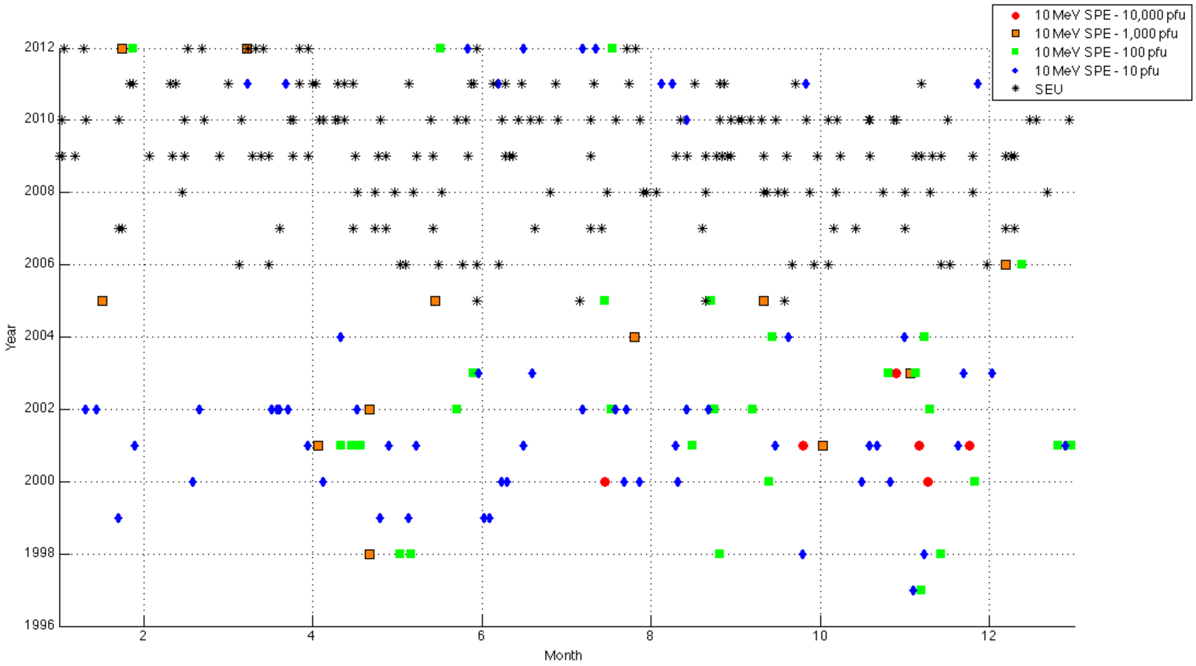

Figure 34: Fleet B SEUs plotted with 10 MeV protons ranging from 10 – 10,000 pfu from 1996—2012. The red circles are 10,000 pfu SPEs, the orange squares are 1,000 pfu SPES, the green squares are 100 pfu SPEs, the blue diamonds are 10 pfu SPEs and the black asterisks are SEUs. A clear inverse correlation exists between the occurrence of SEUs and SPEs, as only 33 of the 198 SEUs occurred one month before an SPE

The highest concentration of SEUs for fleet B occurs between 2006 and 2012, and coincides with more than four years of zero severe SPE activity. The years 2006 to 2012 also span across solar minimum.

Table 13 shows the SEUs on Satellite fleet B that occur one day, one week, two weeks, one month before solar proton events ranging from 10 MeV solar proton events ranging from 10 – 10,000 pfu.

Table 13: Fleet B SEUs that occur 1 day, 1 week, 2 weeks, and 1 month before solar proton events of 10 MeV protons of 10 – 10,000 pfu

Solar Proton Events	**SEU occurs before the following periods of SPE on fleet B**			
	< 1 day before	**< 1 week before**	**< 2 weeks before**	**< 1 month before**
10 pfu	0	4	7	19
100 pfu	0	1	3	6
1,000 pfu	0	1	2	8
10,000 pfu	0	0	0	0

Of the 198 SEUs that occurred on fleet B, 33 occurred one month before an SPE. Twelve of the 33 SEUs occurred two weeks before an SPE, and six occurred one week before an SPE. Zero SEUs occurred one day before an SPE.

Table 14 shows the number of SEUs on fleet B that occur *after* the same periods of time in Table 13.

Table 14: Fleet B SEUs that occur 1 day, 1 week, 2 weeks, and 1 month after solar proton events of 10 MeV protons ranging from 10 – 10,000 pfu

Solar Proton Events	**SEU occurs after the following periods of SPE on fleet B**			
	< 1 day after	**< 1 week after**	**< 2 weeks after**	**< 1 month after**
10 pfu	0	3	13	37
100 pfu	1	2	4	9
1,000 pfu	1	6	6	12
10,000 pfu	0	0	0	0

Out of the total 198 SEUs, fifty-four SEUs occurred within one month of an SPE. Twenty-three of the fifty-four occur two weeks after an SPE, eleven SEUs occurred one week after an SPE, and two SEUs occurred one day after an SPE.

Figure 35 shows the age of the satellite at the time of the SEU from 1996 to 2012. There are eight total satellites but the eleven different colors portray the five satellites of fleet A and separately track the local and remote computers on the three satellites of fleet B. Throughout this time the total number of satellites increases from one to eight and therefore the age of the satellites in 2012 ranges from five to fifteen years old. Aside from an overall bifurcation between fleet A and fleet B, and the influence of the 11-year solar cycle, there does not appear to be an obvious correlation between SEUs and the age of the satellite. It has been suggested that satellite anomalies are more prevalent in the first two years of operation due to “burn-in” and transients from the launch and orbital positioning activities. However, this does not appear to be a substantial contributor to the SEUs on these two satellite fleets.

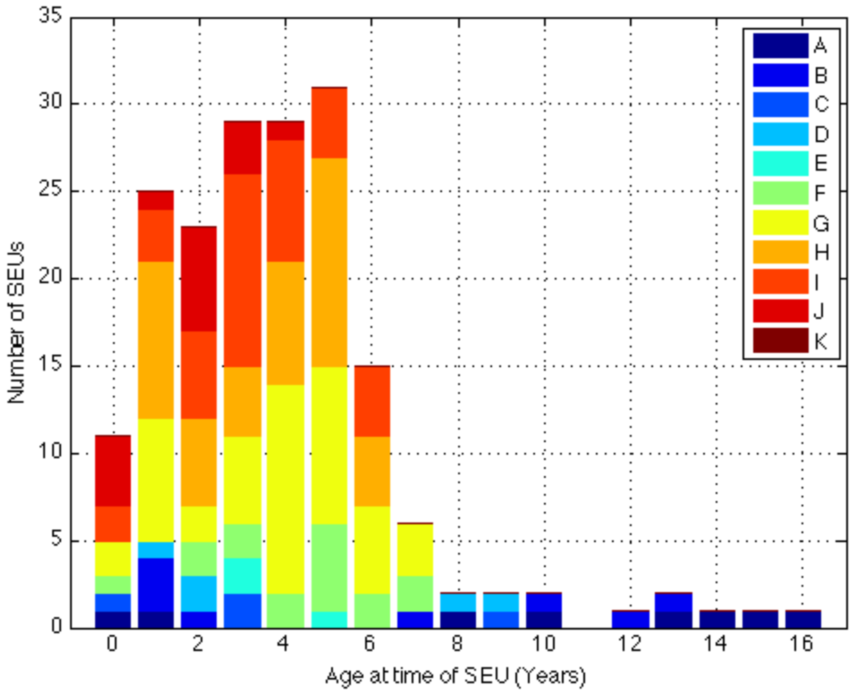

Figure 35: The age (years) of the five satellites in fleet A and the three satellites in fleet B at the time of the SEU. For satellite B the SEUs on the local and remote computers are plotted separately, which creates 11 separate devices, rather than eight.

CHAPTER 6: CONCLUSION

In analyzing the correlation between anomalies on eight of Inmarsat GEO communication satellites and space weather phenomena, the authors synthesized Inmarsat's historic archives, amounting to more than 500 MB of data (SSPA telemetry, eclipse durations and anomaly/SEUs), and space weather databases (GOES, ACE, Kyoto and SIDC).

Since 1996, Inmarsat has experienced twenty-six SSPA anomalies on eight of their satellites. These anomalies occurred anytime between less than a year and fifteen years after launch, however most anomalies occurred during years 1, 2, 3, 5, and 8 of operation. While anomalies within the first two years of operation may result from the hazardous launch environment, it is important to consider the space weather environment as a source of SSPA anomaly within the first two years of operation as well. Out of seven of the anomalies that occurred during the first two years after launch, six occurred within two weeks of a severe radiation space weather event caused from relativistic electrons.

Preliminary analysis of SSPA current periodicities helps to provide context on the dynamic traffic handled by the SSPAs. Further work is needed to determine the utility of this metric.

No correlation exists between the eclipse seasons and SSPA anomalies or SEUs. This may be due to the additional measures the spacecraft operators take to prepare the satellites for operation during eclipse seasons.

Nine of the 26 SSPA anomalies, or 35%, occur between local midnight and 06:00. More anomalies occur during these six hours than each of the other three six-hour periods. Seven of the 26 SSPA anomalies occur between 06:00 and noon, seven occur between noon and 18:00, and four of the 26 SSPA anomalies occur between 18:00 and local midnight, not including local midnight. We do not yet have enough statistics to infer the LT dependence of anomalies. The frequency of occurrence is only slightly higher at midnight, which indicates that all of these anomalies cannot be explained by the surface charging and other space weather and non-space weather effects play a role.

The majority of the SSPA anomalies occur between November and January, in northern winter solstice. February through April, northern vernal equinox, is the period with the fewest number of SSPA anomalies.

We analyze the twenty-six SSPA anomalies experienced by Inmarsat satellites between 1996 and 2000. The SSPA anomalies occurred between the launch and fifteen years of operation. Based on the Inmarsat SSPA data alone, we cannot generalize that all geostationary communications satellite anomalies have a causal relationship with the sunspot cycle (11-year solar cycle). However, it is clear that in this analysis, more SSPA anomalies occur during the declining phase of the solar cycle, when relativistic electron fluxes reach their highest values. From this analysis, it appears that SSPA anomalies on Fleet A are more likely to be caused by relativistic electrons than GCRs, which would occur more frequently at solar minimum. Additional geostationary communications satellite SSPA anomaly data would help to resolve this question. Other complications may arise from the fact that other factors such as the date from the launch, age of the satellite, time the SSPA started being operational, and type of satellite may play a role.

We defined severe space weather events, and analyzed the number of SSPA anomalies that occur within 2 weeks, 1 week, 3 days, and 1 day after a severe space weather event. A severe space weather event is classified as any one of the following four instances: (1) a severe geomagnetic storm occurs when the Dst is less than -200 (nT), (2) a severe radiation storm from SEPs occurs when the 10 MeV Proton Flux exceeds 10,000 pfu (particle flux unit: particles/sr/cm^2/s). Similarly, (3) a severe radiation storm from relativistic electrons occurs when the 2 MeV electron flux exceeds 10,000 pfu, and lastly, (4) a severe solar storm occurs when solar flares are classified as greater than X10.

There were many instances where SSPA anomalies occurred within two weeks before and after severe radiation events from relativistic electrons. Fifteen of the twenty-six SSPA anomalies occurred two weeks before or after a severe electron event. Eleven occurred within one week after, and twelve occurred within one week before a severe electron event. Seven of the twenty-six SSPA anomalies took place within three days before or after a severe electron event. Five anomalies took place within one day after, whereas four anomalies occurred within one day before a severe radiation event from relativistic electrons.

The geomagnetic cycle, as measured by Dst or Kp indices, is an eleven-year cycle that is less clear than the 11-year solar cycle because it does not have an obvious maximum and minimum, but rather multiple maxima and minima. The geomagnetic cycle is not typically discussed, however we considered it here as it may be relevant to understanding the relationship between ring current and surface charging for (equatorial) geostationary communication satellite anomalies. The number of SSPA anomalies appears to occur at low levels of geomagnetic activity. However, this conclusion is based on both limited SSPA anomalies and limited geomagnetic activity, since geomagnetic events occurred only from 1996—2006. This is because we have experienced extremely quiet geomagnetic activity for six consecutive years since 2006.

Two of the SSPA anomalies occur when the solar wind speed is greater than 600 km/s, which suggests that there may have been magnetospheric compression and that the satellites were located outside of the shield of the magnetosphere. Yet, upon further analysis of the solar wind pressure and magnetopause standoff distance for these two anomalies, the magnetopause was not compressed. Additionally, at the time of the anomalies the global geomagnetic indices, Kp and Dst, were relatively quiet with values of 0 to 4 and -50 to 50 nT respectively. In the future we will analyze the geomagnetic indices for larger periods before the anomaly to determine if any correlations exist.

We analyzed the 2 MeV electron flux rates from GOES for a period of two weeks before each of the twenty-six anomalies. Of the fifteen anomalies that occurred within two weeks after a severe electron event, a total of six SSPA anomalies occurred 10 +/- 1.5 days after a peak in severe electron flux. For these fifteen anomalies, the peak 2 MeV electron flux occurred from 0.2 to 14 days before the SSPA anomaly, with a peak flux between 2,870 pfu and 167,000 pfu. On average, these anomalies occurred 8 days (1 sigma of 4.7 days) after severe relativistic electron fluxes. The remaining eleven SSPA anomalies occurred during stormy space weather conditions, but do not have a clear association with an event within two weeks before the anomaly. In future work, we will extend the range to a month in future work to look for additional causes as well as investigate in more detail possible mechanisms for these failures.

Additional SSPA anomaly data as well as additional space weather observations will improve our understanding of the correlation between spacecraft anomalies and the space weather environment. In the future we plan to further investigate other space weather hazards.

Inmarsat has maintained nominal system operations through more than 226 single event upsets on two of its satellite fleets since 1996. Satellite fleet A experienced 28 SEUs, and satellite fleet B experienced 198 SEUs. The occurrence of these SEUs was compared to the occurrence of solar proton events. Ten MeV SPEs with rates greater than 10 pfu are considered significant and were used in this comparison.

At solar maximum we show there are fewer SEUs than at solar minimum, which is when the largest number of SEUs occur. Therefore, SEUs on the Inmarsat fleet were not found to correlate to solar proton events.

For fleet A, eleven of the total twenty-eight SEUs occurred one month *before* an SPE. Of these eleven, four SEUs occurred two weeks before an SPE and three occurred one week before an SPE. No events occurred one day before an SPE. Nine SEUs occurred one month *after* an SPE. Five of these occurred two weeks after an SPE, five occurred on week after an SPE, and one occurred one day after an SPE. Although fleet A only experienced a total of 28 SEUs or 5.6 SEUs per satellite, from fleet A we conclude that SEUs do not appear to have a direct correlation with energetic proton events.

Adding to our analysis the data from fleet B, which had 198 SEUs, an average of 66 per satellite, we find a clear inverse relationship between SEUs and SPEs. This finding suggests that solar energetic protons did not primarily cause the SEUs. Thirty-three of the 198 SEUs occurred one month before an SPE. Twelve of the 33 SEUs occurred two weeks before an SPE, and six occurred one week before an SPE. Zero SEUs occurred one day before an SPE. Fifty-four SEUs occurred within one month *after* an SPE. Twenty-three of these occurred two weeks after an SPE, eleven occurred one week after an SPE, and two SEUs occurred one day after an SPE.

We also note that there is not a clear correlation between SEUs and the age of the satellite.

The next step in this work is to investigate the correlation between SEUs and GCRs as a function of the 11-year solar cycle, as well as to consider correlations between SEUs and heavier elements. Further, the results appear to show a notable difference in the susceptibility of fleet A and fleet B to SEUs on a per-satellite basis. Closer analysis and attention paid to the particular subsystems and components most susceptible to SEUs would be valuable in explaining this difference and providing information about what mitigation methods can be employed, and information about which materials are susceptible to which types and energies of particles.

Ultimately, this research clarifies terminology used to discuss severe space weather and provides a more clear characterization of the space environment at the time of SSPA anomalies and SEUs. These two types of anomalies are strongly related to space weather events, specifically SSPA anomalies and high-energy electron flux, as well as satellite bus manufacturer and hardware. However future work remains to be completed.

A better understanding of the satellite design and the primary differences amongst satellite manufacturers would reduce discrepancies in correlation analysis, and provide insight into potential comparisons amongst like hardware from unique bus designs.

One of the major challenges with this work is conducting statistical analysis that accurately portrays the relationship between the spacecraft telemetry and space weather environment. This is particularly difficult because the space weather environment, like seismic activity, is continuously active. Therefore, determining whether the correlations between the two entities are truly significant along with a method that accounts for the continuous noise in space must be incorporated in the future.

Additional investigation of SEUs and galactic cosmic rays will be explored, as well as the analysis of the Inmarsat solar panel and total bus power data. Additionally, an increased population satellite anomaly data would help improve the analysis as well. For the space weather community as a whole, it has be suggested that a more thorough anomaly database, which contains at minimum, the subject vehicle, the date and time of the event, the 3-D location of the vehicle at the time of the event, the 3-D velocity or orbital elements for the vehicle at the time of the event, the affected subsystems, the suspected type of anomaly and level of confidence in that assessment would greatly increases the accuracy and reliability of current and future analysis and increase the accuracy of predictive models and satellite operator tools [Mazur, 2012].

APPENDIX

Appendix A. Severe Geomagnetic Event Dates (Dst < - 200 nT)

Date	Year	Level (nT)
4-May	1998	-205
25-Sep	1998	-207
22-Oct	1999	-237
6-Apr	2000	-287
7-Apr	2000	-288
15-Jul	2000	-289
16-Jul	2000	-301
12-Aug	2000	-235
17-Sep	2000	-201
31-Mar	2001	-387
1-Apr	2001	-228
11-Apr	2001	-271
12-Apr	2001	-236
6-Nov	2001	-292
24-Nov	2001	-221
29-Oct	2003	-350
30-Oct	2003	-383
31-Oct	2003	-307
20-Nov	2003	-422
21-Nov	2003	-309
8-Nov	2004	-368
9-Nov	2004	-214
10-Nov	2004	-263
15-May	2005	-247

Appendix B. Severe SEP Radiation Event Dates (10 MeV Proton Flux > 10,000 pfu)

Date	Year	Proton Flux (pfu)
14-Jul	2000	24000
8-Nov	2000	14800
24-Sep	2001	12900
4-Nov	2001	31700
22-Nov	2001	18900
28-Oct	2003	29500

Appendix C. Severe Relativistic Electron Radiation Event Dates (2 MeV Proton Flux > 10,000 pfu)

Date	Time	Flux (pfu)
3/25/03	5:00	12500
3/26/03	5:00	14700
4/18/03	11:25	17900
4/19/03	10:50	12100
4/23/03	17:15	16800
4/28/03	9:40	14600
5/3/03	9:00	16300
5/4/03	9:00	22900
5/5/03	9:00	22400
5/8/03	9:00	21600
5/9/03	9:20	47300
5/13/03	9:20	11100
5/14/03	9:15	14100
5/15/03	9:00	30400
5/16/03	5:00	33000
5/17/03	5:00	11300
7/31/03	9:45	19400
8/1/03	6:00	12400
8/2/03	5:00	32200
8/3/03	5:00	60200
8/4/03	5:00	25800
8/24/03	5:00	21900
8/25/03	5:00	20700
8/26/03	5:00	12600
8/27/03	5:00	25600
8/28/03	11:45	31800
8/30/03	13:05	12000
9/19/03	8:55	20300
9/20/03	5:00	31600
9/21/03	5:00	36900
9/22/03	5:00	42600
9/23/03	5:00	22700
9/24/03	7:25	10800
9/27/03	5:00	15800
9/28/03	5:00	19300
9/29/03	5:00	14900
9/30/03	7:40	17900
1/21/05	5:00	33500
1/25/05	5:00	27600
1/26/05	5:00	27500
1/27/05	5:00	19300
1/28/05	13:15	17800
2/10/05	5:20	16100
2/12/05	5:00	19200
2/14/05	5:00	16600
2/15/05	11:30	10800
3/9/05	5:00	14400
3/10/05	5:00	25300
3/11/05	5:00	15100
3/12/05	5:00	12400
3/13/05	5:00	18400
4/7/05	5:00	13400
4/8/05	5:00	18900
4/9/05	5:00	17800
4/10/05	5:00	29500
4/16/05	5:00	18300
4/17/05	5:00	15300
4/18/05	5:00	20200
5/17/05	5:35	13900
5/18/05	5:00	51700
5/19/05	5:00	86300
5/20/05	5:00	74000
6/14/05	5:00	13500
6/15/05	8:30	22600
7/13/05	5:00	11300
8/8/05	5:00	21100
8/9/05	5:00	45100
8/10/05	12:15	49100
8/10/05	14:35	49100
8/26/05	5:00	33600
8/27/05	5:00	15500
8/28/05	5:00	15400
9/4/05	11:15	10200
9/5/05	5:00	15900
12/15/06	12:05	50700
12/16/06	5:00	45700
12/17/06	5:00	43300
12/18/06	5:00	13600
12/19/06	5:15	38300
12/20/06	5:00	11800
12/22/06	5:00	12900
12/23/06	5:00	12400
12/24/06	5:00	13500
12/25/06	5:00	15300
12/26/06	5:00	13300
12/27/06	5:00	14000
12/28/06	5:00	10900
12/29/06	5:00	12800
12/30/06	5:00	11600
1/19/07	5:00	12200
1/20/07	5:00	15600
1/21/07	5:00	13100
1/22/07	5:00	14900
1/23/07	5:00	10500
1/25/07	5:00	11000
1/26/07	5:00	10800
2/1/07	5:15	10400
2/2/07	5:00	13500
2/3/07	5:00	13000
2/4/07	5:00	10900
3/9/07	5:00	21400
3/10/07	7:35	17900
4/5/07	5:00	17100
4/6/07	5:00	20100
4/7/07	5:00	28000
4/8/07	5:00	22000
4/9/07	11:05	24400
4/30/07	5:00	19400
5/26/07	9:35	17600
5/27/07	5:00	24100
5/28/07	5:00	22500

10/17/03	5:00	24800
10/18/03	5:00	15700
10/19/03	2:55	13200
10/20/03	5:20	14900
10/21/03	5:00	13500
10/23/03	10:50	12000
11/3/03	11:10	20100
11/13/03	5:00	26400
11/14/03	8:10	38200
11/17/03	5:00	20700
11/18/03	5:00	29000
11/19/03	5:00	16300
11/20/03	5:00	21800
12/10/03	5:00	13500
12/11/03	5:00	15000
12/12/03	5:00	22700
12/13/03	5:00	25100
12/14/03	5:00	24300
12/15/03	5:00	27100
12/16/03	5:00	25300
12/17/03	5:00	21200
12/18/03	5:00	24900
12/19/03	5:00	25100
12/20/03	5:00	21000
1/7/04	7:35	10100
1/20/04	8:50	13300
2/14/04	5:00	17000
2/15/04	5:00	20900
2/16/04	5:00	19300
2/17/04	5:00	23600
2/18/04	5:00	25200
2/19/04	5:00	48900
2/21/04	10:05	17200
3/12/04	5:00	11000
3/13/04	5:00	17600
3/14/04	5:00	26300
3/15/04	8:35	12500
3/16/04	5:10	11300
3/30/04	6:35	10300
4/8/04	4:00	10000
7/24/04	5:00	32100
9/6/05	5:00	38900
9/7/05	5:00	34200
9/9/05	5:00	15400
9/13/05	5:30	13700
9/14/05	5:00	12700
9/15/05	5:00	29700
9/16/05	5:05	23600
9/17/05	5:00	39000
9/18/05	5:00	59100
9/19/05	5:00	59100
9/20/05	5:00	75100
9/21/05	5:00	38700
9/22/05	5:00	47300
9/23/05	12:50	32000
1/1/06	8:20	13300
1/2/06	14:35	11900
2/23/06	5:00	11400
2/24/06	5:00	10800
3/21/06	5:00	17500
3/22/06	5:00	36300
3/23/06	5:00	13800
3/24/06	5:00	16600
3/25/06	12:05	26100
4/16/06	5:00	22300
4/17/06	5:00	44400
4/18/06	5:00	52300
4/20/06	5:00	22700
4/21/06	8:05	34400
5/13/06	5:00	10400
5/14/06	5:10	16900
5/15/06	5:00	11900
5/16/06	5:00	13000
5/17/06	5:00	14400
6/10/06	5:24	15900
6/12/06	5:00	15000
6/13/06	5:00	13400
6/14/06	5:00	14600
6/15/06	5:45	12800
8/10/06	5:00	10300
8/11/06	5:00	12000
9/8/06	10:25	10300
5/29/07	5:00	18400
5/30/07	5:00	22500
5/31/07	5:00	24500
6/1/07	8:50	22500
9/4/07	5:00	27000
9/5/07	5:00	19100
9/6/07	5:00	14300
10/1/07	5:00	15200
10/2/07	5:00	38400
10/3/07	5:00	33500
10/29/07	5:00	18700
10/30/07	11:40	14900
12/21/07	9:20	22700
1/9/08	5:00	14800
1/10/08	5:00	16200
1/11/08	5:00	16000
1/12/08	5:00	14300
1/18/08	10:10	10800
2/4/08	5:00	11500
2/5/08	5:00	14300
2/6/08	5:00	17200
3/2/08	5:00	19400
3/3/08	5:00	40600
3/4/08	5:00	35200
3/5/08	5:00	34900
3/13/08	5:00	15000
3/14/08	5:00	20600
3/15/08	7:55	21000
3/16/08	5:00	11300
3/17/08	5:00	10050
3/18/08	11:50	10300
3/29/08	5:00	47700
3/30/08	5:00	52300
3/31/08	5:00	34500
4/1/08	5:00	35600
4/2/08	5:00	22900
4/3/08	5:00	29100
4/4/08	5:00	33800
4/5/08	17:00	26000
4/8/08	10:30	10100
4/9/08	5:20	11900

7/25/04	9:00	22100
7/27/04	6:15	11100
7/28/04	5:00	12800
8/1/04	7:05	54600
8/3/04	5:00	23500
8/5/04	5:00	27600
9/17/04	11:00	13000
10/16/04	5:00	11500
10/17/04	5:00	13100
11/11/04	5:00	31900
11/12/04	5:00	47200
11/16/04	5:00	10700
1/5/05	5:00	23300
1/6/05	5:00	25200
1/7/05	5:00	22700
1/20/05	5:00	18500

9/20/06	5:00	20300
9/21/06	5:00	19400
9/22/06	5:00	20300
9/23/06	5:00	15400
10/4/06	5:00	10200
10/5/06	5:00	11200
10/6/06	5:00	10200
10/16/06	5:00	14100
10/17/06	5:00	25700
10/18/06	5:00	15900
10/19/06	5:00	18000
10/20/06	5:00	20700
11/13/06	5:00	14200
11/14/06	5:00	13400
11/15/06	8:50	15600
11/29/06	6:25	11600

4/10/08	5:00	11700
4/11/08	5:00	19000
4/12/08	5:00	14200
4/25/08	5:00	22900
4/26/08	5:00	17800
4/27/08	4:00	35900
4/28/08	5:35	15500
4/29/08	5:05	12700
7/16/08	5:00	10100
7/17/08	5:00	10300
7/25/08	5:00	11100
7/26/08	5:00	12600
8/13/08	5:00	10400
10/14/08	5:00	11000
10/15/08	5:30	15200

Appendix D. Severe Solar Space Weather Event Dates (Solar Flare > X10)

Day	Year	Solar Flare
2-Apr	2001	X14
15-Apr	2001	X17
28-Oct	2003	X17
29-Oct	2003	X10
4-Nov	2003	X18
7-Sep	2005	X17.1

Appendix E: SPEs with 10 MeV Proton Flux > 1,000 pfu

Date	Year	Proton Flux
21-Apr	1998	1700
3-Apr	2001	1110
2-Oct	2001	2360
21-Apr	2002	2520
3-Nov	2003	1570
26-Jul	2004	2086
17-Jan	2005	5040
15-May	2005	3140
11-Sep	2005	1880
7-Dec	2006	1980
24-Jan	2012	6310
8-Mar	2012	6530

Appendix F: SPEs with 10 MeV Proton Flux > 100 pfu

Date	Year	Proton Flux
7-Nov	1997	490
2-May	1998	150
6-May	1998	210
26-Aug	1998	670
14-Nov	1998	310
13-Sep	2000	320
26-Nov	2000	940
11-Apr	2001	355
15-Apr	2001	951
18-Apr	2001	321
16-Aug	2001	493
26-Dec	2001	779
31-Dec	2001	108
23-May	2002	820
17-Jul	2002	234
24-Aug	2002	317
7-Sep	2002	208
10-Nov	2002	404
29-May	2003	121
26-Oct	2003	466
5-Nov	2003	353
14-Sep	2004	273
8-Nov	2004	495
15-Jul	2005	134
23-Aug	2005	330
13-Dec	2006	698
28-Jan	2012	796
17-May	2012	255
18-Jul	2012	136

Appendix G: SPEs with 10 MeV Proton Flux > 10 pfu

Date	Year	Proton Flux
4-Nov	1997	72
25-Sep	1998	44
8-Nov	1998	11
23-Jan	1999	14
25-Apr	1999	32
5-May	1999	14
2-Jun	1999	48
4-Jun	1999	64
18-Feb	2000	13
5-Apr	2000	55
8-Jun	2000	84
10-Jun	2000	46
22-Jul	2000	17
28-Jul	2000	18
11-Aug	2000	17
16-Oct	2000	15
26-Oct	2000	15
29-Jan	2001	49
30-Mar	2001	35
28-Apr	2001	57
8-May	2001	30
16-Jun	2001	26
10-Aug	2001	17
15-Sep	2001	11
19-Oct	2001	11
22-Oct	2001	24
20-Nov	2001	34
29-Dec	2001	76
11-Jan	2002	91
15-Jan	2002	15
20-Feb	2002	13
17-Mar	2002	13
19-Mar	2002	53
20-Mar	2002	19
23-Mar	2002	16
17-Apr	2002	24
7-Jul	2002	22
19-Jul	2002	13

23-Jul	2002	28
14-Aug	2002	26
22-Aug	2002	36
31-May	2003	27
19-Jun	2003	24
22-Nov	2003	13
2-Dec	2003	86
11-Apr	2004	35
20-Sep	2004	57
1-Nov	2004	63
14-Aug	2010	14
8-Mar	2011	50
22-Mar	2011	14
7-Jun	2011	72
5-Aug	2011	96
9-Aug	2011	26
26-Sep	2011	35
27-Nov	2011	80
27-May	2012	14
16-Jun	2012	14
7-Jul	2012	25
12-Jul	2012	96

Appendix H: GOES 2 MeV Electron Flux and SSPA Current

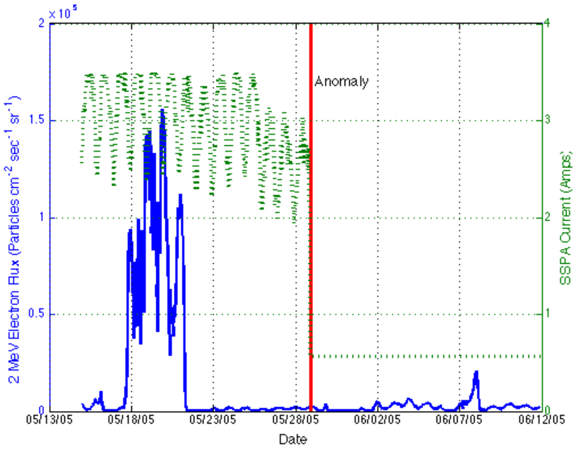

(a)

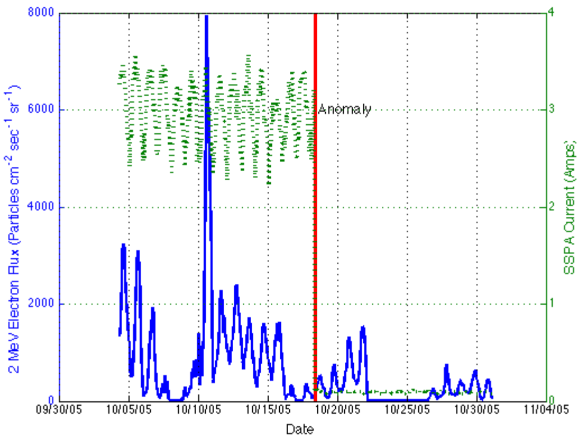

(b)

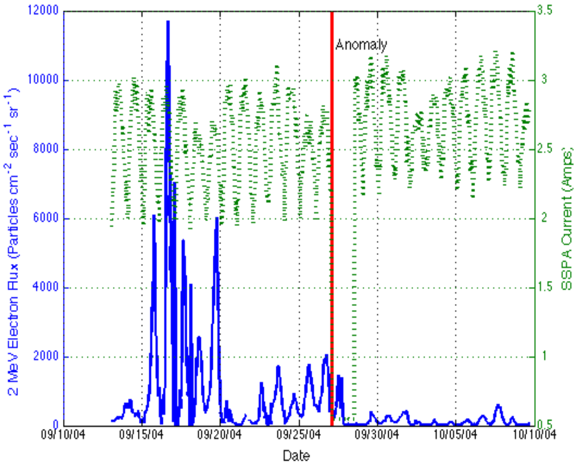

(c)

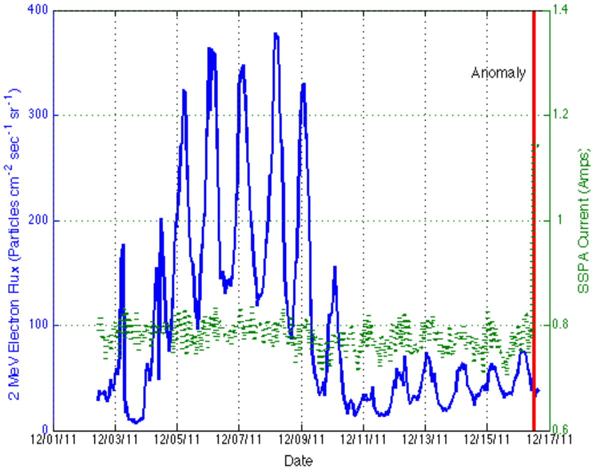

(d)

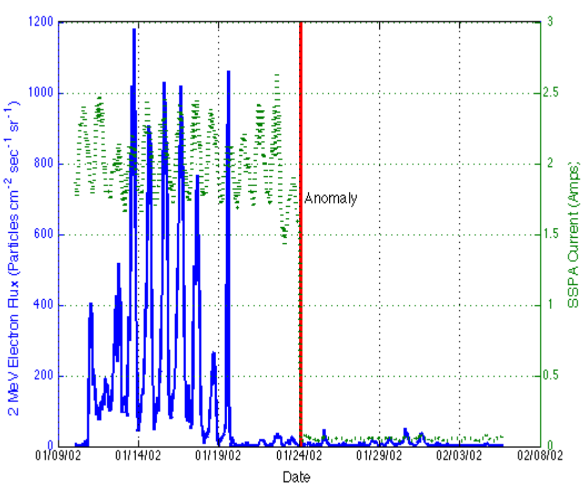

(e)

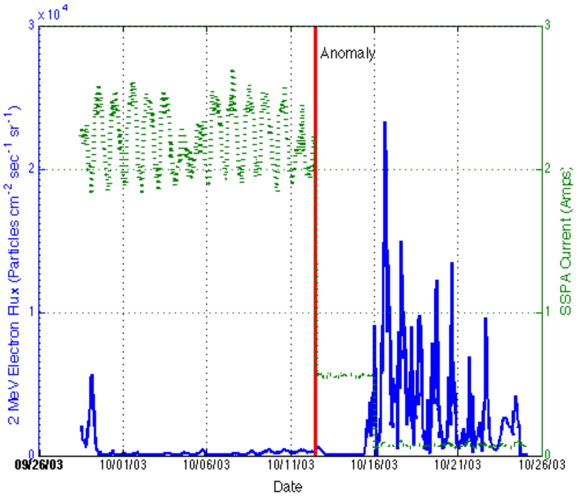

(f)

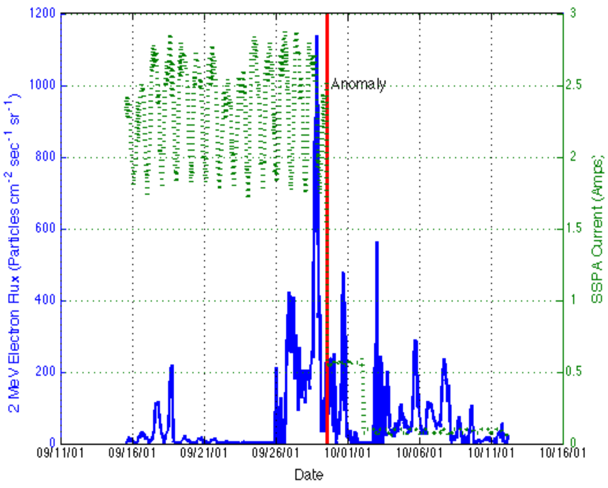
1200
1000
800
600
400
200
0
3
2.5
2
1.5
1
0.5
0
Anomaly
2 MeV Electron Flux (Particles cm^{-2} sec^{-1} sr^{-1})
SSPA Current (Amps)
09/11/01
09/16/01
09/21/01
09/26/01
10/01/01
10/06/01
10/11/01
10/16/01
Date

(g)

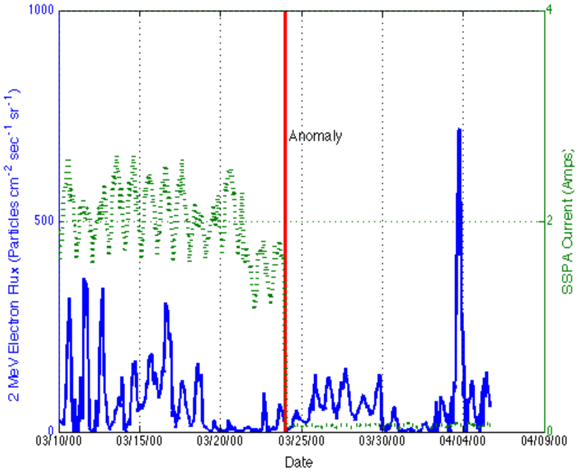
1000
500
0
4
2
0
Anomaly
2 MeV Electron Flux (Particles cm^{-2} sec^{-1} sr^{-1})
SSPA Current (Amps)
03/10/00
03/15/00
03/20/00
03/25/00
03/30/00
04/04/00
04/09/00
Date

(h)

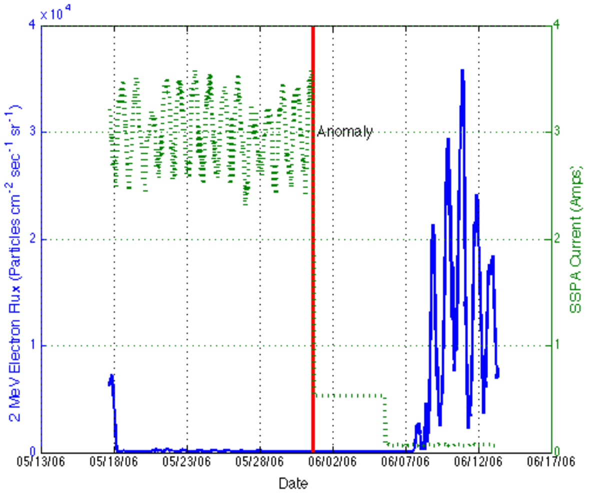
x 10^4
4
3
2
1
0
4
3
2
1
0
Anomaly
2 MeV Electron Flux (Particles cm^{-2} sec^{-1} sr^{-1})
SSPA Current (Amps)
05/13/06
05/18/06
05/23/06
05/28/06
06/02/06
06/07/06
06/12/06
06/17/06
Date

(i)

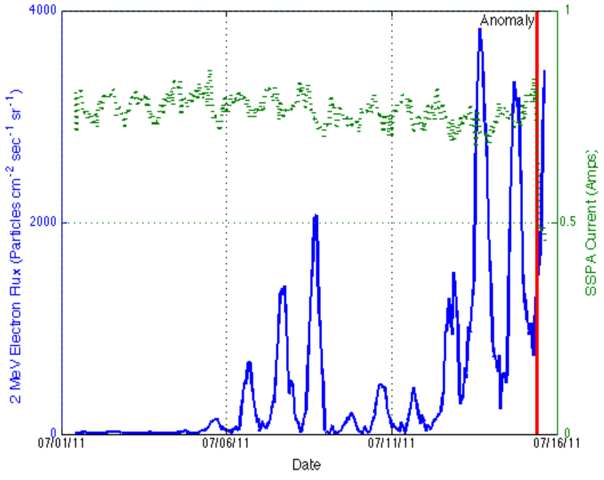
4000
2000
0
1
0.5
0
Anomaly
2 MeV Electron Flux (Particles cm^{-2} sec^{-1} sr^{-1})
SSPA Current (Amps)
07/01/11
07/06/11
07/11/11
07/16/11
Date

(j)

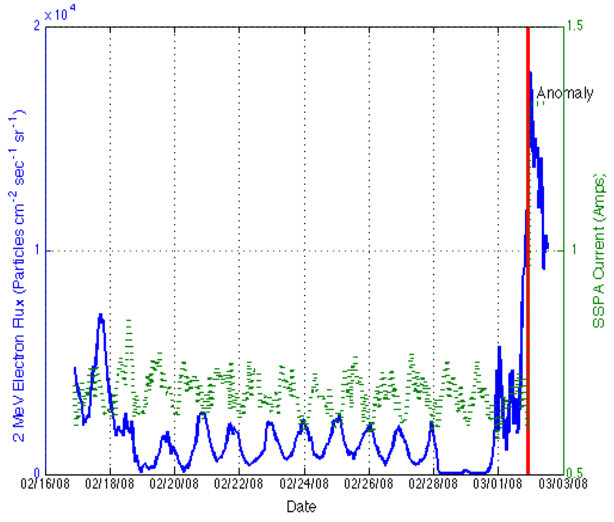
x 10^4
2
1
0
1.5
1
0.5
Anomaly
2 MeV Electron Flux (Particles cm^{-2} sec^{-1} sr^{-1})
SSPA Current (Amps)
02/16/08
02/18/08
02/20/08
02/22/08
02/24/08
02/26/08
02/28/08
03/01/08
03/03/08
Date

(k)

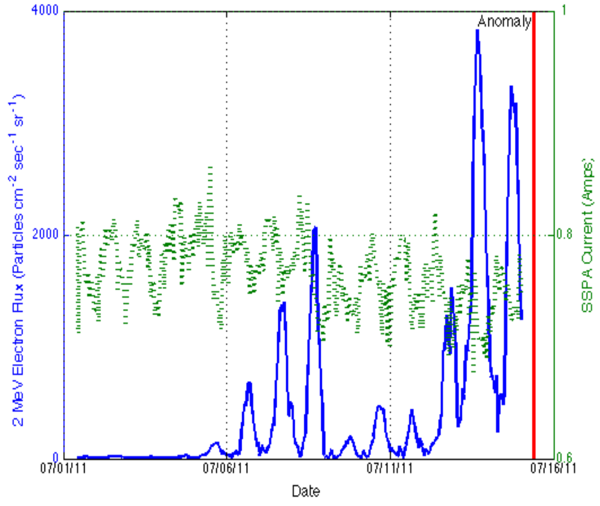
4000
2000
0
1
0.8
0.6
Anomaly
2 MeV Electron Flux (Particles cm^{-2} sec^{-1} sr^{-1})
SSPA Current (Amps)
07/01/11
07/06/11
07/11/11
07/16/11
Date

(l)

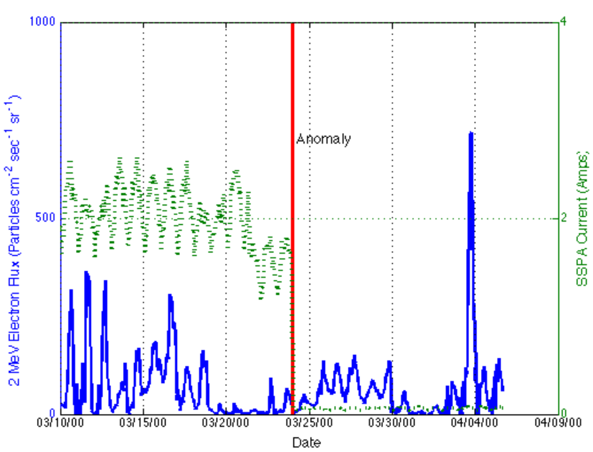
1000
500
0
4
2
0
Anomaly
2 MeV Electron Flux (Particles cm-2 sec-1 sr-1)
SSPA Current (Amps)
03/10/00
03/15/00
03/20/00
03/25/00
03/30/00
04/04/00
04/09/00
Date

(m)

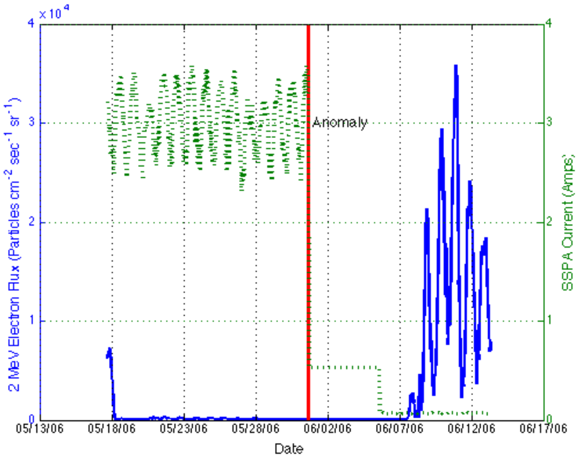
x 10^4
4
3
2
1
0
Anomaly
2 MeV Electron Flux (Particles cm-2 sec-1 sr-1)
SSPA Current (Amps)
05/13/06
05/18/06
05/23/06
05/28/06
06/02/06
06/07/06
06/12/06
06/17/06
Date

(n)

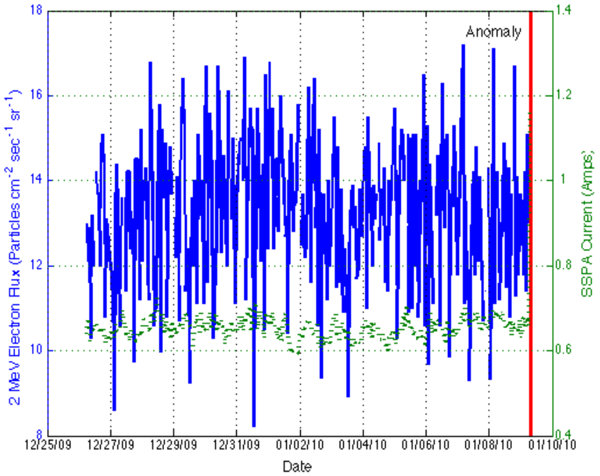
18
16
14
12
10
8
1.4
1.2
1
0.8
0.6
0.4
Anomaly
2 MeV Electron Flux (Particles cm-2 sec-1 sr-1)
SSPA Current (Amps)
12/25/09
12/27/09
12/29/09
12/31/09
01/02/10
01/04/10
01/06/10
01/08/10
01/10/10
Date

(o)

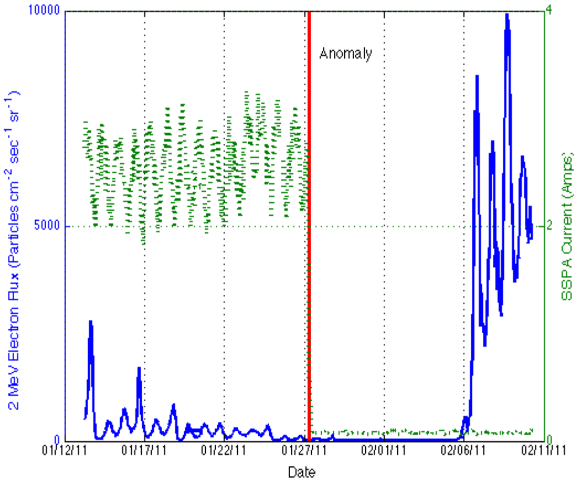
10000
5000
0
4
2
0
Anomaly
2 MeV Electron Flux (Particles cm-2 sec-1 sr-1)
SSPA Current (Amps)
01/12/11
01/17/11
01/22/11
01/27/11
02/01/11
02/06/11
02/11/11
Date

(p)

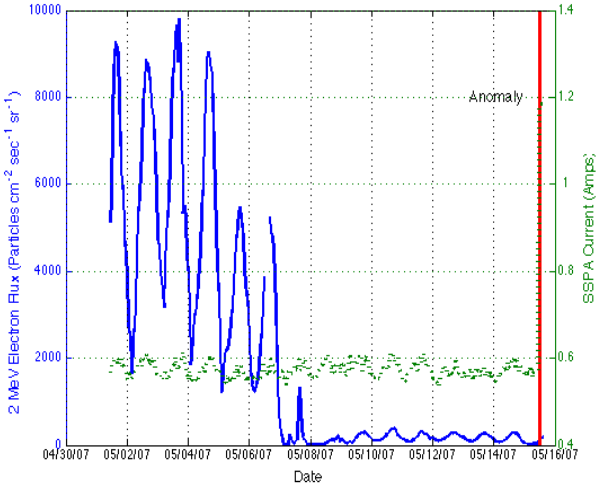
10000
8000
6000
4000
2000
0
1.4
1.2
1
0.8
0.6
0.4
Anomaly
2 MeV Electron Flux (Particles cm-2 sec-1 sr-1)
SSPA Current (Amps)
04/30/07
05/02/07
05/04/07
05/06/07
05/08/07
05/10/07
05/12/07
05/14/07
05/16/07
Date

(q)

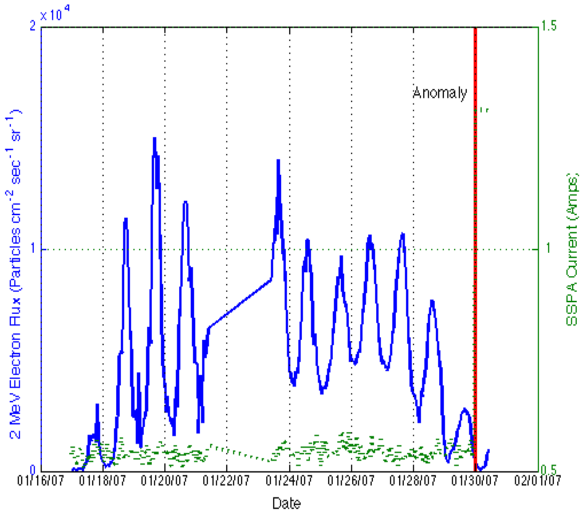
x 10^4
2
1
0
1.5
1
0.5
Anomaly
2 MeV Electron Flux (Particles cm-2 sec-1 sr-1)
SSPA Current (Amps)
01/16/07
01/18/07
01/20/07
01/22/07
01/24/07
01/26/07
01/28/07
01/30/07
02/01/07
Date

(r)

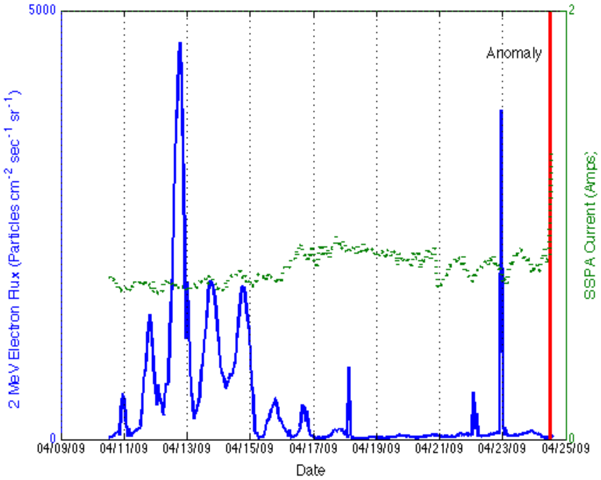
5000
0
2
0
Anomaly
2 MeV Electron Flux (Particles cm^{-2} sec^{-1} sr^{-1})
SSPA Current (Amps)
04/09/09
04/11/09
04/13/09
04/15/09
04/17/09
04/19/09
04/21/09
04/23/09
04/25/09
Date

(s)

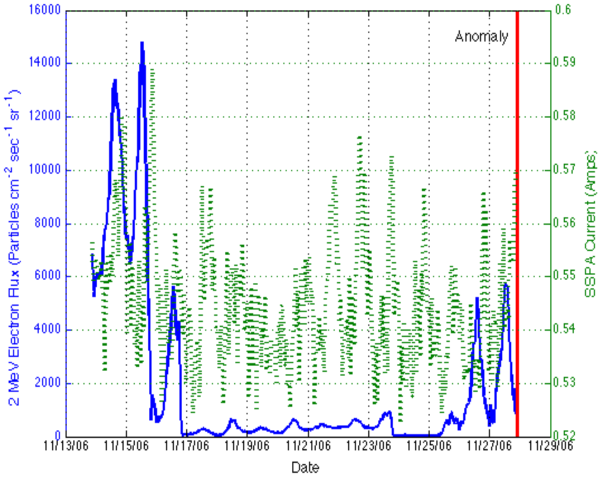
16000
14000
12000
10000
8000
6000
4000
2000
0
0.6
0.59
0.58
0.57
0.56
0.55
0.54
0.53
0.52
Anomaly
2 MeV Electron Flux (Particles cm^{-2} sec^{-1} sr^{-1})
SSPA Current (Amps)
11/13/06
11/15/06
11/17/06
11/19/06
11/21/06
11/23/06
11/25/06
11/27/06
11/29/06
Date

(t)

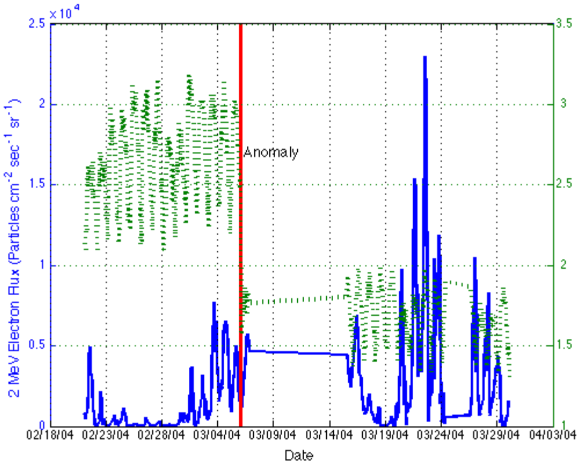
x 10^4
2.5
2
1.5
1
0.5
0
3.5
3
2.5
2
1.5
1
Anomaly
2 MeV Electron Flux (Particles cm^{-2} sec^{-1} sr^{-1})
SSPA Current (Amps)
02/18/04
02/23/04
02/28/04
03/04/04
03/09/04
03/14/04
03/19/04
03/24/04
03/29/04
04/03/04
Date

(u)

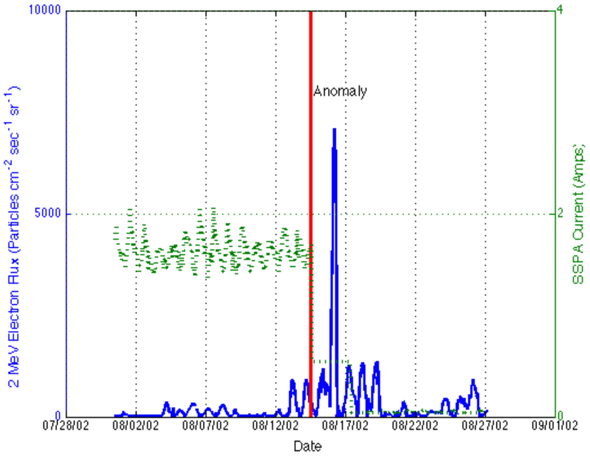
10000
5000
0
4
2
0
Anomaly
2 MeV Electron Flux (Particles cm^{-2} sec^{-1} sr^{-1})
SSPA Current (Amps)
07/28/02
08/02/02
08/07/02
08/12/02
08/17/02
08/22/02
08/27/02
09/01/02
Date

(v)

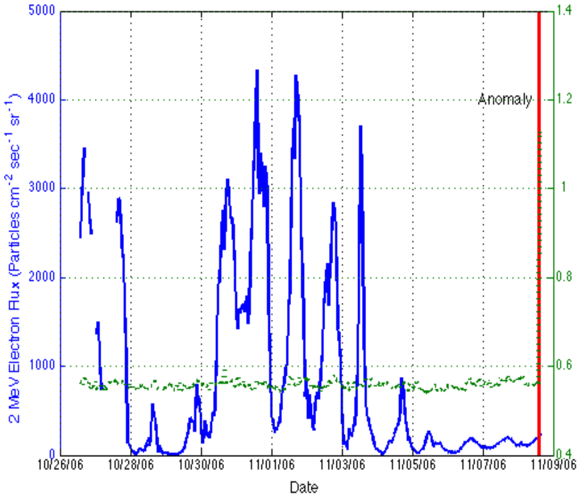
5000
4000
3000
2000
1000
0
1.4
1.2
1
0.8
0.6
0.4
Anomaly
2 MeV Electron Flux (Particles cm^{-2} sec^{-1} sr^{-1})
SSPA Current (Amps)
10/26/06
10/28/06
10/30/06
11/01/06
11/03/06
11/05/06
11/07/06
11/09/06
Date

(w)

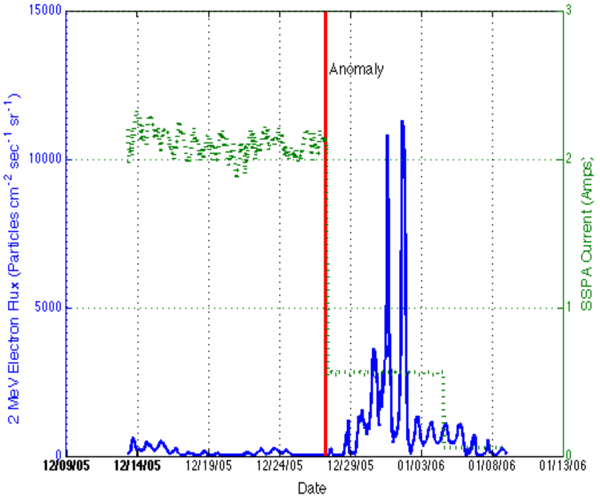
15000
10000
5000
0
3
2
1
0
Anomaly
2 MeV Electron Flux (Particles cm^{-2} sec^{-1} sr^{-1})
SSPA Current (Amps)
12/09/05
12/14/05
12/19/05
12/24/05
12/29/05
01/03/06
01/08/06
01/13/06
Date

(x)

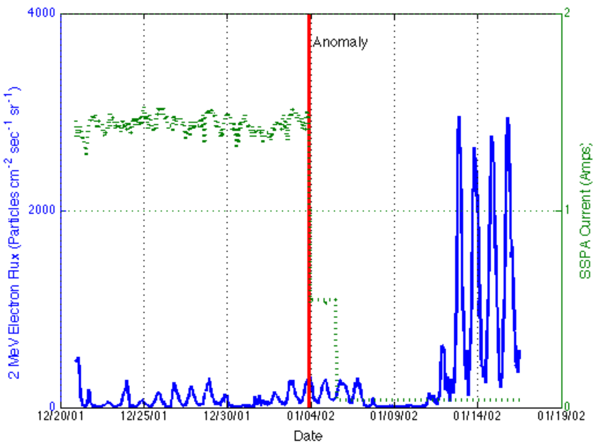
4000
2000
0
2
1
0
2 MeV Electron Flux (Particles cm^{-2} sec^{-1} sr^{-1})
SSPA Current (Amps)
Anomaly
12/20/01
12/25/01
12/30/01
01/04/02
01/09/02
01/14/02
01/19/02
Date

(y)

References

ACE Science Center. "New ACE Level 2 Data Server." *ACE Level 2 Data Server*. NASA, 21 Apr. 2008. 1 May 2012. http://www.srl.caltech.edu/ACE/ASC/level2/new/intro.html.

Allen, J.H. (2004), "The Ap* Index of Maximum 24-Hour Disturbance for Storm Events: An index description and personal reminiscence by its author, J.H. Allen". *NOAA National Geophysical Data Center.* 18 January 2004. Web. 10 September 2012. http://www.ngdc.noaa.gov/stp/geomag/apstar.html.

Astrium, "SSPA – L Band". EADS. http://www.astrium.eads.net/en/equipment/l-band-sspa.html.

Baker, D. "What Is Space Weather?" *Advances in Space Research* 22.1 (1998): 7-16.

Baker, D.N. "The Occurrence of Operational Anomalies in Spacecraft and Their Relationship to Space Weather" *IEEE Transactions on Plasma Science* 28.6 (2000): 2007-2016.

Baker, D. N. "How to Cope with Space Weather." *Science* 297 (2002): 1486-487.

Baker, D.N. "Effects of Hostile Space Weather on Satellite Operations," *IEEE International Symposium on Electromagnetic Compatibility (EMC)*. 14-19 Aug. 2011. 306-311.

Balch, Christopher. "The K-Index." *Space Weather Prediction Center*. NOAA National Geophysical Data Center, 12 Dec. 2011. Web. 20 Feb. 2012. <http://www.swpc.noaa.gov/info /Kindex.html>.

Bartel, J. "Twenty-seven day recurrences in terrestrial-magnetic and solar activity, 1923-1933", *Terrestrial Magnetism and Atmospheric Electricity*, 33(3): 201-201a, 1934.

Bono, J., (2005), "Development of A Defense Meteorological Satellite Program (DMSP) F-15 Disturbance Storm-Time (Dst) Index", *Air Force Institute of Technology*, AFIT/GAP/ENP/05-02.

Choi, H.S., et al., "Analysis of GEO spacecraft anomalies: Space weather relationships", *Space Weather,* 9, pp.1-12, 2012.

CNES, "The Eclipse Phenomenon", Euromet Meteo France, http://euromet.meteo.fr/euromet/english/satmet/s3220/s3220501.htm.

Colantonio, P., and Giannini, F., "High Efficiency RF and Microwave Solid State Power Amplifiers", Wiley, 2009.

Cole, David G., "Space Weather: Its effects and predictability" *Space Science Reviews* 107 (2003): 295-302.

Elbert, B., and Schiff, M., "Simulating the Performance of Communications Links with Satellite Transponders", Application Technology Strategy, Inc., 2002. http://www.applicationstrategy.com/Communications_simulation.htm

European Space Agency. "SPENVIS - Space Environment, Effects, and Education System." *SPENVIS - Space Environment, Effects, and Education System*. ESA, 1997. Web. 1 March 2012. <http://www.spenvis.oma.be/intro.php>.

Fennel, J.F., H.C. Koons, J.L. Roeder, and J.B. Blake (2001), Spacecraft charging: Observations and relationships to satellite anomalies, *Aerosp. Rep. TR-2001(8570)-5,* Aerosp. Corp., Los Angeles, Calif.

Feldman, U., Schühle, U., Widing, K. G., & Laming, J. M. "Coronal composition above the solar equator and the North Pole as determined from spectra acquired by the SUMER Instrument on SOHO, *The Astrophysical Journal*, 505, pp. 999-1006, 1998.

GOES I-M Databook. Palo Alto, CA: Space Systems/Loral, 1996.

Gopalswamy, N., Yashiro, S., and Akiyama, S., (2006), Coronal mass ejections and space weather due to extreme events, paper presented at International Living With A Star (ILWS) Workshop, Goa, India.

Gubby, Robin, and John Evans. "Space Environment Effects and Satellite Design." *Journal of Atmospheric and Solar-Terrestrial Physics* 64.16 (2002): 1723-733.

Intelsat, "Eclipse Seasons", Tech-Talk, 2012, http://www.intelsat.com/resources/tech-talk/eclipse-seasons.asp

Lanzerotti, "Space Weather Effects on Communications" *NATO Science Series: Space Storms and Space Weather Hazards* 38 (2001): 313-334.

Lohmeyer, W., Cahoy, K., and Baker, D.N., (2012), Correlation of GEO Communication Satellite Anomalies and Space Weather Phenomena: Improved Satellite Performance and Risk Mitigation, paper presented at 30th AIAA International Communications Satellite Systems Conference (ICSSC), Ottawa, Canada.

Mazur, J.E., and O'Brien, T.P., "Comment on "Analysis of GEO spacecraft anomalies: Space weather relationships" by Ho-Sung Choi et al.", *Space Weather*, Vol. 10, (2012): pp. 1-2.

Miyoshi, Y. and R. Katoaka (2008), Flux enhancement of the outer radiation belt electrons after the arrival of stream interaction regions" *Journal of Geophysical Research*, Vol. 113. Doi: 10.1029/2007JA012506

Mursula, "A New reconstruction of the Dst index for 1932 – 2002" *Annales Geophysicae* 23:2 (2005): 475-485.

NASA SPOF, "*Magnetic Storms"*. NASA Space Physics Data Facility (SPOF), 13 March 2006. Web. 14 Dec. 2011. http://www-spof.gsfc.nasa.gov/Education/wmagstrm.html.

National Weather Service. "NOAA / NWS Space Weather Prediction Center." *NOAA / NWS Space Weather Prediction Center*. National Oceanic and Atmospheric Administration, 5 Nov. 2007. Web. 23 Mar. 2012. http://www.swpc.noaa.gov/.

NRC "Severe Space Weather Events – Understanding Societal and Economic Impacts Workshop" *National Research Council*. National Academy of Sciences. http://www.nap.edu/catalog/12507.html.

O'Brien, P.T. and R.L. McPherron (2000), Forecasting the ring current index Dst in real time", *Journal of Atmospheric and Solar-Terrestrial Physics*, 62, 1295-1299. doi: 10.1016/S1364-6826(00)00072-9

Peterson, E., Approaches to proton single-event rate calculations, *IEEE Transactions on Nuclear Science*, *43*(2), pp. 496-504, 1996.

Rangarajan and Lyemori, “Time variations of geomagnetic activity indices Kp and Ap: an update”, *Annales Geophysicae*, 15(10), pp. 1271-1290, 1997.

Reeves, G. D., S. K. Morley, R. H. W. Friedel, M. G. Henderson, T. E. Cayton, G. Cunningham, J. B. Blake, R. A. Christensen, and D. Thomsen (2011), On the relationship between relativistic electron flux and solar wind velocity: Paulikas and Blake revisited, J. Geophys. Res., 116, A02213, doi:10.1029/2010JA015735.

Riley, Pete. “On the probability of occurrence of extreme space weather events” AGU Space Weather, Vol. 10, SO2012, doi: 10.1029/2011SW000734, 2012.

Robinson, P. A. Jr. (1989). “Spacecraft Environmental Anomalies Handbook,” JPL Report GL-TR 89 0222, Pasadena, CA.

Royal Observatory of Belgium. "SIDC - Solar Influences Data Analysis Center." *SIDC - Solar Influences Data Analysis Center*. 28 Aug. 2003. Web. 25 June 2012. <http://sidc.oma.be/ sunspot-data/>.

Sechi, Franco, and M. Bujatti (2009). *Solid-state Microwave High-power Amplifiers*. Boston: Artech House.

Shea, M.A. and D.F. Smart (1998), “Space Weather: The Effects on Operations in Space” *Adv. Space Res.* Vol. 22, 29-38, doi: 10.1016/S0273-1177(97)01097-1.

The National Space Weather Program Council. "National Space Weather Implementation Plan, 2nd Edition." *The National Space Weather Program*. Office of the Federal Coordinator for Meteorology, July 2000. Web. 17 July 2012. <http://www.ofcm.gov/nswpip/tableofcon tents.htm>.

Thomsen, M. F., M. H. Denton, B. Lavraud, and M. Bodeau. "Statistics of Plasma Fluxes at Geosynchronous Orbit over More than a Full Solar Cycle." *Space Weather* 5.3 (2007): 1-9.

Tylka, Allan J., William F. Dietrich, Paul R. Boberg, Edward C. Smith, and James H. Adams. "Single event upsets caused by solar energetic heavy ions." *IEEE Transactions on Nuclear Science*, 43.6, pp. 2758-766, 1996.

Vampola, A. L, et al.. *The Aerospace Spacecraft Charging Document*. [S.l.]: Space Division, Air Force Systems Command, 1985.

Wilkinson, D. (1991), TDRS-1 Single Event Upsets and the Effect of the Space Environment, *IEEE Transactions on Nuclear Science*, *38*(6), 1708-1712.

Wilkinson, D.C. (1994), National Oceanic and Atmospheric Administration’s spacecraft anomaly data base and examples of solar activity affecting spacecraft, *J. Spacecr. Rockets, 31,* 160-165, doi:10.2514/3.26417.

Wilkinson, D.C., Shea, M.A., Smart, D.F. “A Case History of Solar and Galactic Space Weather Effects on the GEO COMSAT TDRS-1”, *Adv. Space Research, 26*(1), pp. 27-30, 2000.

World Data Center for Geomagnetism, Kyoto. "Geomagnetic Equatorial Dst Index Home Page." *Geomagnetic Equatorial Dst Index Home Page*. Data Analysis Center for Geomagnetism and Space Magnetism, n.d. Web. January 2012. <http://wdc.kugi.kyotou.ac.jp/dstdir/index.html>.